

THESIS

ACOUSTIC TOMOGRAPHY OF THE ATMOSPHERE USING ITERATED  
UNSCENTED KALMAN FILTER

Submitted by

Soheil Kolouri

Department of Electrical and Computer Engineering

In partial fulfillment of the requirements

For the Degree of Master of Science

Colorado State University

Fort Collins, Colorado

Fall 2012

Master's Committee:

Advisor: Mahmood R. Azimi-Sadjadi

Edwin K. P. Chong

Daniel S. Cooley

## ABSTRACT

### ACOUSTIC TOMOGRAPHY OF THE ATMOSPHERE USING ITERATED UNSCENTED KALMAN FILTER

Tomography approaches are of great interests because of their non-intrusive nature and their ability to generate a significantly larger amount of data in comparison to the in-situ measurement method. Acoustic tomography is an approach which reconstructs the unknown parameters that affect the propagation of acoustic rays in a field of interest by studying the temporal characteristics of the propagation. Acoustic tomography has been used in several different disciplines such as biomedical imaging, oceanographic studies and atmospheric studies.

The focus of this thesis is to study acoustic tomography of the atmosphere in order to reconstruct the temperature and wind velocity fields in the atmospheric surface layer using the travel-times collected from several pairs of transmitter and receiver sensors distributed in the field. Our work consists of three main parts.

The first part of this thesis is dedicated to reviewing the existing methods for acoustic tomography of the atmosphere, namely statistical inversion (SI), time dependent statistical inversion (TDSI), simultaneous iterative reconstruction technique (SIRT), and sparse recovery framework. The properties of these methods are then explained extensively and their shortcomings are also mentioned.

In the second part of this thesis, a new acoustic tomography method based on Unscented Kalman Filter (UKF) is introduced in order to address some of the shortcomings of the existing methods. Using the UKF, the problem is cast as a state estimation problem in which the temperature and wind velocity fields are the desired states to be reconstructed. The field is discretized into several grids in which the

temperature and wind velocity fields are assumed to be constant. Different models, namely random walk, first order 3-D autoregressive (AR) model, and 1-D temporal AR model are used to capture the state evolution in time-space . Given the time of arrival (TOA) equation for acoustic propagation as the observation equation, the temperature and wind velocity fields are then reconstructed using a fixed point iterative UKF.

The focus in the third part of this thesis is on generating a meaningful synthetic data for the temperature and wind velocity fields to test the proposed algorithms. A 2-D Fractal Brownian motion (fBm)-based method is used in order to generate realizations of the temperature and wind velocity fields. The synthetic data is generated for 500 subsequent snapshots of wind velocity and temperature field realizations with spatial resolution of one meter and temporal resolution of 12 seconds. Given the location of acoustic sensors the TOA's are calculated for all the acoustic paths. In addition, white Gaussian noise is added to the calculated TOAs in order to simulate the measurement error. The synthetic data is then used to test the proposed method and the results are compared to those of the TDSI method. This comparison attests to the superiority of the proposed method in terms of accuracy of reconstruction, real-time processing and the ability to track the temporal changes in the data.

## ACKNOWLEDGEMENTS

I would first like to thank my adviser, Dr. Mahmood R. Azimi-Sadjadi, for his invaluable support and considerate guidance throughout the course of this research. He has taught me the value of developing the intellectual reasoning needed to conduct thorough and well-developed research. His guidance and time is greatly appreciated throughout the course of my graduate education.

I would like to thank my committee members, Dr. Edwin K. P. Chong and Dr. Daniel S. Cooley, for their time and assistance and also like to thank Dr. Thomas H. Vonder Haar and Dr. Andrew S. Jones for their useful suggestions throughout the course of this research.

I would like to thank the Cooperative Institute for Research in the Atmosphere, Colorado State University, Fort Collins, for providing the funding for my project. This research was supported by the DoD Center for Geosciences/Atmospheric Research at Colorado State University under Cooperative Agreement W911NF-06-2-0015 with the Army Research Laboratory.

I would like to thank my colleagues in the Signal and Image Processing Lab. They have provided a great environment for discussing work and providing help when most needed. Thanks to Nick, Neil, Gergely, Katalin, Amanda, Adam, and Jared. Special thanks to Nick Klausner for his much needed help and advice.

Finally, I would like to thank my family and my beloved fiancée, Jessi Day, for their support and guidance throughout my education.

## TABLE OF CONTENTS

<b>ABSTRACT</b> . . . . .	<b>ii</b>
<b>ACKNOWLEDGEMENTS</b> . . . . .	<b>iv</b>
<b>1 INTRODUCTION</b> . . . . .	<b>1</b>
1.1 Background and Problem Statement . . . . .	1
1.2 Survey of Previous Work . . . . .	2
1.2.1 Proposed Method . . . . .	5
1.3 Organization of the Thesis . . . . .	6
<b>2 REVIEW OF DIFFERENT TOMOGRAPHY METHODS</b> . . . . .	<b>8</b>
2.1 Introduction . . . . .	8
2.2 Acoustic Propagation Formulation . . . . .	10
2.3 Stochastic Inversion (SI) Method . . . . .	13
2.3.1 Linearization Process . . . . .	14
2.3.2 Spatial Mean Field Estimation . . . . .	15
2.3.3 Observation Equation . . . . .	15
2.3.4 Wiener Filtering . . . . .	16
2.4 Time Dependent Stochastic Inversion (TDSI) Method . . . . .	18
2.4.1 Frozen Turbulence Assumption . . . . .	20

2.5	SIMULTANEOUSLY ITERATIVE RECONSTRUCTION TECHNIQUE (SIRT) . . . . .	21
2.5.1	SIRT Formulation . . . . .	22
2.5.2	Acoustic Tomography Based on SIRT . . . . .	23
2.5.3	Temperature Reconstruction . . . . .	26
2.5.4	Wind Velocity Reconstruction . . . . .	28
2.6	ACOUSTIC TOMOGRAPHY USING SPARSE RECONSTRUCTION FRAMEWORK . . . . .	30
2.6.1	Sparsity in Signal Domain . . . . .	31
2.7	Conclusion . . . . .	34
<b>3</b>	<b>UNSCENTED KALMAN FILTER (UKF) . . . . .</b>	<b>36</b>
3.1	Introduction . . . . .	36
3.2	Probabilistic Inference . . . . .	37
3.3	Unscented Transform . . . . .	40
3.4	State Estimation Using UKF . . . . .	42
3.5	Dual Estimation Problem . . . . .	45
3.6	Fixed-Point Iterative UKF . . . . .	46
3.7	Conclusion . . . . .	49
<b>4</b>	<b>UKF-BASED ACOUSTIC TOMOGRAPHY . . . . .</b>	<b>51</b>
4.1	Introduction . . . . .	51

4.2	Formulation . . . . .	52
4.2.1	State Evolution Process . . . . .	52
4.2.2	Observation Process . . . . .	58
4.3	Conclusion . . . . .	59
<b>5</b>	<b>DATA GENERATION USING FRACTAL BROWNIAN MOTION</b>	<b>60</b>
5.1	Introduction . . . . .	60
5.2	Fractal Brownian Motion . . . . .	61
5.2.1	Fourier-Based Filtering Method . . . . .	63
5.3	Synthetic Data Generation . . . . .	66
5.4	Conclusion . . . . .	68
<b>6</b>	<b>RESULTS ON SYNTHESIZED AND REAL DATA SETS . . . . .</b>	<b>70</b>
6.1	Introduction . . . . .	70
6.2	Results on Synthesized Data Set . . . . .	71
6.2.1	TDSI-Based Acoustic Tomography . . . . .	72
6.2.2	UKF-Based Acoustic Tomography . . . . .	73
6.3	Results on Real Data Sets . . . . .	82
6.4	Conclusion . . . . .	87
<b>7</b>	<b>CONCLUSIONS AND SUGGESTIONS FOR FUTURE WORK</b>	<b>89</b>
7.1	Conclusions and Discussions . . . . .	89

7.2 Future Work . . . . .	93
<b>APPENDIX A — SIRT FORMULATION . . . . .</b>	<b>103</b>

## LIST OF FIGURES

2.1	Parameter demonstration . . . . .	12
2.2	Simple linear system . . . . .	23
2.3	SIRT's framework . . . . .	24
2.4	A reciprocal sensor setup . . . . .	25
2.5	Sparse distribution of the temperature field . . . . .	32
3.1	Probabilistic dynamic state-space model . . . . .	37
3.2	Demonstration of the UT process. . . . .	41
3.3	Schematic of the dual UKF method. . . . .	46
3.4	Fixed point iterative UKF. . . . .	50
4.1	AR support region . . . . .	54
5.1	Schematic diagram of the Fourier-based filtering method. . . . .	64
5.2	STINHO out layer . . . . .	67
5.3	The Oversized fields . . . . .	68
5.4	First Synthetic data . . . . .	69
6.1	Mean fields estimations . . . . .	72
6.2	Boxplot of reconstruction errors . . . . .	76
6.3	Boxplot of reconstruction errors . . . . .	77
6.4	Boxplot of the reconstruction errors . . . . .	78

6.5	Boxplot of the reconstruction errors . . . . .	79
6.6	Comparison of field reconstruction . . . . .	80
6.7	Comparison of field reconstruction . . . . .	81
6.8	Comparison of field reconstruction . . . . .	81
6.9	Comparison of field reconstruction . . . . .	82
6.10	Missing data points . . . . .	83
6.11	In-situ sensors . . . . .	84
6.12	Actual and reconstructed temperature T1 . . . . .	85
6.13	Actual and reconstructed temperature T2 . . . . .	85
6.14	Reconstructed temperature and wind velocity t=50 . . . . .	86
6.15	Reconstructed temperature and wind velocity t=54 . . . . .	86
6.16	Reconstructed temperature and wind velocity t=58 . . . . .	86
6.17	Reconstructed temperature and wind velocity t=62 . . . . .	87
6.18	Reconstructed temperature and wind velocity t=66 . . . . .	87
6.19	Reconstructed temperature and wind velocity t=70 . . . . .	87
A.1	A tomographic setup with reciprocal sensors . . . . .	105
A.2	Layout of the STINHO-2 experiment with reciprocal sensors . . . . .	109
A.3	Actual and estimated temperature-based TOA for the path number 4 . . . . .	111
A.4	Actual and estimated wind velocity-based TOA for the 4'th path . . . . .	112

A.5 Actual and estimated wind velocity-based TOA for the 12'th path . . . 112

# CHAPTER 1

## INTRODUCTION

### 1.1 Background and Problem Statement

Tomography is a method of reconstructing the internal structure of an object by radiating signals through the object and studying its interactions with the signals. A wide variety of signal types with different energy levels can be used to study different mediums, resulting in a vast number of tomography applications. Owing to their non-intrusive nature, tomography methods have been used excessively in medical, non-destructive testing and measurement, oceanographic, and atmospheric arenas.

X-ray tomography, positron emission tomography(PET), magnetic resonance imaging(MRI), ultrasound tomography, etc. are just a few examples of different tomography disciplines [1–3]. In this thesis we are focusing on the acoustic tomography of the atmosphere which aims at reconstructing the temperature and wind velocity fields in the atmospheric surface layer, using the travel-times collected from several pairs of transmitter and receiver sensors distributed in the field. The idea of acoustic travel-time tomography of the atmosphere has emerged from the oceanic acoustic tomography [3], which is a method to measure temperature and current over large regions of the ocean.

Monitoring temperature and wind velocity fields in the atmospheric surface layer has always been of great importance in different disciplines, such as boundary layer meteorology [4, 5], and studies of wave propagation through a turbulent atmosphere [6]. The conventional approach to measure these fields is to use in-situ thermoanemometers. However, employing these sensors within the investigation area has two major drawbacks. First, this is not an economically viable solution as a large number

of such rather expensive sensors is needed to achieve an acceptable spatial resolution. Moreover, deploying these sensors in an investigation area may distort the measured fields and hence leading to inaccurate measurements. Acoustic tomography technique is a popular method [7–12] that has been used in order to measure temperature and wind velocity fields with minimal interference in the investigation area as well as lesser cost.

The speed of a sound ray propagating in the atmosphere is influenced by several parameters like temperature, wind velocity (air flow) and humidity along the propagation path [7–12]. This implies that the measured TOA is directly related to the temperature, wind velocity, and humidity. To be more precise, the TOA for a sound ray is the line integral of the slowness ( $\frac{1}{speed}$ ) of the sound ray over its propagation path. Acoustic tomography methods use this dependency to reconstruct the temperature and wind velocity in an investigation area based on several acoustic travel time measurements between different sources and receivers deployed in an investigation area. Wilson and Thomson [7] showed that for a source and receiver with 100m separation, a path-averaged fluctuation as small as  $1\frac{m}{sec}$  in the wind velocity causes approximately a 0.9msec fluctuation in the TOA, a path-averaged fluctuation as small as 1K in the temperature causes approximately a 0.6msec fluctuation in the time of arrival and a humidity change of  $1gkg^{-1}$  (which is an extremely large change in outdoor conditions) would change the sound velocity by only  $0.2\frac{m}{sec}$ . Thus, the effect of humidity on the travel time is somehow negligible and hence can be ignored [13].

## 1.2 Survey of Previous Work

Acoustic tomography problems are divided into forward and inverse problems [14]. Forward or direct acoustic tomography [15, 16] aims to estimate a detailed structure of the signal at the receivers including the time of arrival and the transmission loss, given the temperature field, wind velocity field, ground condition, and the characteristics

of the sound sources and their location with respect to the sensors. On the other hand, inverse acoustic tomography's goal [7–12] is to estimate temperature and wind velocity fields given the characteristics of the sound sources, the coordinates of sensors and the travel time for acoustic propagation paths.

The first experiments in inverse acoustic tomography were carried out in the early 1900's in Europe. Large explosions were used as the sound sources, where travel times and angle of arrivals were recorded for sensors located at different distances from the explosions. However, theoretical approaches to inverse acoustic tomography were studied later by Spiesberger and Fristrup [5] for the problem of locating bird's calls based upon the received signatures. They demonstrated that consideration of temperature and wind flow along the sound propagation paths can significantly improve the accuracy of localization. Later, Wilson and Thomson [7] carried out the first acoustic tomography experiment with actual sound sources and microphones to measure the atmospheric surface layer temperature and wind velocity fields. They showed that using acoustic tomography is highly beneficial, as it uses a small number of acoustic sensors to reconstruct the temperature and wind velocity fields with high spatial resolution.

Solving an inverse acoustic tomography problem is in general difficult, owing to its highly nonlinear nature. Several tomographic algorithms have been introduced in different fields to solve the inverse acoustic problem [7, 9, 11]. These tomographic algorithms are commonly categorized as statistical-based algorithms [7, 8, 11, 12], algebraic-based algorithms [9, 10, 17, 18] and those which use sparse reconstruction framework [19].

Wilson and Thomson [7] introduced the first statistical-based algorithm referred to as Stochastic Inversion (SI), to reconstruct the temperature and wind velocity fields. This method is based on using Wiener filter [20] which is inherently linear and assumes that the signal and noise are stationary stochastic processes with known

spectral characteristics or known auto-correlation and cross-correlation. This assumption doesn't hold for an inverse acoustic tomography problem, due to the fact that the process is not only nonlinear but also non-stationary with unknown correlations. However, linearizing the problem and separating it into mean fields and fluctuations, assuming stationarity and using Gaussian functions for the spatial correlations enables the application of the Wiener filtering to reconstruct temperature and wind velocity fields. Vecherin et. al [11, 12] proposed a modified version of SI algorithm referred as time dependent stochastic inversion (TDSI) which uses an augmented vector of several snapshots in time as the observation vector. Similar to SI it employs Wiener filter to reconstruct the fields. The frozen turbulence assumption is also used in TDSI in order to deal with the time extension.

Among the algebraic-based algorithms are the algebraic reconstruction techniques including multiplicative algebraic reconstruction technique (MART) [21] and simultaneous iterative reconstruction technique (SIRT) [9, 13] which solve inverse acoustic problems. These methods use reciprocal sensors and collect two arrival times for each sound ray path, and reformulate the problem linearly. The linear system is then solved by an iterative  $L_2$  norm minimization using gradient-based methods. They start with some arbitrary initial values for the fields and calculate the travel-time along known sound ray paths based on the initial fields. Then, the deviations between the calculated travel-time values and actual measured values are calculated, and adjustments are made to the initial fields until the deviations between forward modeled travel-time values and measured values are small.

Jovanovic et. al. [18] suggested a new approach based on sparse reconstruction framework. This approach studies two different kinds of sparsity, namely sparsity in signal domain which assumes that the fields are made out of the combination of a few 2D-kernel functions on the specified grid in the investigation area, and the sparsity in Fourier domain for smooth temperature fields. Numerical results showed that [18]

the method works under perfect experimental condition, though there is no result on actual measured data to evaluate the real performance of this method.

### 1.2.1 Proposed Method

In this thesis, a new statistical-based approach toward solving the inverse acoustic tomography problem is presented which casts the problem as a nonlinear state-estimation problem. The investigation field is discretized into several grids where the temperature and wind velocity fields are assumed to be constant in each grid. The states are the temperature and wind velocity fields in each grid over the monitored area. The TOA measurements are used as the observations, and the state evolution and observation equations are formed based on the underlying physics of the problem. The mean temperature and wind velocity fields are calculated from the measured TOAs and are fed to the Kalman filter as the initial states to start the state estimation process.

Due to the nonlinearity of the observation equation (i.e. observation vector is a nonlinear function of the states), Unscented Kalman Filter (UKF) [22–24] had to be employed to estimate and track the changes in the states at every snapshot. UKF is based on Unscented Transform method [25] which represents a derivative-free alternative to the extended Kalman filter (EKF) [26]. The latter uses linearization of the state and observation equations which leads to the first order approximation of the nonlinear system. UKF’s performance has been shown [24] to surpass that of EKF at an equivalent or even lesser computational complexity.

Different models, namely a random walk, a first order 3-D spatial autoregressive (AR), and a third order 1-D temporal AR models are used and benchmarked to capture spatial-temporal dynamics of the temperature and wind velocity fields. The state evolution equation is formed based on each model, and the results are compared in terms of reconstruction accuracy and computational complexity. It was shown that

the first order 3-D AR model provides the best overall results and hence was used in subsequent experiments.

To test the UKF-based acoustic tomography, a synthetic data set was generated based on fractal Brownian motion (fBm). Then, the TOAs were calculated for the data set. In order to make the synthetic data more realistic, a white Gaussian noise was added to the calculated TOAs to account for the measurement errors. The temperature and wind velocity fields are then reconstructed using a fixed point iterative UKF, using three iterations on each snapshot.

The results indicate that the proposed method offers a robust and accurate solution to the inverse acoustic tomography problem when compared to the existing TDSI method. Due to the nature of the UKF the proposed method can be applied to many applications where near real-time monitoring of the investigation area is needed. In addition, unlike the SI, TDSI, and SIRT methods there is no need for linearization of the observation equation [7, 11] or using reciprocal sensors [9]. Moreover, the Wiener filter used in [7, 11, 12] for the temperature and wind velocity field reconstruction assumes stationarity of the data which is not realistic. This assumption is lifted in the proposed UKF-based acoustic tomography method.

### **1.3 Organization of the Thesis**

This thesis is organized as follows. Chapter 2 reviews the acoustic tomography inverse problem formulation and reviews several existing acoustic tomography approaches such as statistical inversion (SI), time dependent statistical inversion (TDSI), simultaneous iterative reconstruction technique (SIRT), and an acoustic tomography method based on the compressed sensing framework. Chapter 3 reviews formulations of the UKF for state estimation, parameter estimation, and dual state-parameter estimation. The acoustic tomography is cast into a state estimation problem and the proposed UKF-based acoustic tomography method is described in detail in Chapter 4. Chapter

5 describes the fundamentals of the fractal Brownian motion (fBm) and explains the synthetic data generation process using this method. The proposed method is tested both on the synthetic and real data sets acquired from the University of Leipzig, collected at the Meteorological Observatory, Lindenberg, Germany, as part of the STINHO project [27], and compared to the well-known TDSI method in Chapter 6. Finally, Chapter 6 gives conclusion and ideas for future work.

# CHAPTER 2

## REVIEW OF DIFFERENT TOMOGRAPHY METHODS

### 2.1 Introduction

The problem of reconstructing the continuous temperature and wind velocity fields from finite TOA measurements is inherently an underdetermined problem. Solving such a problem usually requires several simplifying assumptions about the temperature and wind velocity fields, i.e. assuming that the fields are spatially and temporally stationary.

Algorithms dealing with acoustic tomography of the atmosphere, namely stochastic inversion (SI) [7], time dependent stochastic inversion (TDSI) [11], simultaneously iterative recursive technique (SIRT) [9], and acoustic tomography based on sparse reconstruction [18] use several simplifying assumptions in order to reconstruct the temperature and wind velocity fields. One common step among all these algorithms is discretization of the investigation field. In order to be able to solve the acoustic tomography problem numerically, the investigation area is discretized into grid cells, and the fields are reconstructed at the chosen grid points. Using the gridding system requires that the temperature and wind velocity fields be constant in every cell. This implies that the fields are perfectly correlated between every pair of points in a cell while they are less correlated or uncorrelated with the points in other cells. The step behavior of the correlation function, introduced by the gridding process, is unrealistic in fluid mechanics because it forces a discontinuous solution on a continuous field.

The forward formulation of the TOA for an acoustic ray is nonlinear and generally

speaking working with nonlinear models is onerous. Hence, most inverse algorithms use simplified linear models and solve the inverse problem based on these models. SI and TDSI algorithms [7, 11] assume that the wind velocity is much less than the Laplace sound speed and also the temperature fluctuations are much less than the mean temperature throughout the field and employ the first order linear approximation of the forward model to reconstruct the temperature and wind velocity fields. SIRT method [9], on the other hand, uses reciprocal sensors and reformulate the nonlinear problem into two linear problems using the reciprocal measurements.

SI and TDSI algorithms use Wiener filter [20] in order to reconstruct the temperature and wind velocity fields. Solving the problem using Wiener filter, requires temperature and wind velocity temporal and spatial covariance functions. The main difficulty in setting up SI and TDSI is that the correlation functions for atmospheric temperature and wind velocity fields are unknown, therefore the optimal stochastic inverse is not feasible in real-world scenarios. However, SI and TDSI assume the fields are stationary, and use realistic models for the correlation functions in order to reconstruct the fields. SIRT method [9], reconstructs temperature and wind velocity fields separately using a gradient based iterative  $\ell_2$  minimization algorithm. Compared to SI and TDSI, SIRT uses less additional assumptions about the structure of the temperature and wind velocity fields which makes it more suitable for real-world problems.

SI reconstructs the fields at each snapshot using the measured TOAs for the same snapshot while TDSI uses previous measurements as well as the current measurements to reconstruct the fields. Employing several snapshots requires using the spatial-temporal temperature and wind velocity correlation functions. TDSI uses the locally frozen turbulence assumption, to deal with the spatial-temporal correlation functions and represents them just based on spatial correlation functions. The locally frozen turbulence hypothesis includes two assumptions about the temporal evolution of the

atmosphere. First, the layers of the temperature (in our case Laplace sound speed) and wind velocity fields are spatially stable through time. Second, these layers are moving with the spatial mean wind velocity.

This chapter explains the formulation of the problem and studies different acoustic tomography methods, namely those in [7, 9, 11, 18] and their inherent assumptions in detail.

## 2.2 Acoustic Propagation Formulation

The travel time for an acoustic wave to propagate from a source to a receiver is a function of temperature, wind velocity (air flow) and humidity along the path [7–12]. Acoustic tomography methods use this relation to reconstruct the temperature and wind velocity in an investigation area based on several travel time measurements between different sources and receivers deployed in an investigation area.

In the absence of wind an acoustic wavefront propagates with the well-known Laplace sound speed [7], given by

$$c_L^2 = \gamma R_a T_{av}, \quad (2.1)$$

where  $\gamma \approx 1.41$  denotes the ratio of specific heat capacities (or adiabatic index) at constant pressure and volume,  $R_a$  is the universal gas constant for dry air and  $T_{av}$  is the acoustic virtual temperature which is related to the thermodynamic temperature  $T_{th}$ , as  $T_{av} = T_{th}(1 + 0.511q)$ , with  $q$  being the specific humidity defined as the ratio of water vapor to moist air [28]. But since the effect of  $q$  is negligible one can write  $T_{av} \approx T_{th}$

In the field experiments though, wind velocity significantly impacts the speed of sound propagation along a specific path. Wind velocity can be formulated as:

$$\mathbf{v}(\mathbf{r}, t) = \alpha(\mathbf{r}, t)\cos(\theta(\mathbf{r}, t))\mathbf{e}_x + \alpha(\mathbf{r}, t)\sin(\theta(\mathbf{r}, t))\mathbf{e}_y, \quad (2.2)$$

where  $\mathbf{e}_x$  and  $\mathbf{e}_y$  are the unit vectors of a 2D-Cartesian coordinate system and  $\mathbf{r} =$

$x\mathbf{e}_x + y\mathbf{e}_y$  is the position vector of a point on the investigation area and  $\alpha(\mathbf{r}, t)$  and  $\theta(\mathbf{r}, t)$  are magnitude and direction of the wind velocity at position  $\mathbf{r}$  and time  $t$ , respectively. Therefore, the sound speed along the sound ray can be defined as:

$$c_{ray}(\mathbf{r}, t) = \mathbf{s} \cdot (c_L(\mathbf{r}, t) \cdot \mathbf{n} + \mathbf{v}(\mathbf{r}, t)), \quad (2.3)$$

where  $\mathbf{s}$  and  $\mathbf{n}$  denote the unit vectors in the direction of sound propagation and normal to the wavefront, respectively. The acoustic rays propagating in the atmosphere, are bent or refracted by gradients of sound speed and wind velocity. A positive sound speed gradient bends the ray downward and a negative sound speed gradient bends it upward. However, these refractions are negligible for sound propagation distances of few hundreds of meters and when the speed of wind is much less than the Laplace sound speed  $c_L$ . Assuming these refractions are negligible will lead to the simplest ray model for acoustic propagation, straight-ray model, which is typically used in most literature and in which  $\mathbf{s}$  and  $\mathbf{n}$  are assumed to be in the same direction, hence  $\mathbf{s} \cdot \mathbf{n} \approx 1$ . Applying this assumption to (2.3) gives:

$$c_{ray}(\mathbf{r}, t) \approx c_L(\mathbf{r}, t) + \mathbf{s} \cdot \mathbf{v}(\mathbf{r}, t). \quad (2.4)$$

Based on (2.4) which is a well-known relation for the effective sound speed [28], the travel time formula for the  $n$ 'th path is defined as:

$$\tau_n(t) = \int_{L_n} \frac{dl}{c_{ray}(\mathbf{r}, t)} = \int_{L_n} \frac{dl}{c_L(\mathbf{r}, t) + \mathbf{s}_n \cdot \mathbf{v}(\mathbf{r}, t)}, \quad (2.5)$$

where the integration is along the  $n$ 'th propagation path,  $L_n$  is the length of the  $n$ 'th propagation path and  $\mathbf{s}_n$  is the unit vector in its direction. In order to be able to estimate the fields in the investigation area, almost all existing methods [7–13, 17] discretize the investigation area, into grids and assume that  $c_L(\mathbf{r}, t)$  and  $\mathbf{v}(\mathbf{r}, t)$  are spatially constant in each grid. Using  $I \times J$  grids, (A.2) can be discretize as:

$$\tau_n(t) = \sum_{i=1}^I \sum_{j=1}^J \frac{d_n(i, j)}{c_L([i, j], t) + \mathbf{s}_n \cdot \mathbf{v}([i, j], t)}. \quad (2.6)$$

Here  $d_n(i, j)$  is the distance  $n$ 'th propagation path travels in the  $(i, j)$ 'th cell,  $c_L([i, j], t)$  and  $\mathbf{v}([i, j], t)$  are the Laplace sound speed and the wind velocity vector in the  $(i, j)$ 'th grid at time  $t$ , respectively. Figure 2.1 shows the gridding process and the parameters used in time of arrival formulation.

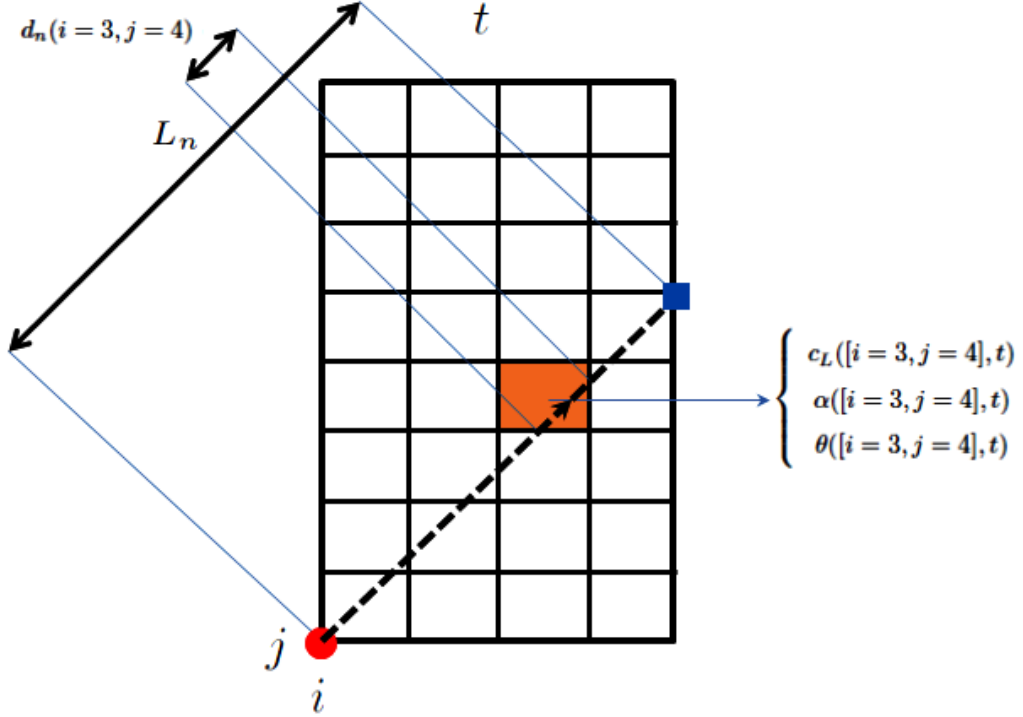


**Figure 2.1:** Gridding and parameters used in travel time formulation.

The term  $\mathbf{s}_n \cdot \mathbf{v}([i, j], t)$  in (A.3) can be written as:

$$\begin{aligned} \mathbf{s}_n \cdot \mathbf{v}([i, j], t) &= \alpha([i, j], t) \cos(\theta([i, j], t)) \cos(\phi_n) + \\ &\quad \alpha([i, j], t) \sin(\theta([i, j], t)) \sin(\phi_n), \end{aligned} \quad (2.7)$$

where  $\alpha([i, j], t)$  and  $\theta([i, j], t)$  are respectively the amplitude and the angle (with respect to  $\mathbf{e}_x$ ) of wind velocity in the  $(i, j)$ th grid at time  $t$  and  $\phi_n$  is the angle of the  $n$ 'th propagation path with  $\mathbf{e}_x$ .

The goal of acoustic tomography is then to find  $c_L([i, j], t)$ ,  $\alpha([i, j], t)$  and  $\theta([i, j], t)$ , for  $i = 1, \dots, I$  and  $j = 1, \dots, J$ , given coordinates of the acoustic transmitters and

receivers deployed in the field and the travel times between each transmitter and receiver,  $\tau_n(t)$ s, recorded for all propagation paths and at each snapshot  $t$ .

The following sections review some of the existing acoustic tomography methods and explain their methodology as well as pros and cons.

## 2.3 Stochastic Inversion (SI) Method

As mentioned before, SI [11, 12] is based on linearizing (A.2) and decomposing temperature and wind velocity fields into spatial mean fields and spatial fluctuation fields. SI uses Cartesian coordinate for wind velocity components and defines

$$v_x(\mathbf{r}, t) = \alpha(\mathbf{r}, t)\cos(\theta(\mathbf{r}, t)) \quad (2.8)$$

$$v_y(\mathbf{r}, t) = \alpha(\mathbf{r}, t)\sin(\theta(\mathbf{r}, t)), \quad (2.9)$$

where  $v_x(\mathbf{r}, t)$  is the wind component in  $\mathbf{e}_x$  direction and  $v_y(\mathbf{r}, t)$  is the wind direction in the  $\mathbf{e}_y$  direction. The Laplace sound speed and wind velocity fields are then decomposed into spatial mean and fluctuation fields.

$$\begin{aligned} c_L(\mathbf{r}, t) &= \bar{c}_L(t) + \tilde{c}_L(\mathbf{r}, t) \\ T_{av}(\mathbf{r}, t) &= \bar{T}_{av}(t) + \tilde{T}_{av}(\mathbf{r}, t) \\ v_x(\mathbf{r}, t) &= \bar{v}_x(t) + \tilde{v}_x(\mathbf{r}, t) \\ v_y(\mathbf{r}, t) &= \bar{v}_y(t) + \tilde{v}_y(\mathbf{r}, t), \end{aligned} \quad (2.10)$$

where  $\bar{c}_L(t)$  is the spatial mean Laplace sound speed and  $\tilde{c}_L(\mathbf{r}, t)$  is the corresponding spatial fluctuations at time  $t$  [7, 11]. Similarly for temperature  $T_{av}(\mathbf{r}, t)$ , wind velocity horizontal component,  $v_x(\mathbf{r}, t)$ , and wind velocity vertical component,  $v_y(\mathbf{r}, t)$ , fields. The steps used in SI are as follow.

### 2.3.1 Linearization Process

Equation (A.2) can be reformulated using (2.10) as follow

$$\begin{aligned}\tau_n(t) &= \int_{L_n} \frac{dl}{c_L(\mathbf{r}, t) + \mathbf{s}_n \cdot \mathbf{v}(\mathbf{r}, t)} \\ &= \int_{L_n} \frac{(\bar{c}_L(t) - (\tilde{c}_L(\mathbf{r}, t) + \mathbf{s}_n \cdot \mathbf{v}(\mathbf{r}, t)))dl}{\bar{c}_L^2(t) - (\tilde{c}_L(\mathbf{r}, t) + \mathbf{s}_n \cdot \mathbf{v}(\mathbf{r}, t))^2}.\end{aligned}\quad (2.11)$$

For low to mid wind velocity we have  $\bar{c}_L(t) \gg (\tilde{c}_L(\mathbf{r}, t) + \mathbf{s}_n \cdot \mathbf{v}(\mathbf{r}, t))$ , then (2.11) can be simplified into

$$\begin{aligned}\tau_n(t) &\approx \int_{L_n} \frac{(\bar{c}_L(t) - (\tilde{c}_L(\mathbf{r}, t) + \mathbf{s}_n \cdot \mathbf{v}(\mathbf{r}, t)))dl}{\bar{c}_L^2(t)} \\ &= \frac{L_n}{\bar{c}_L(t)} - \frac{1}{\bar{c}_L^2(t)} \int_{L_n} (\tilde{c}_L(\mathbf{r}, t) + (\tilde{v}_x(\mathbf{r}, t) + \bar{v}_x(t))\cos(\phi_n) + (\tilde{v}_y(\mathbf{r}, t) + \bar{v}_y(t))\sin(\phi_n))dl \\ &= \frac{L_n}{\bar{c}_L(t)} \left(1 - \frac{\bar{v}_x(t)\cos(\phi_n) + \bar{v}_y(t)\sin(\phi_n)}{\bar{c}_L(t)}\right) - \\ &\quad \frac{1}{\bar{c}_L^2(t)} \int_{L_n} (\tilde{c}_L(\mathbf{r}, t) + \tilde{v}_x(\mathbf{r}, t)\cos(\phi_n) + \tilde{v}_y(\mathbf{r}, t)\sin(\phi_n))dl.\end{aligned}\quad (2.12)$$

Assuming that the temperature fluctuations are small in comparison to the mean temperature,  $\bar{T}_{av}(t) \gg \tilde{T}_{av}(\mathbf{r}, t)$ , and using (2.1) the Laplace sound speed fluctuation field is approximated by

$$\begin{aligned}\tilde{c}_L(\mathbf{r}, t) &= c(\mathbf{r}, t) - \bar{c}(\mathbf{r}, t) = \sqrt{\gamma R_a T_{av}(\mathbf{r}, t)} - \sqrt{\gamma R_a \bar{T}_{av}(t)} \\ &= \sqrt{\gamma R_a \bar{T}_{av}(t)} \left( \sqrt{1 + \frac{\tilde{T}_{av}(\mathbf{r}, t)}{\bar{T}_{av}(t)}} - 1 \right) \approx \frac{\bar{c}(t) \tilde{T}_{av}(\mathbf{r}, t)}{2\bar{T}_{av}(t)},\end{aligned}\quad (2.13)$$

Finally, using (2.13) and (2.12), (A.2) can be linearized as follow

$$\begin{aligned}\tau_n(t) &\approx \frac{L_n}{\bar{c}_L(t)} \left(1 - \frac{\bar{v}_x(t)\cos(\phi_n) + \bar{v}_y(t)\sin(\phi_n)}{\bar{c}_L(t)}\right) - \\ &\quad \frac{1}{\bar{c}_L^2(t)} \int_{L_n} \left( \frac{\bar{c}_L(t) \tilde{T}_{av}(\mathbf{r}, t)}{2\bar{T}_{av}(t)} + \tilde{v}_x(\mathbf{r}, t)\cos(\phi_n) + \tilde{v}_y(\mathbf{r}, t)\sin(\phi_n) \right) dl.\end{aligned}\quad (2.14)$$

Equations (2.14) and (2.12) are the core equations used in the SI method.

### 2.3.2 Spatial Mean Field Estimation

The right side of (2.12) consists of two expressions in which the first expression depends only on the spatial mean fields. Having  $N$  number of paths for all the transmitters and receivers, we form (2.12) for every path. In order to estimate the spatial mean-fields, fluctuations in (2.12) are first neglected (set to zero) in which case the integral vanishes, and the remaining part forms a system of  $N$  (number of paths) linear equations with three unknowns,

$$\underbrace{\begin{bmatrix} 1 & -\cos(\phi_1) & -\sin(\phi_1) \\ 1 & -\cos(\phi_2) & -\sin(\phi_2) \\ \vdots & \vdots & \vdots \\ 1 & -\cos(\phi_N) & -\sin(\phi_N) \end{bmatrix}}_{\Phi} \underbrace{\begin{bmatrix} \frac{1}{\bar{c}_L(t)} \\ \frac{\bar{v}_x(t)}{\bar{c}_L^2(t)} \\ \frac{\bar{v}_y(t)}{\bar{c}_L^2(t)} \end{bmatrix}}_{\mathbf{x}} = \underbrace{\begin{bmatrix} \frac{\tau_1(t)}{L_1} \\ \frac{\tau_2(t)}{L_2} \\ \vdots \\ \frac{\tau_N(t)}{L_N} \end{bmatrix}}_{\mathbf{y}} \quad (2.15)$$

which can easily be solved at time  $t$  for  $N > 3$  by using the least squares (LS) method [20],

$$\hat{\mathbf{x}} = (\Phi^T \Phi)^{-1} \Phi^T \mathbf{y}. \quad (2.16)$$

### 2.3.3 Observation Equation

Employing the mean fields and (2.12), a new observation for the  $n$ 'th path at snapshot  $t$ ,  $q_n(t)$ , is defined as:

$$\begin{aligned} q_n(t) &\triangleq L_n(\bar{c}_L(t) - \bar{v}_x(t)\cos(\phi_n) - \bar{v}_y(t)\sin(\phi_n)) \\ &\quad - \bar{c}_L^2(t)\tau_n(t). \end{aligned} \quad (2.17)$$

Using this new observation,(2.12) is reformulated as

$$\begin{aligned} q_n(t) &= \int_{L_n} (\tilde{c}(\mathbf{r}, t) + \tilde{v}_x(\mathbf{r}, t)\cos(\phi_n) + \tilde{v}_y(\mathbf{r}, t)\sin(\phi_n))dl + \\ &\quad \bar{c}_L^2(t)\epsilon_n(t). \end{aligned} \quad (2.18)$$

where  $\epsilon_n(t)$  represents the effects of the linearization and the measurement errors for the  $n$ th path at time  $t$ .

Discretizing (2.18) into  $I \times J$  grids yields the observation equation as follow:

$$q_n(t) = \sum_{i=1}^I \sum_{j=1}^J d_n(i, j) (\tilde{c}([i, j], t) + \tilde{v}_x([i, j], t) \cos(\phi_n) + \tilde{v}_y([i, j], t) \sin(\phi_n)) + \tilde{c}_L^2(t) \epsilon_n(t). \quad (2.19)$$

### 2.3.4 Wiener Filtering

Wiener filter [20, 29] introduced by Norbert Wiener in the 1940's, is a filter which solves the signal estimation problem for stationary signals. Wiener filter is optimal in minimum mean square error (MMSE) sense. Using (2.19) for all the paths one can write

$$\mathbf{q}(t) = \mathbf{G}\mathbf{m}(t) + \mathbf{n}(t), \quad (2.20)$$

where  $\mathbf{q}(t) = [q_1(t), q_2(t), \dots, q_N(t)]^T$  is the observation vector, the unknown variables are augmented in vector  $\mathbf{m}(t) = [\tilde{\mathbf{c}}_L^T(t), \tilde{\mathbf{v}}_x^T(t), \tilde{\mathbf{v}}_y^T(t)]^T$  to form the vector of Laplace sound speed and wind velocity fields in every grid while  $\tilde{\mathbf{c}}_L(t) = [\tilde{c}_L([1, 1], t), \tilde{c}_L([1, 2], t), \dots, \tilde{c}_L([I, J], t)]^T$ ,  $\tilde{\mathbf{v}}_x^T(t)$  and  $\tilde{\mathbf{v}}_y^T(t)$  are similarly defined, and  $\mathbf{n}(t)$  is the zero-mean observation noise at time  $t$  with known covariance matrix  $R_n$ , and  $\mathbf{G}$  is a known deterministic matrix defined as follow:

$$\mathbf{G} = \begin{bmatrix} \mathbf{d}_1 & \cos(\phi_1)\mathbf{d}_1 & \sin(\phi_1)\mathbf{d}_1 \\ \mathbf{d}_2 & \cos(\phi_2)\mathbf{d}_2 & \sin(\phi_2)\mathbf{d}_2 \\ \vdots & \vdots & \vdots \\ \mathbf{d}_N & \cos(\phi_N)\mathbf{d}_N & \sin(\phi_N)\mathbf{d}_N \end{bmatrix} \quad (2.21)$$

where  $\mathbf{d}_n = [d_n(1, 1), d_n(1, 2), \dots, d_n(I, J)]$ . The purpose of Wiener filter is then to construct a linear estimation in the form

$$\hat{\mathbf{m}}(t) = \mathbf{W}\mathbf{q}(t), \quad (2.22)$$

where  $\hat{\mathbf{m}}(t)$  is an estimate of  $\mathbf{m}(t)$  at time  $t$ . To find the matrix  $W$  the Wiener filter then uses the MMSE criterion,

$$\langle e(t)^2 \rangle = \langle (\mathbf{m}(t) - \hat{\mathbf{m}}(t))^2 \rangle = \langle (\mathbf{m}(t) - W\mathbf{q}(t))^2 \rangle, \quad (2.23)$$

where  $\mathbf{e}(t) = \mathbf{m}(t) - \hat{\mathbf{m}}(t)$  is the estimation error, and  $\langle \cdot \rangle$  is the time averaging process. The estimation error can be minimized by differentiating (2.23) with respect to  $W$  and setting the result to zero.

$$\frac{\partial \langle e(t)^2 \rangle}{\partial W} = \langle 2(\mathbf{m}(t) - W\mathbf{q}(t))\mathbf{q}^T(t) \rangle = 0, \quad (2.24)$$

which gives,

$$W = R_{mq}R_{qq}^{-1}, \quad (2.25)$$

where  $R_{qq} = \langle \mathbf{q}(t)\mathbf{q}^T(t) \rangle$  is the observation covariance matrix of size  $[N, N]$  and  $R_{mq} = \langle \mathbf{m}(t)\mathbf{q}^T(t) \rangle$  is the model-observation cross-covariance matrix of size  $[3IJ, N]$ . In addition  $R_{qq}$  and  $R_{mq}$  can be written as follow

$$R_{mq} = R_{mm}G^T \quad (2.26)$$

$$R_{qq} = GR_{mm}G^T + R_{nn}. \quad (2.27)$$

Here  $R_{mm}$  is the model covariance matrix of size  $[3IJ, 3IJ]$ . SI assumes that  $R_{nn}$  is known and further

$$R_{mm} = \begin{bmatrix} R_{c_L c_L} & \mathbf{0} & \mathbf{0} \\ \mathbf{0} & R_{v_x v_x} & \mathbf{0} \\ \mathbf{0} & \mathbf{0} & R_{v_y v_y} \end{bmatrix} \quad (2.28)$$

where  $R_{c_L c_L}$  is the spatial covariance of size  $IJ \times IJ$  for the Laplace sound speed, and  $R_{v_x v_x}$  and  $R_{v_y v_y}$  are the spatial covariance matrices of horizontal and vertical elements of wind velocity field, respectively. For instance,  $R_{c_L c_L}$  is defined as follow

$$\begin{aligned}
\mathbf{R}_{c_L c_L} &= \langle \mathbf{c}_L(t) \mathbf{c}_L^T(t) \rangle \\
&= \begin{bmatrix} \langle c_L([1, 1], t) c_L([1, 1], t) \rangle & \langle c_L([1, 1], t) c_L([1, 2], t) \rangle & \cdots & \langle c_L([1, 1], t) c_L([I, J], t) \rangle \\ \langle c_L([1, 2], t) c_L([1, 1], t) \rangle & \langle c_L([1, 2], t) c_L([1, 2], t) \rangle & \cdots & \langle c_L([1, 2], t) c_L([I, J], t) \rangle \\ \vdots & \vdots & \ddots & \vdots \\ \langle c_L([I, J], t) c_L([1, 1], t) \rangle & \langle c_L([I, J], t) c_L([1, 2], t) \rangle & \cdots & \langle c_L([I, J], t) c_L([I, J], t) \rangle \end{bmatrix} \quad (2.29)
\end{aligned}$$

where in the SI method it is assumed that the correlation function for  $c_L$  is Gaussian function i.e.

$$\langle c_L(r_k, t) c_L(r_l, t) \rangle = \sigma_{c_L}^2 \exp\left(-\frac{\|r_l - r_k\|^2}{l_{c_L}^2}\right), \quad (2.30)$$

where  $\sigma_{c_L}^2$  is the standard deviation, and  $l_{c_L}$  is the corresponding correlation length of the Laplace sound speed field. Similar assumption holds for  $\mathbf{R}_{v_x v_x}$  and  $\mathbf{R}_{v_y v_y}$  matrices.

Finally SI reconstructs the Laplace sound speed and wind velocity fields at time  $t$  as follow

$$\hat{\mathbf{m}}(t) = \mathbf{R}_{mm} \mathbf{G}^T (\mathbf{G} \mathbf{R}_{mm} \mathbf{G}^T + \mathbf{R}_{nn})^{-1} \mathbf{q}(t). \quad (2.31)$$

## 2.4 Time Dependent Stochastic Inversion (TDSI) Method

The TDSI method is an extension of the SI method introduced by Vecherin et. al. in [11]. It follows the same steps of linearization, spatial mean field estimation, and uses the same observation equation as in SI, but it accumulates  $M$  past snapshots and forms the augmented observation vector,  $\mathbf{q}_a(t) = [\mathbf{q}^T(t-M), \mathbf{q}^T(t-M+1), \dots, \mathbf{q}^T(t)]^T$  to reconstruct vector  $\mathbf{m}(t)$  using the Wiener filter,

$$\hat{\mathbf{m}}(t) = \mathbf{C}_{mq_a} \mathbf{C}_{q_a q_a}^{-1} \mathbf{q}_a(t), \quad (2.32)$$

where  $\mathbf{C}_{mq_a} = \langle \mathbf{m} \mathbf{q}_a^T \rangle$  is the cross-covariance matrix of size  $3IJ \times (M+1)N$  between the fields and the augmented observation vector and  $\mathbf{C}_{q_a q_a} = \langle \mathbf{q}_a \mathbf{q}_a^T \rangle$  is the covariance matrix of the augmented observation vector which is of size  $(M+1)N \times (M+1)N$ .  $\mathbf{C}_{mq_a}$  and  $\mathbf{C}_{q_a q_a}$  are computed as follow

$$\mathbf{C}_{mqa} = \left[ \mathbf{B}_{mq}(t, t-M), \mathbf{B}_{mq}(t, t-M+1), \dots, \mathbf{B}_{mq}(t, t) \right] \quad (2.33)$$

$$\mathbf{C}_{q_a q_a} = \begin{bmatrix} \mathbf{B}_{qq}(t-M, t-M) & \mathbf{B}_{qq}(t-M, t-M+1) & \dots & \mathbf{B}_{qq}(t-M, t) \\ \mathbf{B}_{qq}(t-M+1, t-M) & \mathbf{B}_{qq}(t-M+1, t-M+1) & \dots & \mathbf{B}_{qq}(t-M+1, t) \\ \vdots & \vdots & \ddots & \vdots \\ \mathbf{B}_{qq}(t, t-M) & \mathbf{B}_{qq}(t, t-M+1) & \dots & \mathbf{B}_{qq}(t, t) \end{bmatrix} + \mathbf{R}_{nn} \quad (2.34)$$

where  $\mathbf{B}_{mq}(t_l, t_k) = \langle \mathbf{m}(t_l) \mathbf{q}^T(t_k) \rangle$  is the cross-covariance matrix of size  $3IJ \times N$  between the fields vector  $\mathbf{m}$  at time  $t_l$  and the observation vector  $\mathbf{q}$  at time  $t_k$ , and  $\mathbf{B}_{qq}(t_l, t_k) = \langle \mathbf{q}(t_l) \mathbf{q}^T(t_k) \rangle$  is the covariance matrix of size  $N \times N$  between the observations at time  $t_l$  and  $t_k$ . The noise in the data is assumed to be white Gaussian noise (WGN) and independent of the Laplace sound speed and wind velocity fields, i.e.  $\mathbf{R}_{nn} = \sigma_n^2 \mathbf{I}$ . The elements of  $\mathbf{B}_{mq}(t_l, t_k)$  are defined as follow

$$\begin{aligned} [\mathbf{B}_{mq}(t_l, t_k)]_{ji} &= \langle \mathbf{m}(\mathbf{r}_j, t_l) \mathbf{q}_i(t_k) \rangle \\ &= \int_{L_i} (\langle \mathbf{m}(\mathbf{r}_j, t_l) \tilde{c}_L(\mathbf{r}, t_k) \rangle + \langle \mathbf{m}(\mathbf{r}_j, t_l) \tilde{v}_x(\mathbf{r}, t_k) \rangle \cos(\phi_n) + \langle \mathbf{m}(\mathbf{r}_j, t_l) \tilde{v}_y(\mathbf{r}, t_k) \rangle \sin(\phi_n)) dl \\ &= \begin{cases} \int_{L_i} \mathbf{B}_{c_L c_L}(\mathbf{r}_j, t_l; \mathbf{r}, t_k) dl & \text{if } 1 \leq j \leq IJ, \\ \int_{L_i} (\mathbf{B}_{v_x v_x}(\mathbf{r}_j, t_l; \mathbf{r}, t_k) \cos(\phi_i) + \mathbf{B}_{v_x v_y}(\mathbf{r}_j, t_l; \mathbf{r}, t_k) \sin(\phi_i)) dl & \text{if } IJ+1 \leq j \leq 2IJ, \\ \int_{L_i} (\mathbf{B}_{v_y v_x}(\mathbf{r}_j, t_l; \mathbf{r}, t_k) \cos(\phi_i) + \mathbf{B}_{v_y v_y}(\mathbf{r}_j, t_l; \mathbf{r}, t_k) \sin(\phi_i)) dl & \text{if } 2IJ+1 \leq j \leq 3IJ, \end{cases} \end{aligned} \quad (2.35)$$

where  $\mathbf{B}_{c_L c_L}, \mathbf{B}_{v_x v_x}, \mathbf{B}_{v_x v_y}, \mathbf{B}_{v_y v_x}$ , and  $\mathbf{B}_{v_y v_y}$  are the spatial-temporal covariance/cross-covariance functions of the corresponding fields marked by the subscripts. Similarly, the expression for the covariance matrix  $\mathbf{B}_{qq}(t_l, t_k)$  is defined as

$$\begin{aligned} [\mathbf{B}_{qq}(t_l, t_k)]_{ip} &= \langle \mathbf{q}_i(t_l) \mathbf{q}_p(t_k) \rangle = \int_{L_i} dl \int_{L_p} dl' \{ \mathbf{B}_{c_L c_L}(\mathbf{r}, t_l; \mathbf{r}', t_k) + \\ &\quad \mathbf{B}_{v_x v_x}(\mathbf{r}, t_l; \mathbf{r}', t_k) \cos(\phi_i) \cos(\phi_p) + \mathbf{B}_{v_y v_y}(\mathbf{r}, t_l; \mathbf{r}', t_k) \sin(\phi_i) \sin(\phi_p) + \\ &\quad \mathbf{B}_{v_x v_y}(\mathbf{r}, t_l; \mathbf{r}', t_k) \cos(\phi_i) \sin(\phi_p) + \mathbf{B}_{v_y v_x}(\mathbf{r}, t_l; \mathbf{r}', t_k) \sin(\phi_i) \cos(\phi_p) \}, \end{aligned} \quad (2.36)$$

Similar to the SI method, TDSI assumes the Laplace sound speed and wind velocity fields are statistically stationary. Therefore, all spatial-temporal covariance

matrices only depend on the spatial coordinates and lag. For instance, the Laplace sound speed spatial-temporal covariance  $B_{c_L c_L}(\mathbf{r}, t_l; \mathbf{r}', t_k)$  can be written as

$$B_{c_L c_L}(\mathbf{r}, t_l; \mathbf{r}', t_k) = B_{c_L c_L}(\mathbf{r}, \mathbf{r}', \Delta t) \quad \Delta t = t_k - t_l \quad (2.37)$$

Similarly for  $B_{v_x v_x}, B_{v_x v_y}, B_{v_y v_x}$ , and  $B_{v_y v_y}$ . Based on (2.37) equations (2.33) and (2.34) can be modified as follows:

$$C_{mq_a} = [ B_{mq}(-M), B_{mq}(-M+1), \dots, B_{mq}(0) ] \quad (2.38)$$

$$C_{q_a q_a} = \begin{bmatrix} B_{qq}(0) & B_{qq}(1) & \dots & B_{qq}(M) \\ B_{qq}(-1) & B_{qq}(0) & \dots & B_{qq}(M-1) \\ \vdots & \vdots & \ddots & \vdots \\ B_{qq}(-M) & B_{qq}(-M+1) & \dots & B_{qq}(0) \end{bmatrix} + R_{nn} \quad (2.39)$$

where  $B_{qq}(\Delta t) = B_{qq}(-\Delta t)$  for any  $\Delta t$ .

#### 2.4.1 Frozen Turbulence Assumption

TDSI employs the frozen turbulence assumption to relate the spatial-temporal covariance matrices to the spatial covariance functions. The frozen turbulence assumption states that

$$\mathbf{v}(\mathbf{r}_k, t_k) = \mathbf{v}(\mathbf{r}_k - \bar{\mathbf{v}}(t_l, t_k)\Delta t, t_l) \quad (2.40)$$

$$\mathbf{c}_L(\mathbf{r}_k, t_k) = \mathbf{c}_L(\mathbf{r}_k - \bar{\mathbf{v}}(t_l, t_k)\Delta t, t_l) \quad (2.41)$$

where  $\mathbf{v}(\mathbf{r}_k, t_k) = [v_x(\mathbf{r}_k, t_k), v_y(\mathbf{r}_k, t_k)]^T$  is the wind velocity vector at time  $t_k$  and position  $\mathbf{r}_k$ ,  $\bar{\mathbf{v}}(t_l, t_k) = [\frac{\bar{v}_x(t_l) + \bar{v}_x(t_k)}{2}, \frac{\bar{v}_y(t_l) + \bar{v}_y(t_k)}{2}]^T$ , and  $\Delta t = t_k - t_l$ . Taking into account the frozen turbulence assumption the spatial-temporal covariance functions are then modified accordingly. For instance, spatial-temporal covariance of the Laplace sound speed is given as

$$B_{c_L c_L}(\mathbf{r}_l, \mathbf{r}_k, \Delta t) = B_{c_L c_L}^s(\mathbf{r}_l, \mathbf{r}_k - \bar{\mathbf{v}}(t_l, t_k)\Delta t), \quad (2.42)$$

where  $B_{c_L c_L}^s$  is the spatial covariance matrix of Laplace sound speed field. The other covariances, namely  $B_{v_x v_x}, B_{v_x v_y}, B_{v_y v_x}$ , and  $B_{v_y v_y}$  are modified similarly. Following

Gaussian models are then used as spatial covariance matrices.

$$B_{c_L c_L}^s(\mathbf{r}_l, \mathbf{r}_k) = \sigma_{c_L}^2 \exp\left(-\frac{\|\mathbf{r}_k - \mathbf{r}_l\|^2}{l_{c_L}^2}\right) \quad (2.43)$$

$$B_{v_x v_x}^s(\mathbf{r}_l, \mathbf{r}_k) = \sigma_{v_x}^2 \exp\left(-\frac{\|\mathbf{r}_k - \mathbf{r}_l\|^2}{l^2}\right) \quad (2.44)$$

$$B_{v_y v_y}^s(\mathbf{r}_l, \mathbf{r}_k) = \sigma_{v_y}^2 \exp\left(-\frac{\|\mathbf{r}_k - \mathbf{r}_l\|^2}{l^2}\right) \quad (2.45)$$

$$B_{v_x v_y}^s(\mathbf{r}_l, \mathbf{r}_k) = B_{v_y v_x}^s(\mathbf{r}_l, \mathbf{r}_k) = \sigma_{v_y} \sigma_{v_x} \exp\left(-\frac{\|\mathbf{r}_k - \mathbf{r}_l\|^2}{l^2}\right) \quad (2.46)$$

where  $\sigma_{c_L}, \sigma_{v_x}$ , and  $\sigma_{v_y}$  are the standard deviations of the corresponding fields, and  $l_{c_L}$  and  $l$  are their correlation lengths. Note that different covariance models can be used for spatial covariance of the Laplace sound speed and wind velocity fields. Clearly, more careful choices for these models leads to better reconstruction accuracy of the TDSI.

## 2.5 SIMULTANEOUSLY ITERATIVE RECONSTRUCTION TECHNIQUE (SIRT)

SIRT is one of the well-known algebraic-based methods which is frequently used in acoustic tomography of the atmosphere [9, 13]. Generally speaking, the algebraic-based methods [9, 10, 17, 18, 30, 31], including SIRT, are conceptually much simpler than the statistical-based tomography algorithms. However, comparing to the statistical-based methods, algebraic-based methods are shown to lack accuracy and reconstruction speed [12].

The major benefit of algebraic-based methods is that, they need no initial knowledge about the statistics of the temperature and wind velocity fields. Requiring the minimal number of assumptions and prior knowledge about the fields make algebraic-based solutions, like SIRT, desirable and easy to use.

### 2.5.1 SIRT Formulation

SIRT is an iterative method which solves an overdetermined linear system for the case of noisy observation. A review of the iterative algebraic solutions for a linear system with noisy observations could help to understand and explain SIRT method. Therefore, in the first part of this section we describe these iterative methods. Consider a linear system as

$$\mathbf{G}\mathbf{m} = \mathbf{q} \quad (2.47)$$

where

$$\mathbf{G} = \begin{bmatrix} g_{1,1} & g_{1,2} & \cdots & g_{1,J} \\ g_{2,1} & g_{2,2} & \cdots & g_{2,J} \\ \vdots & \vdots & \ddots & \vdots \\ g_{N,1} & g_{N,2} & \cdots & g_{N,J} \end{bmatrix} \quad (2.48)$$

where  $\mathbf{m} = [m_1; \dots; m_J]$  is the unknown vector to be reconstructed, and  $\mathbf{q} = [q_1, \dots, q_N]^T$  is the observation vector. A solution for  $\mathbf{m}$  can be considered as a single point in a  $J$ -dimensional subspace spanned by  $\langle \mathbf{G} \rangle$ . The intersection of all hyperplanes is a single point when a unique solution exists for this linear system. Figure 2.2 shows the case when  $J = 2$  and  $N = 2$ .

Algebraic reconstruction technique (ART) which is the simplest iterative algebraic reconstruction method starts with an initial estimate  $\mathbf{m}^{(0)} = [m_1^{(0)}; \dots; m_J^{(0)}]$  as the solution for the system. Then, at every step it projects the estimated solution to one of the hyperplanes and uses the projected point as the new estimate. The projection equation at every step is as follow

$$\mathbf{m}^{(k)} = \mathbf{m}^{(k-1)} - \left( \frac{\mathbf{g}_i^T \mathbf{m}^{(k-1)} - q_i}{\mathbf{g}_i^T \mathbf{g}_i} \right) \mathbf{g}_i \quad (2.49)$$

where  $\mathbf{g}_i = [g_{i,1}, \dots, g_{i,J}]^T$  is the  $i$ th row of matrix  $\mathbf{G}$ . It can be shown that if a unique

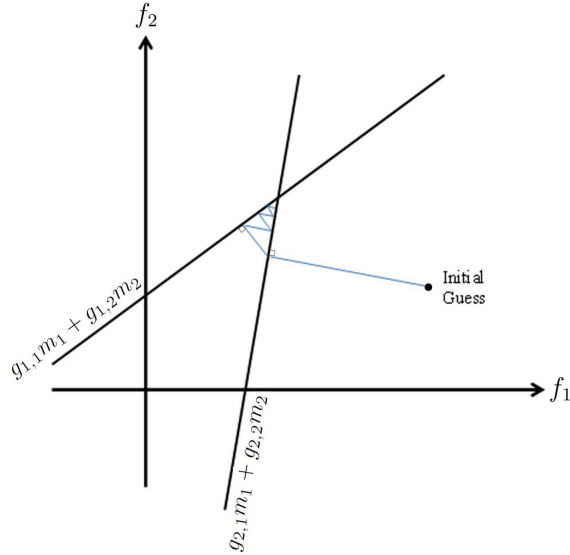


**Figure 2.2:** The simplified problem for  $J = 2$  and  $N = 2$  case using ART.

solution,  $\mathbf{m}_s$ , exists, then ART converges to  $\mathbf{m}_s$  as  $k$  increases, i.e.

$$\lim_{k \rightarrow \infty} \mathbf{m}^{(kN)} = \mathbf{m}_s. \quad (2.50)$$

The speed of convergence depends on the angle between the hyperplanes. Figure 2.2 illustrates the convergence of this method. However, in tomography problems we always end up having an overdetermined noisy system. In this case there is no unique solution to the system and therefore the ART method oscillates around the actual solution. SIRT on the other hand, uses a robust method which can handle the noisy observation. Figure 2.3 demonstrates how SIRT works for  $J = 2$  and  $N = 3$ , it projects the estimated solution to all hyperplanes (red points) and then takes the average of all projected values to be the new estimate (green point).

### 2.5.2 Acoustic Tomography Based on SIRT

For the same experimental setup as in Figure 2.1, the effective sound speed [9, 10] over the  $n$ 'th path is defined, based on the TOA of the path, as follow

$$c_{eff}^n(t) \triangleq \frac{L_n}{\tau_n(t)}, \quad (2.51)$$

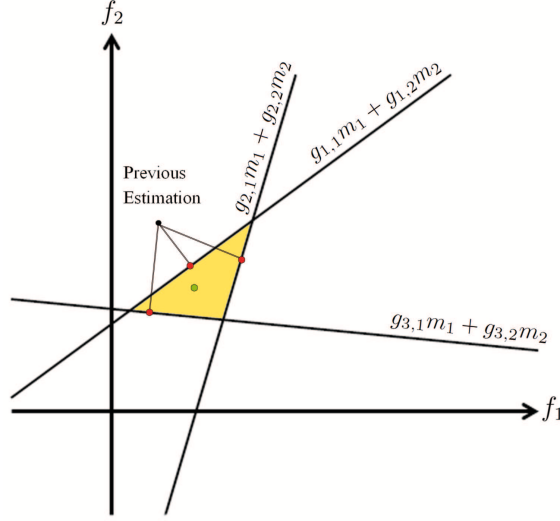


**Figure 2.3:** The simplified problem for  $J = 2$ ,  $N = 3$  and noisy observation using SIRT.

where  $c_{eff}^n(t)$  is the effective sound speed over the  $n$ 'th path at snapshot  $t$ . The effective sound speed can be decomposed into the effective Laplace sound speed and effective wind speed as,

$$c_{eff}^n(t) = c_{L,n}^{eff}(t) + v_n^{eff}(t)$$

$$c_{L,n}^{eff}(t) + v_{x,n}^{eff}(t)\cos(\phi_n) + v_{y,n}^{eff}(t)\sin(\phi_n). \quad (2.52)$$

where  $c_{L,n}^{eff}(t)$ ,  $v_{x,n}^{eff}(t)$ , and  $v_{y,n}^{eff}(t)$  are the effective Laplace sound speed, effective wind velocity horizontal element, and effective wind velocity vertical element, respectively, over the  $n$ 'th path at snapshot  $t$ .

SIRT method uses reciprocal sensors, as in Figure 2.4, which consists of a transmitter and a receiver at every sensor node. Reciprocal sensors are used to isolate the effect of temperature field from the wind velocity fields on the time of arrivals.

An immediate consequence of using reciprocal sensors is having two TOAs for each path, for instance for the  $n$ 'th path at time  $t$  we have  $\tau_{n,1}(t)$  and  $\tau_{n,2}(t)$ . According to (A.8), the effective sound speed for the two opposite directions of the  $n$ 'th path,

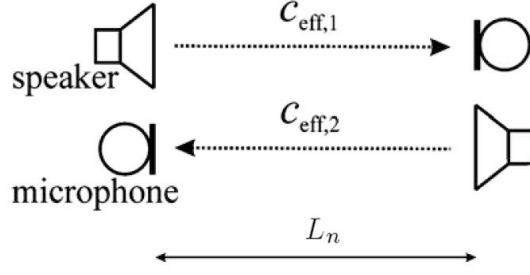


**Figure 2.4:** A reciprocal sensor setup

$c_{eff,1}^n(t)$  and  $c_{eff,2}^n(t)$  in Figure 2.4, are formulated as follow:

$$\begin{aligned} c_{eff,1}^n(t) &= c_{L,n}^{eff}(t) + v_n^{eff}(t) \\ c_{eff,2}^n(t) &= c_{L,n}^{eff}(t) - v_n^{eff}(t). \end{aligned} \quad (2.53)$$

Using (2.53) the temperature and wind velocity fields effects on the TOAs are isolated as follow:

$$\begin{aligned} \frac{c_{eff,1}^n(t) + c_{eff,2}^n(t)}{2} &= c_{L,n}^{eff}(t) \\ \frac{c_{eff,1}^n(t) - c_{eff,2}^n(t)}{2} &= v_n^{eff}(t). \end{aligned} \quad (2.54)$$

Using (A.1), (2.54) can be reformulated as,

$$\begin{aligned} c_{L,n}^{eff}(t) &= \frac{L_n}{2} \left( \frac{1}{\tau_{n,1}(t)} + \frac{1}{\tau_{n,2}(t)} \right) \\ v_n^{eff}(t) &= \frac{L_n}{2} \left( \frac{1}{\tau_{n,1}(t)} - \frac{1}{\tau_{n,2}(t)} \right). \end{aligned} \quad (2.55)$$

That is, the effective temperature and the wind velocity are calculated separately from the reciprocal measurements of TOAs. The new observations are calculated based on (2.55) as follow.

$$\tau_n^c(t) = \frac{L_n}{c_{L,n}^{eff}(t)} = \frac{2\tau_{n,1}(t)\tau_{n,2}(t)}{\tau_{n,2}(t) + \tau_{n,1}(t)} \quad (2.56)$$

$$\tau_n^v(t) = \frac{L_n}{v_n^{eff}(t)} = \frac{2\tau_{n,1}(t)\tau_{n,2}(t)}{\tau_{n,2}(t) - \tau_{n,1}(t)}, \quad (2.57)$$

where  $\tau_n^c(t)$  and  $\tau_n^v(t)$  are the portions of the TOA which only depend on the temperature field and the wind velocity fields for the  $n$ 'th path at snapshot  $t$ , respectively.

These new measurements are then used in (A.2) to relate them to  $c_L(\mathbf{r}, t)$  and  $\mathbf{v}(\mathbf{r}, t)$  as follow:

$$\tau_n^c(t) = \int_{L_n} \frac{dl_n}{c_L(\mathbf{r}, t)} \quad (2.58)$$

$$\tau_n^v(t) = \int_{L_n} \frac{dl_n}{\mathbf{s}_n \cdot \mathbf{v}(\mathbf{r}, t)}. \quad (2.59)$$

Using the gridding process (2.58) and (2.59) are discretized as,

$$\tau_n^c(t) = \sum_{i=1}^I \sum_{j=1}^J \frac{d_n(i, j)}{c_L([i, j], t)} + \epsilon_n^c(t) \quad (2.60)$$

$$\tau_n^v(t) = \sum_{i=1}^I \sum_{j=1}^J \frac{d_n(i, j)}{\mathbf{s}_n \cdot \mathbf{v}([i, j], t)} + \epsilon_n^v(t) \quad (2.61)$$

where  $\epsilon_n^c(t)$  and  $\epsilon_n^v(t)$  represent the observation error as well as the gridding error. Appendix A gives a more detailed discussion on the SIRT assumptions and derivations.

### 2.5.3 Temperature Reconstruction

Slowness is defined as  $m(\mathbf{r}, t) = \frac{1}{c_L(\mathbf{r}, t)}$  and is substituted in (2.60) to form a linear system of equations as,

$$\tau_n^c(t) = \sum_{i=1}^I \sum_{j=1}^J d_n(i, j) m([i, j], t), \quad \text{for } n = 1, \dots, N \quad (2.62)$$

which can be written in Matrix form,

$$\mathbf{q}^c(t) = \mathbf{D}\mathbf{m}(t) \quad (2.63)$$

where  $\mathbf{q}^c(t) = [\tau_1^c(t), \tau_2^c(t), \dots, \tau_N^c(t)]^T$ ,  $\mathbf{m}(t) = [m([1, 1], t), m([1, 2], t), \dots, m([I, J], t)]^T$ , and matrix D is defined as follow

$$\mathbf{D} = \begin{bmatrix} d_1(1, 1) & d_1(1, 2) & \cdots & d_1(I, J) \\ d_2(1, 1) & d_2(1, 2) & \cdots & d_2(I, J) \\ \vdots & \vdots & \ddots & \vdots \\ d_N(1, 1) & d_N(1, 2) & \cdots & d_N(I, J) \end{bmatrix}. \quad (2.64)$$

Then, the SIRT follows the following steps to estimate the temperature in each cell.

1. Set an initial distribution for the slowness values within the grids,  $m^0([i, j], t)$  for  $i = 1, \dots, I$  and  $j = 1, \dots, J$  and form the initial point  $\mathbf{m}^{(0)}(t)$  at time  $t$  (e.g. mean field calculated as it was described before).
2. Estimate the temperature-based TOAs along known sound ray paths using (2.62) according to slowness field estimated in previous iteration,  $m^{(k-1)}(t)$ . (forward modeling)

$$\tau_n^{c,k-1}(t) = \mathbf{d}_n^T \mathbf{m}^{(k-1)}(t), \quad \text{for } n = 1, \dots, N \quad (2.65)$$

where  $\mathbf{d}_n = [d_n(1, 1), d_n(1, 2), \dots, d_n(I, J)]^T$  is the  $n$ 'th row of matrix D. This step is the same as calculating  $\mathbf{g}_i^T \mathbf{m}^{(k-1)}$  in (2.49) for all  $i$ 's.

3. Calculate the projections of  $\mathbf{m}^{(k-1)}(t)$  on all hyperplanes formed by the rows of matrix D.

$$\mathbf{m}_n^{(k)}(t) = \mathbf{m}^{(k-1)}(t) + \frac{(\tau_n^c(t) - \tau_n^{c,k-1}(t))}{\mathbf{d}_n^T \mathbf{d}_n} \mathbf{d}_n \quad \text{for } n = 1, \dots, N \quad (2.66)$$

where  $\mathbf{m}_n^{(k)}$  is the projection of  $\mathbf{m}^{(k-1)}$  on the hyperplane presented by the  $n$ 'th row of matrix D,  $\mathbf{d}_n$ . This step is the same as (2.49).

4. As stated before, SIRT takes the average of all the projections and uses it as the new estimate,  $\mathbf{m}^{(k)}$ .

$$\mathbf{m}_{average}^{(k)}(t) = \frac{1}{N} \sum_{n=1}^N \mathbf{m}_n^{(k)}(t) \quad (2.67)$$

5. In order to make the estimated field spatially consistent, SIRT forces a spatial dependency on the calculated slowness. To do so, at each iteration, after updating slowness of each grid, the spatial field is low-pass filtered with a first order 2D-moving average (MA) filter. For instance, at each iteration the field

is convolved with a filter matrix as follow [9]

$$H = \begin{bmatrix} 0.01 & 0.01 & 0.01 \\ 0.01 & 0.92 & 0.01 \\ 0.01 & 0.01 & 0.01 \end{bmatrix} \quad (2.68)$$

$$m^{(k)}([i, j], t) = \sum_{k_1=1}^3 \sum_{k_2=1}^3 m_{average}^k([i - k_1 + 2, j - k_2 + 2], t) H(k_1, k_2) \quad (2.69)$$

6. Set  $k = k + 1$  and repeat steps 2-5 until the termination criterion is met. The termination criterion is as follow,

$$\|\mathbf{m}^{(k)}(t) - \mathbf{m}^{(k-1)}(t)\|_2 < \epsilon \quad (2.70)$$

where  $\epsilon$  is a constant which determines the accuracy of the solution.

#### 2.5.4 Wind Velocity Reconstruction

A vector tomographic algorithm has to be used to reconstruct the wind velocity field within the area of interest. The SIRT method states that the relationship between the effective wind velocity calculated from the TOAs and the actual wind velocity is as follow

$$\begin{aligned} v_n^{eff}(t) &= \frac{(\cos(\phi_n) \mathbf{d}_n^T)(\cos(\phi_n) \mathbf{v}_x(t))}{\cos(\phi_n) L_n} + \frac{(\sin(\phi_n) \mathbf{d}_n^T)(\sin(\phi_n) \mathbf{v}_y(t))}{\sin(\phi_n) L_n} \\ &= \frac{\mathbf{d}_n^T(\cos(\phi_n) \mathbf{v}_x(t) + \sin(\phi_n) \mathbf{v}_y(t))}{L_n}, \quad \text{for } n = 1, \dots, N \end{aligned} \quad (2.71)$$

where  $\mathbf{v}_x(t) = [v_x([1, 1], t), v_x([1, 2], t), \dots, v_x([I, J], t)]^T$ ,  $\mathbf{v}_y(t) = [v_y([1, 1], t), v_y([1, 2], t), \dots, v_y([I, J], t)]^T$ , and  $\mathbf{d}_n$  is the  $n$ 'th row of matrix D, as defined before.

Equation (2.71) can be written in vector form as follow,

$$\begin{aligned} \mathbf{v}^{eff}(t) &= \begin{bmatrix} (C)(D) & (S)(D) \end{bmatrix} \begin{bmatrix} \mathbf{v}_x(t) \\ \mathbf{v}_y(t) \end{bmatrix} \\ &= \mathbf{Gm}(t). \end{aligned} \quad (2.72)$$

Note that in (2.72) matrix  $\mathbf{G}$  and vector  $\mathbf{m}(t)$  are defined differently from those in (2.20) and (2.21). Also,  $\mathbf{v}^{eff}(t) = [v_1^{eff}(t), v_2^{eff}(t), \dots, v_N^{eff}(t)]^T$ , and  $\mathbf{C}$  and  $\mathbf{S}$  are  $N \times N$  matrices defined as

$$\begin{aligned}\mathbf{C} &= \text{Diag}[\cos(\phi_i)] \\ \mathbf{S} &= \text{Diag}[\sin(\phi_i)]\end{aligned}\tag{2.73}$$

So we can write,

$$\mathbf{v}^{eff}(t) = \mathbf{G}\mathbf{m}.\tag{2.74}$$

SIRT then follows the following steps to estimate the wind velocity fields.

1. Start with initial estimates for the wind velocity horizontal and vertical fields  $v_x^0([i, j], t)$  and  $v_y^0([i, j], t)$ , within the grids, e. g. the mean fields. Note that, the superscript shows the iteration.
2. Estimate the effective wind velocity along known sound ray paths using (2.71), according to the wind velocity horizontal and vertical fields estimated in previous iteration,  $\mathbf{v}_x^{(k-1)}(t)$  and  $\mathbf{v}_y^{(k-1)}(t)$ , respectively.

$$\begin{aligned}v_n^{eff,(k)}(t) &= \frac{\mathbf{d}_n^T(\cos(\phi_n)\mathbf{v}_x^{(k-1)}(t) + \sin(\phi_n)\mathbf{v}_y^{(k-1)}(t))}{L_n}, \quad \text{for } n = 1, \dots, N \\ &= \mathbf{g}_n^T \mathbf{m}^{(k-1)}\end{aligned}\tag{2.75}$$

where  $\mathbf{g}_n^T$  is the  $n$ 'th row of matrix  $\mathbf{G}$ , defined in (2.72) .

3. Calculate the projections of  $\mathbf{m}^{(k-1)}(t)$  on all hyperplanes formed by the rows of matrix  $\mathbf{G}$ .

$$\mathbf{m}_n^{(k)}(t) = \mathbf{m}^{(k-1)}(t) + \frac{(v_n^{eff}(t) - v_n^{eff,k}(t))}{\mathbf{g}_n^T \mathbf{g}_n} \mathbf{g}_n \quad \text{for } n = 1, \dots, N\tag{2.76}$$

where  $\mathbf{m}_n^{(k)}$  is the projection of  $\mathbf{m}^{(k-1)}$  on the hyperplane presented by the  $n$ 'th row of matrix  $\mathbf{G}$ ,  $\mathbf{g}_n$ . This step is the same as (2.49).

4. As stated before, SIRT takes the average of all the projections and uses it as the new estimate,  $\mathbf{m}^{(k)}$ .

$$\mathbf{m}_{average}^{(k)}(t) = \frac{1}{N} \sum_{n=1}^N \mathbf{m}_n^{(k)}(t) \quad (2.77)$$

5. A spatial dependency is forced on the grids as described in temperature reconstruction.
6. Set  $k = k + 1$  and repeat steps 2-5 until the termination criterion is met. The termination criterion is as follow,

$$\|\mathbf{m}^{(k)}(t) - \mathbf{m}^{(k-1)}(t)\|_2 < \epsilon \quad (2.78)$$

where  $\epsilon$  is a constant which determines the accuracy of the solution.

## 2.6 ACOUSTIC TOMOGRAPHY USING SPARSE RECONSTRUCTION FRAMEWORK

Algorithms using sparse reconstruction framework [18] assume that the temperature and wind velocity fields can be represented as a linear combination of some kernel-functions (e.g., set of different bases) where most of the coefficients are zero. In other words they assume that the fields have sparse representation with respect to some known bases. An acoustic tomography algorithm is developed by Jovanovic, et. al. [18], based on sparse reconstruction framework. This section focuses on describing this particular algorithm.

The algorithm in [18] is developed for a numerical experiment in which the wind velocity is set to zero, meaning that it is assumed that the time of arrival measurements are only dependent on the temperature field. Assuming that the wind velocity is zero (2.14) becomes,

$$\tau_n(t) \approx \frac{L_n}{\bar{c}_L(t)} - \frac{1}{\bar{c}_L^2(t)} \int_{L_n} \tilde{c}_L(\mathbf{r}, t) dr. \quad (2.79)$$

Using (2.13) and (2.1), the Laplace sound speed fluctuation,  $\tilde{c}_L(\mathbf{r}, t)$ , can be written as

$$\tilde{c}_L(\mathbf{r}, t) = \frac{\gamma R_a \tilde{T}_{av}(\mathbf{r}, t)}{2\bar{c}_L(t)} \quad (2.80)$$

substituting (2.80) in we have,

$$\tau_n(t) \approx \frac{L_n}{\bar{c}_L(t)} - \frac{2\gamma R_a}{\bar{c}_L^3(t)} \int_{L_n} \tilde{T}_{av}(\mathbf{r}, t) d\mathbf{r}. \quad (2.81)$$

A new observation equation is then defined based on (2.81),

$$q_n(t) \triangleq \frac{\bar{c}_L^3(t)}{2\gamma R_a} \left( \frac{L_n}{\bar{c}_L(t)} - \tau_n(t) \right). \quad (2.82)$$

Using this new observation,  $q_n(t)$ , (2.81) can be reformulated as,

$$q_n(t) = \int_{L_n} \tilde{T}_{av}(\mathbf{r}, t) d\mathbf{r} \quad (2.83)$$

### 2.6.1 Sparsity in Signal Domain

Consider the tomographic problem in which the goal is to reconstruct the temperature field produced by  $K$  localized sources inside the region of interest. An  $I \times J$  grid is overlaid on the investigation area and the temperature field is presented as a linear combination of shifted and normalized kernels  $k(\mathbf{r})$  placed at the center of the grids. Figure 2.5 shows an arbitrary setup with three active heat sources.

It is assumed that there are  $P$  possible candidates for the kernels,  $k_p(\mathbf{r}, t)$  for  $p = 1, \dots, P$ . Note that, for the time being, we assume that  $t$  is not changing and we are solving the problem at snapshot  $t$  without having any knowledge about the previous or later snapshots. Since the kernel functions  $k_1(\mathbf{r}, t), \dots, k_P(\mathbf{r}, t)$  could be at any of  $IJ$  grid centers and there are  $P$  kernel functions, we can write

$$\tilde{T}_{av}(\mathbf{r}, t) = \sum_{i=1}^I \sum_{j=1}^J \sum_{p=1}^P a_{i,j,p} k_p(\mathbf{r} - \mathbf{r}_{i,j}, t), \quad (2.84)$$

where  $a_{i,j,p}$  is the weight of kernel  $p$  at the center of  $[i, j]$ 'th grid. Assuming that the problem is  $K$ -sparse, there are just  $K$  active sources which means that only  $K$  of

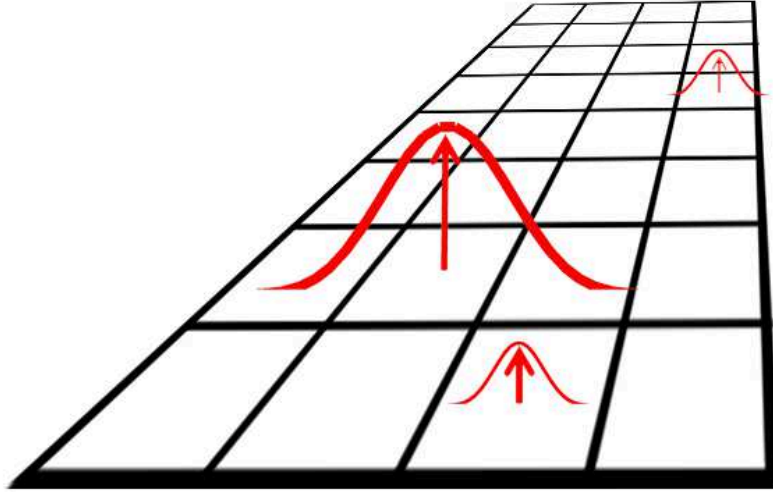


**Figure 2.5:** A sparse distribution of the temperature field in the signal domain, as it originates from 3 local sources placed on the center of the grids.

these kernel weights are nonzero. The goal of this type of acoustic tomography is to estimate these  $K$  nonzero kernel weights from the TOA measurements. Substituting (2.84) into (2.83) we can write,

$$\begin{aligned}
 q_n(t) &= \int_{L_n} \tilde{T}_{av}(t) dr \\
 &= \sum_{i=1}^I \sum_{j=1}^J \sum_{p=1}^P a_{i,j,p} \int_{\Gamma_n} k_p(\mathbf{r} - \mathbf{r}_{i,j}, t) dr.
 \end{aligned} \tag{2.85}$$

Using (2.85) for  $N$  observations we can write,

$$\mathbf{q}(t) = \mathbf{W}(k(t))\mathbf{a} + \mathbf{n}(t), \tag{2.86}$$

where  $\mathbf{q}(t) = [q_1(t), \dots, q_N(t)]^T$  is the observation vector,  $\mathbf{W}(k(t))$  is the dictionary matrix representing  $\int_{L_n} k_p(\mathbf{r} - \mathbf{r}_{i,j}, t) dr$  for all  $p = 1, \dots, P$  and  $n = 1, \dots, N$ ,  $\mathbf{a} = [a_{1,1,1}, \dots, a_{I,J,P}]^T$  is the weight vector which is assumed to be  $K$ -sparse [32, 33], and  $\mathbf{n}(t)$  is the measurement noise. In the absence of noise in (2.86), the sparse signal  $\mathbf{a}$  can be reconstructed by solving an  $\ell_1$  minimization problem [32, 33] as follow,

$$\hat{\mathbf{a}} = \underset{\mathbf{a}}{\operatorname{argmin}} \|\mathbf{a}\|_1 \quad \text{s.t: } \mathbf{q}(t) = \mathbf{W}(k(t))\mathbf{a} \tag{2.87}$$

However, for the linear system with noisy observation the sparse reconstruction solution in (2.87) needs to be modified. A very well-known solution in the case of noisy observation is by solving the minimization problem below,

$$\hat{\mathbf{a}} = \underset{\mathbf{a}}{\operatorname{argmin}}(\|\mathbf{q} - \mathbf{W}(k(t))\mathbf{a}\|_2^2 + \lambda \|\mathbf{a}\|_1) \quad (2.88)$$

where  $\lambda$  is a weighting coefficient which emphasizes on the sparsity aspect of the estimation of  $\mathbf{a}$ . (2.88) can be solved using linear programming [34] or other solvers. However, in order to get a more reliable result, one can employ consequent snapshots and use more observation.

Using consequent snapshots requires knowledge about heat diffusion in the atmosphere. Given that the change of temperature over time in the atmosphere is governed by the heat equation [35], a concentrated deposit of heat diffuses away in a Gaussian manner [35], as described by the 2-D heat kernel,

$$h(\mathbf{r}, t) = \frac{1}{4\pi l_d t} e^{-\frac{\mathbf{r}^T \mathbf{r}}{4l_d t}}, \quad (2.89)$$

where  $l_d$  is the diffusion constant. The investigation field is assumed to be source-free (no heat source), therefore, since there are no active heat sources, the temperature field at time  $t$  can be computed from the convolution of the temperature field at some arbitrary snapshot,  $t_0 < t$ , with the heat kernel as follow

$$\tilde{T}_{av}(\mathbf{r}, t) = \tilde{T}_{av}(\mathbf{r}, t_0) * h(\mathbf{r}, t - t_0). \quad (2.90)$$

Substituting (2.84) in (2.90) we can write,

$$\sum_{i=1}^I \sum_{j=1}^J \sum_{p=1}^P \mathbf{a}_{i,j,p} k_p(\mathbf{r} - \mathbf{r}_{i,j}, t) = \sum_{i=1}^I \sum_{j=1}^J \sum_{p=1}^P \mathbf{a}_{i,j,p} k_p(\mathbf{r} - \mathbf{r}_{i,j}, t_0) * h(\mathbf{r}, t - t_0) \quad (2.91)$$

It follows immediately from (2.91) that the kernel functions at time  $t$  can also be presented by the kernel functions at time  $t_0$  using,

$$k_p(\mathbf{r}, t) = k_p(\mathbf{r}, t_0) * h(\mathbf{r}, t - t_0). \quad (2.92)$$

Note that in (2.92), we are assuming that the location of the kernel functions are not changing in time, which is not a realistic assumption in the presence of wind velocity and in real-world experiments. However, assuming that for a short period of time the position of kernels are fixed, which means that  $\mathbf{a}$  is time independent, one can employ  $M$  past observations and write (2.86) as,

$$\begin{bmatrix} \mathbf{q}(t - M + 1) \\ \vdots \\ \mathbf{q}(t) \end{bmatrix} = \begin{bmatrix} \mathbf{W}(k_{t-M+1}) \\ \vdots \\ \mathbf{W}(k_t) \end{bmatrix} \mathbf{a} + \begin{bmatrix} \mathbf{n}(t - M + 1) \\ \vdots \\ \mathbf{n}(t) \end{bmatrix} \quad (2.93)$$

which can be solved using sparse reconstruction similar to (2.88). It is shown in [18] that using (2.93) instead of (2.86), provides a more accurate temperature reconstruction.

The algorithm doesn't put any constraints on choosing the kernel functions. Jovanovic et al. [18] used 2-D cubic B-splines as the kernel functions to reconstruct the temperature field.

Acoustic tomography of the atmosphere using the sparse reconstruction framework is a new and interesting approach. However, the algorithm still needs further improvements in order to be applied to realistic situations. More specifically, the non-moving atmosphere (zero wind velocity) assumption used in [18] is not a realistic assumption. In addition, since the kernel functions are assumed to be located at the center of each grid, a very fine gridding is needed for this approach, which makes the solution to (2.88) computationally exhaustive.

The issue of sparsity in frequency domain is not addressed here. Interested readers are referred to [18].

## 2.7 Conclusion

In this chapter, the acoustic propagation was formulated. It was shown that the TOA is a nonlinear function of temperature and wind velocity fields. In addition, several

atmospheric acoustic tomography methods were reviewed in detail, and their assumptions were discussed. Acoustic tomography of the atmosphere is an underdetermined nonlinear inverse problem, which is in general difficult to solve. Statistical-based acoustic tomography, such as SI [7] and TDSI [11], use the first order linear approximation of the forward problem and solve the inverse problem applying the Wiener filter to the linearized forward problem. However, using Wiener filter requires knowledge about the statistical characteristics of the temperature and wind velocity fields. Since these characteristics are unknown, optimal stochastic inverse is not generally feasible.

Algebraic-based acoustic tomography methods, such as SIRT [9], are conceptually simpler than the statistical-based tomography algorithms. The major benefit of algebraic-based methods is that, they need no initial knowledge about the statistics of the temperature and wind velocity fields. Requiring minimal number of assumptions and prior knowledge about the fields make algebraic methods suitable for real-world experiments. On the other hand, these methods require reciprocal measurements for every propagation path, which may not be cost-effective and realistic.

Last but not least, are the acoustic tomography algorithms which use the sparse reconstruction framework [18]. These methods are developed recently, and have shown promising results on synthesized data. However, assumptions like non-moving atmosphere and the sparsity of the fields in the atmosphere are not realistic and need to be studied in depth. Moreover, the choices and the number of the kernel functions and the resolution of the gridding system will become of crucial importance in this method. Increasing the number of kernel functions and the resolution of the gridding system, increases the computational cost of these algorithms drastically, hence rendering them impractical for real-life applications.

# CHAPTER 3

## UNSCENTED KALMAN FILTER (UKF)

### 3.1 Introduction

The classical Kalman filter [36] is an optimal recursive estimator which estimates the states from noisy observations. The classical Kalman filter is shown to be the best linear estimator [36] when dealing with linear state space models. However, many interesting and practical applications are modeled with nonlinear state space models, which can not be solved by the classical Kalman filter. Therefore, several extensions of the classical Kalman filter have been developed in order to deal with nonlinear state space models.

Extended Kalman Filter (EKF) [37] and Unscented Kalman Filter (UKF) [24,38] are among these extensions and have been widely applied to nonlinear state estimation problems. EKF uses the first order linear approximation of the state and observation equations around the operation point ( prior state estimates) and solve the linearized problem using the classical Kalman filter. The first order linear approximation can introduce large errors in the estimations of the true posterior mean and covariance of the transformed random variable, which may in turn lead to divergence of the filter.

Unlike EKF, UKF provides a derivative free approach to nonlinear state estimation. UKF employs unscented transform, proposed by Julier and Uhlman [38], to estimate the distribution of a posteriori state. Unscented transform (UT) [22] is a technique which is used to estimate the distribution of a random variable propagating through a known nonlinear function. The idea behind the UT is simple and intuitive, as it states that instead of linearizing the nonlinear function and mapping the distribution using the linear function, one can generate a discrete distribution having

the same first and second (and possibly higher) moments as the initial distribution using a set of deterministic points, called sigma points [39], and transform these sigma points through the nonlinear functions and estimate the distribution based on these transformed sigma points.

In this chapter, the probabilistic inference problem is formulated and reviewed. Furthermore, the UT algorithm is explained and different UKFs are studied for state estimation and dual estimation problems.

### 3.2 Probabilistic Inference

Probabilistic inference is the problem of estimating the hidden variables (state or parameter) of a system (linear or nonlinear) using probability theory given the noisy observations. A probabilistic inference problem can be described by a dynamic state-space model as shown in Figure 3.1.

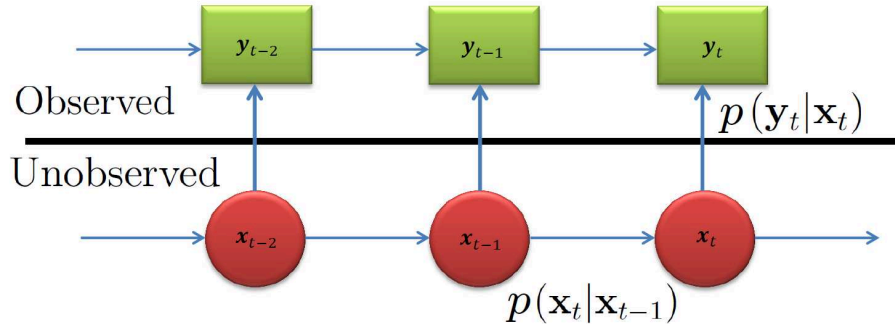


**Figure 3.1:** Graphical model of a probabilistic dynamic state-space model.

The state-space equations for a general system shown in Figure 3.1 are formed as follows.

$$\mathbf{x}_t = \mathbf{f}(\mathbf{x}_{t-1}; \boldsymbol{\rho}_t) + \mathbf{u}_t \quad (3.1)$$

$$\mathbf{y}_t = \mathbf{h}(\mathbf{x}_t; \boldsymbol{\rho}_t) + \mathbf{v}_t, \quad (3.2)$$

Equation (3.1) is the state evolution equation in which  $\mathbf{f}(\cdot)$  captures the state evolution dynamics,  $\mathbf{u}_t$  is the driving noise, and  $\boldsymbol{\rho}_t$  is the model parameter vector.

Equation (3.2) is the observation equation in which  $\mathbf{y}_t$  is the observation at time (snapshot)  $t$ ,  $\mathbf{h}(\cdot)$  is the function which maps the state vector to the observation vector, and  $\mathbf{v}_t$  is the additive observation noise.

The goal of Kalman filter is to estimate the state vector,  $\mathbf{x}_t$ , given all the observation vectors up to  $\mathbf{y}_t$ . The optimal estimate in the sense of minimum mean-squared error (MMSE) is given as follows,

$$\hat{\mathbf{x}}_t = \mathbb{E}[\mathbf{x}_t | \mathbf{z}_t], \quad (3.3)$$

where  $\mathbf{z}_t = \{\mathbf{y}_0, \mathbf{y}_1, \dots, \mathbf{y}_t\}$  represents the set of observation vectors from time 0 to  $t$ . Note that, finding  $\mathbb{E}[\mathbf{x}_t | \mathbf{z}_t]$  requires knowledge of a posteriori density  $p(\mathbf{x}_t | \mathbf{z}_t)$ . Note that, the hidden state  $\mathbf{x}_t$  with initial probability of  $p(\mathbf{x}_0)$ , evolves in time as a first order Markov process [40] according to the conditional density  $p(\mathbf{x}_t | \mathbf{x}_{t-1})$ . In the state-space model in Figure 3.1 the observations are conditionally independent given the states, meaning that if states are observable then  $p(\mathbf{y}_t | \mathbf{z}_t; \mathbf{x}_t) = p(\mathbf{y}_t | \mathbf{x}_t)$ .

Using Bayesian approach and the fact that given that the observations are conditionally independent, one can formulate a recursive equation for the a posteriori density as

$$\begin{aligned} p(\mathbf{x}_t | \mathbf{z}_t) &= \frac{p(\mathbf{x}_t, \mathbf{z}_t)}{p(\mathbf{z}_t)} \\ &= \frac{p(\mathbf{y}_t | \mathbf{z}_{t-1}, \mathbf{x}_t) p(\mathbf{z}_{t-1}, \mathbf{x}_t)}{p(\mathbf{y}_t, \mathbf{z}_{t-1})} \\ &= \frac{p(\mathbf{y}_t | \mathbf{x}_t) p(\mathbf{x}_t | \mathbf{z}_{t-1}) p(\mathbf{z}_{t-1})}{p(\mathbf{y}_t, \mathbf{z}_{t-1})} \\ &= \frac{p(\mathbf{x}_t | \mathbf{z}_{t-1}) p(\mathbf{y}_t | \mathbf{x}_t)}{p(\mathbf{y}_t | \mathbf{z}_{t-1})}, \end{aligned} \quad (3.4)$$

Due to the first order Markovianity of the states we can write,  $p(\mathbf{x}_t | \mathbf{x}_{t-1}, \mathbf{x}_{t-2}, \dots, \mathbf{x}_0) = p(\mathbf{x}_t | \mathbf{x}_{t-1})$  and therefore we have  $p(\mathbf{x}_t | \mathbf{x}_{t-1}, \mathbf{z}_{t-1}) = p(\mathbf{x}_t | \mathbf{x}_{t-1})$ . Now,  $p(\mathbf{x}_t | \mathbf{z}_{t-1})$

in (3.4) can be written as,

$$\begin{aligned}
p(\mathbf{x}_t|\mathbf{z}_{t-1}) &= \frac{p(\mathbf{x}_t, \mathbf{z}_{t-1})}{p(\mathbf{z}_{t-1})} \\
&= \int \frac{p(\mathbf{x}_t, \mathbf{x}_{t-1}, \mathbf{z}_{t-1})}{p(\mathbf{z}_{t-1})} d\mathbf{x}_{t-1} \\
&= \int \frac{p(\mathbf{x}_t|\mathbf{x}_{t-1}, \mathbf{z}_{t-1})p(\mathbf{x}_{t-1}, \mathbf{z}_{t-1})}{p(\mathbf{z}_{t-1})} d\mathbf{x}_{t-1} \\
&= \int p(\mathbf{x}_t|\mathbf{x}_{t-1})p(\mathbf{x}_{t-1}|\mathbf{z}_{t-1})d\mathbf{x}_{t-1} \tag{3.5}
\end{aligned}$$

and the denominator (normalizing constant) in (3.4) is given by

$$\begin{aligned}
p(\mathbf{y}_t|\mathbf{z}_{t-1}) &= \frac{p(\mathbf{y}_t, \mathbf{z}_{t-1})}{p(\mathbf{z}_{t-1})} \\
&= \int \frac{p(\mathbf{y}_t, \mathbf{z}_{t-1}, \mathbf{x}_t)}{p(\mathbf{z}_{t-1})} d\mathbf{x}_t \\
&= \int \frac{p(\mathbf{y}_t|\mathbf{z}_{t-1}, \mathbf{x}_t)p(\mathbf{x}_t, \mathbf{z}_{t-1})}{p(\mathbf{z}_{t-1})} d\mathbf{x}_t \\
&= \int p(\mathbf{y}_t|\mathbf{x}_t)p(\mathbf{x}_t|\mathbf{z}_{t-1})d\mathbf{x}_t \tag{3.6}
\end{aligned}$$

The state transition probability,  $p(\mathbf{x}_t|\mathbf{x}_{t-1})$  is determined by the state evolution equation, and specifically by the density of the driving noise,  $p(\mathbf{u}_t)$ . Similarly,  $p(\mathbf{y}_t|\mathbf{x}_t)$  is determined by the observation noise density,  $p(\mathbf{v}_t)$ . Generally speaking, the integrations in (3.5) and (3.6) are multidimensional integrations, which make a closed form solution of (3.4) intractable. The only general approach in this case is to apply the Monte-Carlo [41] techniques to convert the integrals into finite summations which converge to real solution in the limit. Monte-Carlo techniques are known to be computationally exhaustive, hence they can't be used in the applications where near real-time estimations are needed. However, the Bayesian recursion can be greatly simplified, using the Gaussian distribution assumption for all densities in which case the problem can be solved by Kalman filter [37] for linear state and observation equations.

### 3.3 Unscented Transform

For the nonlinear case, the unscented transform (UT) [22, 25] is a practical estimator to the probability density function of a random variable which undergoes a nonlinear transformation. The idea behind the UT is evolved from the traditional Monte Carlo method. However, in UT instead of drawing a large number of random samples from the a priori distribution, a small number of deterministic samples which have the same first and second order characteristic as the a priori distribution, are used to be transformed through the nonlinear function. In order to clarify the process consider a random vector  $\mathbf{x}$  of size  $L$  with mean  $\bar{\mathbf{x}}$  and covariance  $P_x$ , which undergoes a nonlinear function  $\mathbf{y} = \mathbf{f}(\mathbf{x})$ . To calculate the statistics of  $\mathbf{y}$ , UT defines  $2L + 1$  deterministic samples, in the  $L$  dimensional space, known as sigma points [22] which are defined as

$$\begin{aligned}\boldsymbol{\chi}_0 &= \bar{\mathbf{x}} \\ \boldsymbol{\chi}_i &= \bar{\mathbf{x}} + \gamma\sqrt{P_{x[i]}} \quad i = 1, \dots, L \\ \boldsymbol{\chi}_{L+i} &= \bar{\mathbf{x}} - \gamma\sqrt{P_{x[i]}} \quad i = 1, \dots, L,\end{aligned}\tag{3.7}$$

where  $\gamma = \varrho\sqrt{L + \kappa}$  is a scaling parameter in which the constant  $\varrho$  determines the spread of the sigma points around  $\bar{\mathbf{x}}$  and is set to a small positive value (e.g. ,  $1e-3$ ),  $\kappa$  is the secondary scaling parameter which is usually set to zero, and  $\sqrt{P_{x[i]}}$  is the  $i$ 'th column of the Cholesky factor [42] of  $P_x$ .

These sigma points are then transformed through the nonlinear function  $\mathbf{f}(\cdot)$ , resulting in new sigma points.

$$\boldsymbol{\Upsilon}_i = \mathbf{f}(\boldsymbol{\chi}_i), \quad i = 0, \dots, 2L\tag{3.8}$$

The mean and covariance of  $\mathbf{y}$ ,  $\bar{\mathbf{y}}$  and  $P_y$ , respectively, are estimated from these

transformed sigma points,  $\Upsilon_i$ s as follows,

$$\bar{\mathbf{y}} = \sum_{i=0}^{2L} W_i^{(m)} \Upsilon_i, \quad (3.9)$$

$$\mathbf{P}_y = \sum_{i=0}^{2L} W_i^{(c)} [\Upsilon_i - \bar{\mathbf{y}}][\Upsilon_i - \bar{\mathbf{y}}] \quad (3.10)$$

where the weights  $W_i^{(m)}$ s and  $W_i^{(c)}$ s are [24]  $W_0^{(m)} = \frac{\gamma-L}{\gamma}$ ,  $W_0^{(c)} = \frac{\gamma-L}{\gamma} + (1 - \varrho^2 + \beta)$ , and  $W_i^{(m)} = W_i^{(c)} = \frac{1}{2\gamma}$  for  $i = 1, \dots, 2L$  with  $\beta$  being a constant used to incorporate prior knowledge of the distribution of the state vector and is set to  $\beta = 2$  for Gaussian distributions. Figure 3.2 shows how UT estimates the first and second moments of  $\mathbf{y}$ .

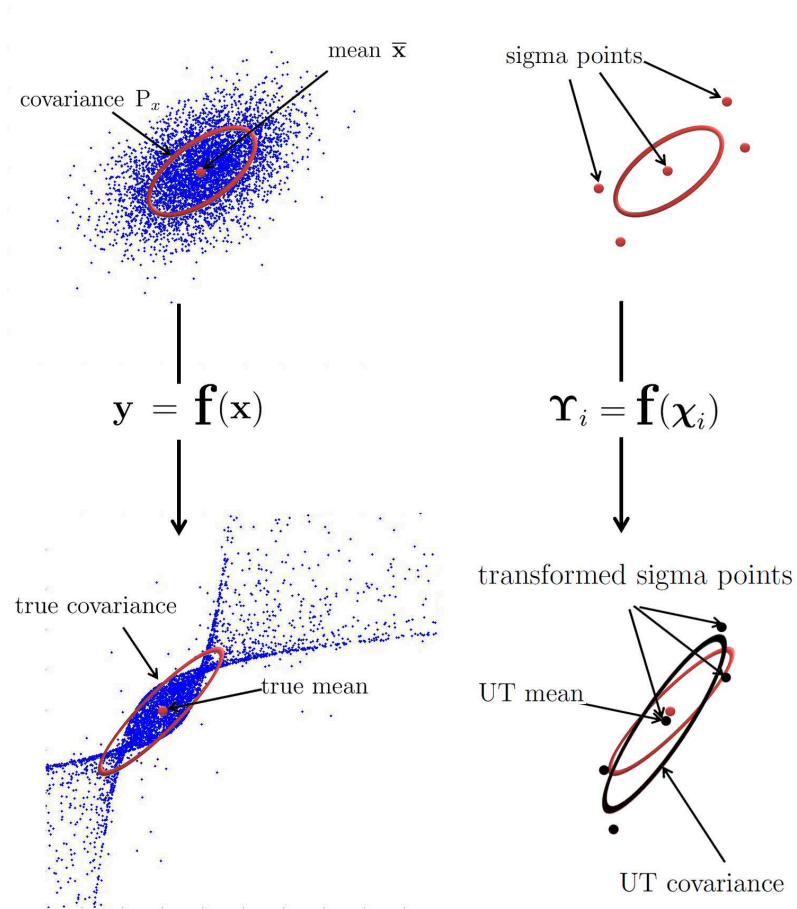


**Figure 3.2:** Demonstration of the UT process.

### 3.4 State Estimation Using UKF

Consider the state-space model in (3.1) and (3.2), if the model parameter vector,  $\boldsymbol{\rho}_t$ , is known but the state is unobserved (hidden), then the problem simplifies to finding the unobserved state  $\mathbf{x}_t$  from the noisy observation  $\mathbf{y}_t$ . Therefore, assuming that the innovation and observation noise vectors  $\mathbf{u}$  and  $\mathbf{v}$ , respectively, are additive in the state-space model the state estimation problem can be reformulated as,

$$\mathbf{x}_t = \mathbf{f}(\mathbf{x}_{t-1}) + \mathbf{u}_t \quad (3.11)$$

$$\mathbf{y}_t = \mathbf{h}(\mathbf{x}_t) + \mathbf{v}_t. \quad (3.12)$$

Note that it is assumed that  $\mathbf{u}_t$  and  $\mathbf{v}_t$  are zero mean with known covariance matrices,  $R_u$  and  $R_v$ , respectively. Given (3.11) and (3.12) the state estimation using Unscented Kalman filter steps are as follows.

1. *Initialization:*

UKF starts with an initial estimate of the state  $\hat{\mathbf{x}}_{0|0}$  and the corresponding covariance matrix  $P_0$ . The expected mean of  $\mathbf{x}$  is typically used as  $\hat{\mathbf{x}}_{0|0}$  and the identity matrix is usually used for  $P_0$ .

2. *Generating Initial Sigma Points:*

As explained in Section 3.3, sigma points are  $2L + 1$  point masses that approximate the state distribution. Using the previous estimations of the state,  $\hat{\mathbf{x}}_{t-1|t-1}$ , and the error covariance matrix,  $P_{t-1|t-1}$ , at time  $t-1$ , the sigma points

are calculated at time  $t$ , as follows

$$\begin{bmatrix} \boldsymbol{\chi}_{0,t-1|t-1} \\ \vdots \\ \boldsymbol{\chi}_{i,t-1|t-1} \\ \vdots \\ \boldsymbol{\chi}_{L+i,t-1|t-1} \\ \vdots \end{bmatrix} = \begin{bmatrix} \hat{\mathbf{x}}_{t-1|t-1} \\ \vdots \\ \hat{\mathbf{x}}_{t-1|t-1} + \gamma \sqrt{\mathbf{P}_{t-1|t-1}[i]} \\ \vdots \\ \hat{\mathbf{x}}_{t-1|t-1} - \gamma \sqrt{\mathbf{P}_{t-1|t-1}[i]} \\ \vdots \end{bmatrix}, \quad i = 1, \dots, L, \quad (3.13)$$

where  $\sqrt{\mathbf{P}_{t-1|t-1}(t)[i]}$  is the  $i$ 'th column of the Cholesky factor of  $\mathbf{P}_{t-1|t-1}$  and  $\gamma$  is defined the same as in the previous section.

### 3. A Priori State Estimation:

The initial sigma points are transformed through the state evolution equation (3.11) to yield,

$$\boldsymbol{\chi}_{i,t|t-1}^* = \mathbf{f}(\boldsymbol{\chi}_{i,t-1|t-1}), \quad i = 0, \dots, 2L \quad (3.14)$$

A weighted sum of these transformed sigma points (see Section 3.3) is calculated to estimate the a priori state,  $\hat{\mathbf{x}}_{t|t-1}$ , and the a priori covariance matrix,  $\mathbf{P}_{t|t-1}$ :

$$\hat{\mathbf{x}}_{t|t-1} = \sum_{i=0}^{2L} W_i^{(m)} \boldsymbol{\chi}_{i,t|t-1}^*, \quad (3.15)$$

$$\mathbf{P}_{t|t-1} = \sum_{i=0}^{2L} W_i^{(c)} [\boldsymbol{\chi}_{i,t|t-1}^* - \hat{\mathbf{x}}_{t|t-1}] [\boldsymbol{\chi}_{i,t|t-1}^* - \hat{\mathbf{x}}_{t|t-1}]^T + \mathbf{R}_u, \quad (3.16)$$

where the weights  $W_i^{(m)}$ s and  $W_i^{(c)}$ s were defined before in Section 3.3.

### 4. Covariance Matrices Computation:

New sigma points are calculated based on the a priori state estimates  $\hat{\mathbf{x}}_{t|t-1}$  and

the a priori error covariance matrix  $P_{t|t-1}$  using

$$\begin{bmatrix} \boldsymbol{\chi}_{0,t|t-1} \\ \vdots \\ \boldsymbol{\chi}_{i,t|t-1}(t) \\ \vdots \\ \boldsymbol{\chi}_{L+i,t|t-1}(t) \\ \vdots \end{bmatrix} = \begin{bmatrix} \hat{\mathbf{x}}_{t|t-1} \\ \vdots \\ \hat{\mathbf{x}}_{t|t-1} + \gamma\sqrt{P_{t|t-1}^{[i]}} \\ \vdots \\ \hat{\mathbf{x}}_{t|t-1} - \gamma\sqrt{P_{t|t-1}^{[i]}} \\ \vdots \end{bmatrix}, \quad i = 1, \dots, L. \quad (3.17)$$

These new sigma points are transformed through the nonlinear observation process (3.12) to yield:

$$\boldsymbol{\Upsilon}_{i,t|t-1} = \mathbf{h}(\boldsymbol{\chi}_{i,t|t-1}) \quad i = 0, \dots, 2L \quad (3.18)$$

which are then used to find estimated observation  $\hat{\mathbf{y}}_{t|t-1}(t)$  and the covariance and cross-covariance matrices  $P_{yy,t}$  and  $P_{xy,t}$  using

$$\hat{\mathbf{y}}_{t|t-1} = \sum_{i=0}^{2L} W_i^{(m)} \boldsymbol{\Upsilon}_{i,t|t-1} \quad (3.19)$$

$$P_{yy,t} = \sum_{i=0}^{2L} W_i^{(c)} [\boldsymbol{\Upsilon}_{i,t|t-1} - \hat{\mathbf{y}}_{t|t-1}] [\boldsymbol{\Upsilon}_{i,t|t-1} - \hat{\mathbf{y}}_{t|t-1}]^T + R_v \quad (3.20)$$

$$P_{xy,t} = \sum_{i=0}^{2L} W_i^{(c)} [\boldsymbol{\chi}_{i,t|t-1} - \hat{\mathbf{x}}_{t|t-1}] [\boldsymbol{\Upsilon}_{i,t|t-1} - \hat{\mathbf{y}}_{t|t-1}]^T \quad (3.21)$$

##### 5. Kalman Gain Computation and A Posteriori State Estimation:

Equations (3.36)-(3.21) for  $\hat{\mathbf{y}}_{t|t-1}$ ,  $P_{yy,t}$ , and  $P_{xy,t}$  are then used to generate the Kalman gain  $K_t$ , the a posteriori state vector  $\hat{\mathbf{x}}_{t|t}$  and the a posteriori error covariance matrix  $P_{t|t}$  using:

$$K_t = P_{xy,t} P_{yy,t}^{-1} \quad (3.22)$$

$$\hat{\mathbf{x}}_{t|t} = \hat{\mathbf{x}}_{t|t-1} + K_t [\mathbf{y}_t - \hat{\mathbf{y}}_{t|t-1}] \quad (3.23)$$

$$P_{t|t} = P_{t|t-1} - K_t P_{yy,t} K_t^T \quad (3.24)$$

The process is repeated until all data points are recursively processed.

UKF provides an optimum estimate in the MMSE sense for the state vector at every snapshot.

### 3.5 Dual Estimation Problem

In a state-space model if the state and the model parameters are both unknown, then the problem of estimating the state and the model parameters is known as a dual estimation problem. There are two extensions of UKF [43–45] which can be used to solve the dual estimation problem, known as dual UKF [43] and joint UKF [44].

In the dual UKF [43], two decoupled UKFs run simultaneously, one for state estimation and the other for the parameter estimation. At every time snapshot the current estimate of the model parameter vector is used in the state estimation whereas the current estimate of the state vector is used in the parameter estimation. Therefore, the filters can be formulated as follows,

$$\text{State filter: } \begin{cases} \mathbf{x}_t = \mathbf{f}(\mathbf{x}_{t-1}; \hat{\boldsymbol{\rho}}_{t-1|t-1}) + \mathbf{u}_t \\ \mathbf{y}_t = \mathbf{h}(\mathbf{x}_t) + \mathbf{v}_t \end{cases} \quad (3.25)$$

$$\text{Parameter filter: } \begin{cases} \boldsymbol{\rho}_t = \boldsymbol{\rho}_{t-1} + \mathbf{n}_t \\ \mathbf{y}_t = \mathbf{h}(\mathbf{f}(\hat{\mathbf{x}}_{t-1|t-1}; \boldsymbol{\rho}_t)) + \mathbf{v}_t \end{cases} \quad (3.26)$$

The schematic of the dual UKF is demonstrated in Figure 3.3.

Note that in the dual UKF the model parameter and the state vectors are assumed to be uncorrelated,  $\mathbf{P}_{\rho x} = \mathbf{P}_{x\rho} = 0$ . The primary benefit of dual estimation is the ability to temporarily decouple the parameter filter from the state filter as needed. Decoupling can prevent erratic behavior due to poor measurements or initial estimate of the parameter estimation from causing the state filter to diverge.

The joint UKF [44], on the other hand, uses just one UKF and estimate state and model parameter vectors simultaneously. In the joint UKF approach, the state and the model parameter vectors are concatenated into an augmented state vector,

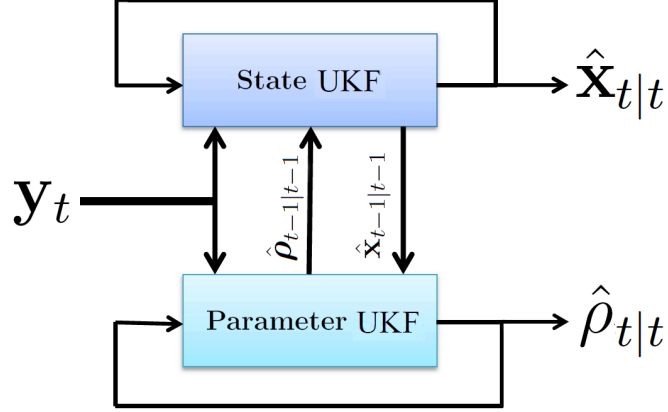


**Figure 3.3:** Schematic of the dual UKF method.

$\mathbf{x}_t^a = [\mathbf{x}_t^T \boldsymbol{\rho}_t^T]^T$ , and hence the state and observation equations are,

$$\mathbf{x}_t^a = \begin{bmatrix} \mathbf{x}_t \\ \boldsymbol{\rho}_t \end{bmatrix} = \begin{bmatrix} \mathbf{f}(\mathbf{x}_{t-1}; \boldsymbol{\rho}_{t-1}) \\ \boldsymbol{\rho}_{t-1} \end{bmatrix} + \begin{bmatrix} \mathbf{u}_t \\ \mathbf{n}_t \end{bmatrix} \quad (3.27)$$

$$\mathbf{y}_t = \mathbf{h}(\mathbf{x}_t) + \mathbf{v}_t. \quad (3.28)$$

Note that in the joint UKF we have

$$P_{x^a} = E[(\mathbf{x}_t^a - \bar{\mathbf{x}}_t^a)(\mathbf{x}_t^a - \bar{\mathbf{x}}_t^a)^T] = \begin{bmatrix} P_{xx} & P_{x\rho} \\ P_{x\rho} & P_{xx} \end{bmatrix}, \quad (3.29)$$

which shows that, unlike the dual UKF, joint UKF can capture the dynamics between the state and model parameter vectors. Therefore, from the modeling point of view, the joint UKF approach is the preferred choice, though the experiments conducted in [39] showed little difference between two approaches. The reason might be due to the fact that switching parameter and state vectors between the dual filters, coupled with using the exact same measurement vector in both filters, acts as a type of constraint on the filters which implicitly develops the cross covariance terms.

## 3.6 Fixed-Point Iterative UKF

In the case of large uncertainty in the choice of the initial error covariance matrix  $P_0$  and weak observability (low SNR or insufficient measurements) of the system, UKF

exhibits slow convergence problem and poor state estimation accuracy. Fixed-point iterative UKF [46] is a more robust version of UKF which not only iterates on every snapshot  $t$  but also performs a fixed-point iteration at each fixed snapshot to get a more robust and accurate state estimates.

In this section, the fixed point iterative UKF is formulated for the state estimation problem. However, the same principle can be extended to the dual estimation problem as well. Defining  $\hat{\mathbf{x}}_{k|k}(t)$  to be the state estimate at  $k$ 'th iteration on snapshot  $t$ , the state estimation using fixed-point iterative UKF steps for  $k \in [0, K]$  iterations on each snapshot  $t$  are:

1. *Initialization:*

Fixed-point iterative UKF starts by initializing the state vector estimate  $\hat{\mathbf{x}}_{K|K}(0)$  (i.e. estimate of state vector, given observation at time  $t = 0$ ). Additionally, the corresponding state error covariance matrix  $P_{K|K}(0)$  is initialized with an identity matrix. The initial state vector at  $t$  is then set to be  $\hat{\mathbf{x}}_{0|0}(t) = \hat{\mathbf{x}}_{K|K}(t - 1)$  and the corresponding covariance matrix  $P_{0|0}(t) = P_{K|K}(t - 1)$ .

2. Generating Initial Sigma Points

Using the initial estimates  $\hat{\mathbf{x}}_{k-1|k-1}(t)$  and  $P_{k-1|k-1}(t)$  for the  $k$ 'th iteration at time  $t$ , the sigma points are calculated as follows

$$\begin{bmatrix} \boldsymbol{\chi}_{0,k-1|k-1}(t) \\ \vdots \\ \boldsymbol{\chi}_{i,k-1|k-1}(t) \\ \vdots \\ \boldsymbol{\chi}_{L+i,k-1|k-1}(t) \\ \vdots \end{bmatrix} = \begin{bmatrix} \hat{\mathbf{x}}_{k-1|k-1}(t) \\ \vdots \\ \hat{\mathbf{x}}_{k-1|k-1}(t) + \gamma \sqrt{P_{k-1|k-1}(t)}_{[i]} \\ \vdots \\ \hat{\mathbf{x}}_{k-1|k-1}(t) - \gamma \sqrt{P_{k-1|k-1}(t)}_{[i]} \\ \vdots \end{bmatrix}, \quad i = 1, \dots, L, \quad (3.30)$$

where  $\gamma$  and  $\sqrt{P_{k-1|k-1}(t)}_{[i]}$  were defined as before.

### 3. A Priori State Estimation:

The initial sigma points are transformed through the state evolution equation (3.11).

$$\boldsymbol{\chi}_{i,k|k-1}^*(t) = \mathbf{f}(\boldsymbol{\chi}_{i,k-1|k-1}(t)), \quad i = 0, \dots, 2L \quad (3.31)$$

A weighted sum of these transformed sigma points is calculated to estimate the a priori state,  $\hat{\mathbf{x}}_{k|k-1}(t)$ , and covariance matrix,  $\mathbf{P}_{k|k-1}(t)$ :

$$\begin{aligned} \hat{\mathbf{x}}_{k|k-1}(t) &= \sum_{i=0}^{2L} W_i^{(m)} \boldsymbol{\chi}_{i,k|k-1}^*(t), \\ \mathbf{P}_{k|k-1}(t) &= \sum_{i=0}^{2L} W_i^{(c)} [\boldsymbol{\chi}_{i,k|k-1}^*(t) - \hat{\mathbf{x}}_{k|k-1}(t)][\boldsymbol{\chi}_{i,k|k-1}^*(t) - \hat{\mathbf{x}}_{k|k-1}(t)]^T + \mathbf{R}_u, \end{aligned} \quad (3.32)$$

$$(3.33)$$

where  $W_i^{(m)}$  and  $W_i^{(c)}$  are defined as before.

### 4. Covariance Matrices Computation:

New sigma points are calculated based on the a priori state estimates  $\hat{\mathbf{x}}_{k|k-1}(t)$  and the a priori error covariance matrix  $\mathbf{P}_{k|k-1}(t)$  i.e.

$$\begin{bmatrix} \boldsymbol{\chi}_{0,k|k-1}(t) \\ \vdots \\ \boldsymbol{\chi}_{i,k|k-1}(t) \\ \vdots \\ \boldsymbol{\chi}_{L+i,k|k-1}(t) \\ \vdots \end{bmatrix} = \begin{bmatrix} \hat{\mathbf{x}}_{k|k-1}(t) \\ \vdots \\ \hat{\mathbf{x}}_{k|k-1}(t) + \gamma \sqrt{P_{k|k-1}(t)}_{[i]} \\ \vdots \\ \hat{\mathbf{x}}_{k|k-1}(t) - \gamma \sqrt{P_{k|k-1}(t)}_{[i]} \\ \vdots \end{bmatrix}, \quad i = 1, \dots, L, \quad (3.34)$$

The new sigma points are transformed through the nonlinear observation process (3.12) to yield:

$$\boldsymbol{\Upsilon}_{i,k|k-1}(t) = \mathbf{h}(\boldsymbol{\chi}_{i,k|k-1}(t)) \quad i = 0, \dots, 2L \quad (3.35)$$

which are then used to find  $\hat{\mathbf{y}}_{k|k-1}(t)$  and the covariance and cross-covariance matrices  $P_{yy,k}(t)$  and  $P_{xy,k}(t)$  using

$$\hat{\mathbf{y}}_{k|k-1}(t) = \sum_{i=0}^{2L} W_i^{(m)} \mathbf{\Upsilon}_{i,k|k-1}(t) \quad (3.36)$$

$$P_{yy,k}(t) = \sum_{i=0}^{2L} W_i^{(c)} [\mathbf{\Upsilon}_{i,k|k-1}(t) - \hat{\mathbf{y}}_{k|k-1}(t)] [\mathbf{\Upsilon}_{i,k|k-1}(t) - \hat{\mathbf{y}}_{k|k-1}(t)]^T + R_v \quad (3.37)$$

$$P_{xy,k}(t) = \sum_{i=0}^{2L} W_i^{(c)} [\mathbf{\chi}_{i,k|k-1}(t) - \hat{\mathbf{x}}_{k|k-1}(t)] [\mathbf{\Upsilon}_{i,k|k-1}(t) - \hat{\mathbf{y}}_{k|k-1}(t)]^T \quad (3.38)$$

### 5. Kalman Gain Computation and A Posteriori State Estimation:

These are then used to generate the Kalman gain  $K_k(t)$ , a posteriori state vector  $\hat{\mathbf{x}}_{k|k}(t)$  and the a posteriori error covariance matrix  $P_{k|k}(t)$  estimations:

$$K_k(t) = P_{xy,k}(t) P_{yy,k}^{-1}(t) \quad (3.39)$$

$$\hat{\mathbf{x}}_{k|k}(t) = \hat{\mathbf{x}}_{k|k-1}(t) + K_k(t) [\mathbf{y}_t - \hat{\mathbf{y}}_{k|k-1}(t)] \quad (3.40)$$

$$P_{k|k}(t) = P_{k|k-1}(t) - K_k(t) P_{yy,k}(t) K_k^T(t) \quad (3.41)$$

### 6. Iteration Step:

If  $k < K$  then the algorithm proceeds to the next iteration  $k + 1$  on the fixed snapshot  $t$  and redo steps 2 to 5. But if  $k = K$ , then proceed in time  $t + 1$  and jumps to step 1.

Figure 3.4 demonstrates the schematic diagram of the fixed-point UKF.

## 3.7 Conclusion

This chapter reviewed the idea behind UKF and its different variations. The Unscented Transform (UT) process was described and utilized to derive the UKF. The original UKF was explained in detail followed by the cases of state estimation and

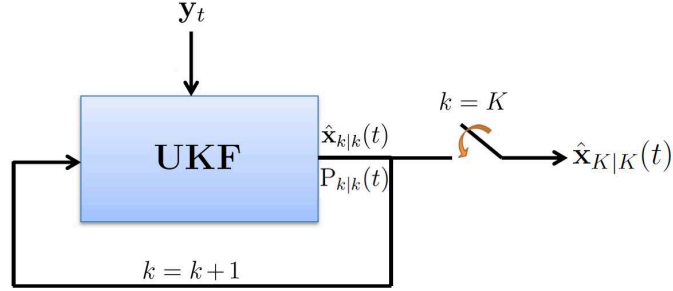


**Figure 3.4:** Fixed point iterative UKF.

dual state-parameter estimation. Finally, the fixed point UKF was introduced to enhance the performance of UKF for the problems with large uncertainty in the choice of the initial error covariance matrix and low SNR or insufficient measurements.

UKF is shown to be an effective method for nonlinear state estimation problems [39]. One should take into account that the performance of UKF highly depends on the accuracy of the state evolution and observation models, as well as on accuracy of covariance matrices, for the driving and measurement noise. Providing good models for state evolution and observation is of the foremost importance in the UKF. However, for some real-world applications, like the temperature and wind velocity evolution in the atmosphere, the state evolution model is unknown or it depends on many different stochastic parameters. In this case, one should use the dual state-parameter estimation UKF to estimate the state and model parameters simultaneously from the observations.

Compared with the standard UKF, the fixed point iterated UKF can adjust the state estimates to adaptively approach the true values through corrections calculated based on a single measurement. The fixed point UKF is adopted in the next chapters for state estimation as well as dual state-parameter estimation.

# CHAPTER 4

## UKF-BASED ACOUSTIC TOMOGRAPHY

### 4.1 Introduction

In this chapter a new statistical-based approach is proposed for the acoustic tomography of the atmosphere using the UKF reviewed in Chapter 3 instead of using Wiener filter traditionally used in the existing methods such as those in [7] and [11]. Similar to most acoustic tomography algorithms the gridding system is employed to discretize the monitored area into several grids in which the temperature, wind velocity amplitude, and wind velocity angle are assumed to be constant. The problem is then framed as a state estimation problem where state variables are temperature and wind velocity elements in every grid.

Different linear state evolution models, using random walk, first order 3-D autoregressive (AR), and 1-D temporal AR models, are tried to capture the dynamics of the state evolution. The time of arrival (TOA) measurements from all the sensors in the field are used as the observations forming collectively the observation equation. Owing to the nonlinearity of the observation equation UKF is employed for this state estimation problem.

In this chapter the UKF-based acoustic tomography of the atmosphere is formulated and three different state evolution models are studied. The proposed method is capable of providing a robust temperature and wind velocity reconstruction and due to the nature of UKF it is capable of tracking these fields over time.

## 4.2 Formulation

As mentioned in Chapter 2 the deployment field is divided into non-overlapping grids as shown in Figure 2.1. The Laplace sound speed, wind velocity amplitude and wind velocity angle at all grids are arranged to form the  $L = 3IJ$ -dimensional state vector as

$$\mathbf{x}_t = [\mathbf{c}_L^T(t), \boldsymbol{\alpha}^T(t), \boldsymbol{\theta}^T(t)]^T, \quad (4.1)$$

where  $\mathbf{c}_L(t) = [c_L([1, 1], t), c_L([1, 2], t), \dots, c_L([I, J], t)]^T$  is the column vector of the Laplace sound speed at every grid, and similarly for  $\boldsymbol{\alpha}(t)$  and  $\boldsymbol{\theta}(t)$ . The observation vector,  $\mathbf{y}_t$ , on the other hand, consists of TOA measurements for all acoustic propagation paths. That is,

$$\mathbf{y}_t = [\tau_1(t), \dots, \tau_N(t)]^T, \quad (4.2)$$

where  $\tau_i(t)$  is the travel time for the  $i$ 'th path at snapshot  $t$ .

### 4.2.1 State Evolution Process

The state evolution equation in this case is assumed to be linear but unknown. Three different linear models are studied and tested to determine their success in capturing the state dynamics. These models are explained next.

#### (a) *Random Walk Model*

Assuming that the fields don't follow certain dynamical behavior, snapshot to snapshot variations can simply be captured by a random walk model [47]. In this case state equation can be written as:

$$\mathbf{x}_t = \mathbf{x}_{t-1} + \mathbf{u}_t. \quad (4.3)$$

One should expect a trade off between simplicity of the model and accuracy of the reconstruction using UKF. The complexity of the model should match the complexity of the state evolution. For instance, using an oversimplified model for a complex

system can lead to poor state estimation, and using an elaborate model to capture the dynamics of a simple system can cause overfitting problems. Nonetheless, this random walk model appears to be a good fit to the wind velocity angle component, due to erratic behavior of this component.

(b) *First Order 3-D AR Model*

A more representative model to capture the state dynamics of the system is an spatial-temporal autoregressive (AR) model. The adjacent neighbors at time  $t - 1$  are used as the support region for each grid at time  $t$ . The state evolution equation for the Laplace sound speed at a specific grid  $[i, j]$  is defined as follow

$$\begin{aligned}
c_L([i, j], t) = & \rho_0^{c_L} c_L([i, j], t - 1) + \rho_1^{c_L} (c_L([i + 1, j], t - 1) + c_L([i, j + 1], t - 1) + \\
& c_L([i - 1, j], t - 1) + c_L([i, j - 1], t - 1)) + \rho_2^{c_L} (c_L([i - 1, j - 1], t - 1) + \\
& c_L([i - 1, j + 1], t - 1) + c_L([i + 1, j - 1], t - 1) + c_L([i + 1, j + 1], t - 1)) + \\
& u_c([i, j], t),
\end{aligned} \tag{4.4}$$

where  $\rho_0^{c_L}$ ,  $\rho_1^{c_L}$  and  $\rho_2^{c_L}$  are the AR model coefficients and  $u_c([i, j], t)$  is the deriving noise which represents the inaccuracies in the modeling of the state evolution in time. Figure 4.1 shows the support region of the discretized 3-D AR model for the Laplace sound speed field at time  $t$ . Note that around the boundaries the support region of a cell is reduced to its neighbors in the investigation area. For the cells around the boundaries, the neighbors that are outside the investigation area are set to zero.

The AR model for the Laplace sound speed can then be written in state equation vector form as

$$\mathbf{c}_L(t) = \mathbf{A}^{(c_L)} \mathbf{c}_L(t - 1) + \mathbf{u}_{c_L}(t) \tag{4.5}$$

where  $\mathbf{u}_{c_L}(t) = [u_{c_L}([1, 1], t), \dots, u_{c_L}([I, J], t)]^T$  is the column vector of the Laplace sound speed deriving process. Matrix  $\mathbf{A}^{(c_L)}$  is a block Toeplitz matrix with Toeplitz blocks, and is defined as the right-stochastic (each row is normalized by the sum of

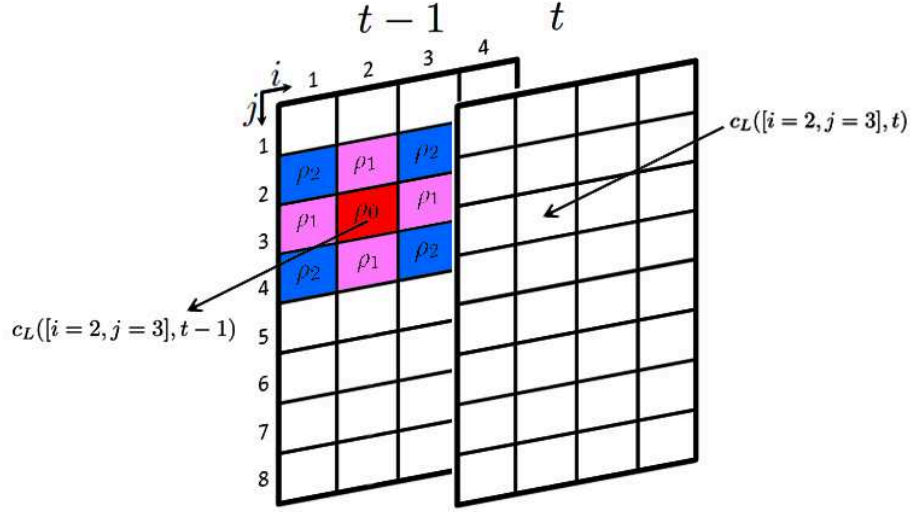


**Figure 4.1:** The support region of a 1st spatial-temporal order AR model.

the elements to account for the cells around the boundaries) of the matrix  $A^{(c_L)}$  which for a  $4 \times 8$  grid is defined as,

$$A^{(c_L)} \triangleq \begin{bmatrix} B & C & 0 & 0 & 0 & 0 & 0 & 0 \\ C & B & C & 0 & 0 & 0 & 0 & 0 \\ 0 & C & B & C & 0 & 0 & 0 & 0 \\ 0 & 0 & C & B & C & 0 & 0 & 0 \\ 0 & 0 & 0 & C & B & C & 0 & 0 \\ 0 & 0 & 0 & 0 & C & B & C & 0 \\ 0 & 0 & 0 & 0 & 0 & C & B & C \\ 0 & 0 & 0 & 0 & 0 & 0 & C & B \end{bmatrix}, \quad (4.6)$$

and B and C block matrices are defined as

$$\mathbf{B} = \begin{bmatrix} \rho_0^{cL} & \rho_1^{cL} & 0 & 0 \\ \rho_1^{cL} & \rho_0^{cL} & \rho_1^{cL} & 0 \\ 0 & \rho_1^{cL} & \rho_0^{cL} & \rho_1^{cL} \\ 0 & 0 & \rho_1^{cL} & \rho_0^{cL} \end{bmatrix}, \quad (4.7)$$

$$\mathbf{C} = \begin{bmatrix} \rho_1^{cL} & \rho_2^{cL} & 0 & 0 \\ \rho_2^{cL} & \rho_1^{cL} & \rho_2^{cL} & 0 \\ 0 & \rho_2^{cL} & \rho_1^{cL} & \rho_2^{cL} \\ 0 & 0 & \rho_2^{cL} & \rho_1^{cL} \end{bmatrix}. \quad (4.8)$$

The AR coefficients  $\rho_0^{cL}, \rho_1^{cL}$  and  $\rho_2^{cL}$  can be estimated using different approaches. The first approach is to use a training data set and estimate the parameters based on the Yule-Walker method [48] or run a parameter estimation UKF/EKF on the training data. However, using the training data to estimate the model parameters is not a feasible solution for realistic cases, due to the need for a large number of in-situ measurements. In addition, using a limited training data to estimate the model parameters doesn't apply to the cases in which the model parameters are changing in time. The second approach is to use the dual estimation UKF method explained in Section 3.5. And finally the third approach is to assume known covariance models and use the associated generic model parameters.

Similar relationship as (4.5) holds for the wind velocity amplitude,  $\boldsymbol{\alpha}(t)$ , and wind velocity angle,  $\boldsymbol{\theta}(t)$ . Thus, we have

$$\begin{aligned} \boldsymbol{\alpha}(t) &= \mathbf{A}^{(\alpha)} \boldsymbol{\alpha}(t-1) + \mathbf{u}_\alpha(t), \\ \boldsymbol{\theta}(t) &= \mathbf{A}^{(\theta)} \boldsymbol{\theta}(t-1) + \mathbf{u}_\theta(t). \end{aligned} \quad (4.9)$$

Here  $\mathbf{u}_\alpha(t)$  and  $\mathbf{u}_\theta(t)$  are, respectively the driving processes for amplitude and the angle of wind velocity and matrix  $\mathbf{A}^{(\alpha)}$  and  $\mathbf{A}^{(\theta)}$  are defined in a similar manner as  $\mathbf{A}^{(cL)}$ . Note that the AR models are assumed to be decoupled from each other

as the phenomena that generate them are independent. Combining these decoupled equations yields the following linear state equation,

$$\mathbf{x}_t = \mathbf{A}\mathbf{x}_{t-1} + \mathbf{u}_t, \quad (4.10)$$

where  $\mathbf{u}_t = [\mathbf{u}_{c_L}(t)^T, \mathbf{u}_\alpha(t)^T, \mathbf{u}_\theta(t)^T]^T$  is the augmented deriving noise vector which is assumed to be Gaussian with zero mean and known covariance matrix,  $R_u$  and matrix  $\mathbf{A}$  is

$$\mathbf{A} = \begin{bmatrix} \mathbf{A}^{(c_L)} & \mathbf{0}_{IJ \times IJ} & \mathbf{0}_{IJ \times IJ} \\ \mathbf{0}_{IJ \times IJ} & \mathbf{A}^{(\alpha)} & \mathbf{0}_{IJ \times IJ} \\ \mathbf{0}_{IJ \times IJ} & \mathbf{0}_{IJ \times IJ} & \mathbf{A}^{(\theta)} \end{bmatrix}. \quad (4.11)$$

where  $\mathbf{0}_{IJ \times IJ}$  is the zero matrix of size  $IJ \times IJ$ . Note that the model parameter vector is then defined to be

$$\boldsymbol{\rho}_t = [\rho_0^{c_L}(t), \rho_1^{c_L}(t), \rho_2^{c_L}(t), \rho_0^\alpha(t), \rho_1^\alpha(t), \rho_2^\alpha(t), \rho_0^\theta(t), \rho_1^\theta(t), \rho_2^\theta(t)]^T \quad (4.12)$$

(c) *1-D Temporal AR Model*

There is a concern about the feasibility of using a first order 3-D AR model to capture the dynamic of the state evolution process in field-experiments. More specifically, there is no guarantee that the spatial dependency be consistent throughout the investigation field, especially when the turbulence is local and strong. As a result, we decided to explore a different model to capture the dynamic of the state evolution process temporally but not spatially in contrast to the previous model.

Since the fields are changing consistently in time it is beneficial to look into the fields at times  $t - 2$  and  $t - 3$  as well as time  $t - 1$ . Therefore, we devised a new 3rd order linear temporal model with a more temporal depth and without any spatial dependency. In this case, the Laplace sound speed can be modeled as follow

$$c_L([i, j], t) = \rho_1 c_L([i, j], t - 1) + \rho_2 c_L([i, j], t - 2) + \rho_3 c_L([i, j], t - 3) + u_{c_L}([i, j], t) \quad (4.13)$$

where  $\rho_1$ ,  $\rho_2$ , and  $\rho_3$  are the coefficients of the temporal model for the Laplace sound speed field, and  $u_{c_L}([i, j], t)$  is the deriving noise which represents the inaccuracies in the modeling of the state evolution in time. Similar equations hold for wind velocity amplitude and angle fields,  $\alpha([i, j], t)$  and  $\theta([i, j], t)$ .

The 1-D temporal AR model for the Laplace sound speed can be written in vector form as:

$$\underbrace{\begin{bmatrix} \mathbf{c}_L(t) \\ \mathbf{c}_L(t-1) \\ \mathbf{c}_L(t-2) \end{bmatrix}}_{\mathbf{c}_L^{(a)}(t)} = \underbrace{\begin{bmatrix} \rho_1 \mathbf{I}_{IJ \times IJ} & \rho_2 \mathbf{I}_{IJ \times IJ} & \rho_3 \mathbf{I}_{IJ \times IJ} \\ \mathbf{I}_{IJ \times IJ} & \mathbf{0}_{IJ \times IJ} & \mathbf{0}_{IJ \times IJ} \\ \mathbf{0}_{IJ \times IJ} & \mathbf{I}_{IJ \times IJ} & \mathbf{0}_{IJ \times IJ} \end{bmatrix}}_{A_{temp}^{(c_L)}} \underbrace{\begin{bmatrix} \mathbf{c}_L(t-1) \\ \mathbf{c}_L(t-2) \\ \mathbf{c}_L(t-3) \end{bmatrix}}_{\mathbf{c}_L^{(a)}(t-1)} + \underbrace{\begin{bmatrix} \mathbf{u}_{c_L}(t) \\ \mathbf{0} \\ \mathbf{0} \end{bmatrix}}_{\mathbf{u}_{c_L}^{(a)}(t)}, \quad (4.14)$$

where  $\mathbf{I}_{IJ \times IJ}$  is identity matrix of size  $IJ \times IJ$ , and  $\mathbf{0}_{IJ \times IJ}$ ,  $\mathbf{c}_L(t)$ , and  $\mathbf{u}_{c_L}(t)$  are defined as before. Similar relationship as (4.17) holds for the wind velocity amplitude,  $\alpha(t)$ , and wind velocity angle,  $\theta(t)$ . Thus, we have

$$\alpha^{(a)}(t) = A_{temp}^{(\alpha)} \alpha^{(a)}(t-1) + \mathbf{u}_\alpha^{(a)}(t) \quad (4.15)$$

$$\theta^{(a)}(t) = A_{temp}^{(\theta)} \theta^{(a)}(t-1) + \mathbf{u}_\theta^{(a)}(t), \quad (4.16)$$

where  $\alpha^{(a)}(t) = [\alpha^T(t), \alpha^T(t-1), \alpha^T(t-2)]^T$ , and  $\theta^{(a)}(t) = [\theta^T(t), \theta^T(t-1), \theta^T(t-2)]^T$  are the augmented wind velocity amplitude and wind velocity angle vectors, respectively,  $\alpha^T(t)$ ,  $\theta^T(t)$  are defined as before,  $\mathbf{u}_\alpha^{(a)}(t) = [\mathbf{u}_\alpha^T(t), \mathbf{0}^T, \mathbf{0}^T]^T$  is the augmented wind velocity amplitude driving noise,  $\mathbf{u}_\theta^{(a)}(t) = [\mathbf{u}_\theta^T(t), \mathbf{0}^T, \mathbf{0}^T]^T$  is the augmented wind velocity angle driving noise, and  $\mathbf{u}_\alpha^T(t)$  and  $\mathbf{u}_\theta^T(t)$  are defined as before.

Note that like the spatial case, the 1-D temporal AR models are assumed to be decoupled from each other as the phenomena that generate them are independent. Combining these decoupled equations yields the following linear state equation,

$$\underbrace{\begin{bmatrix} \mathbf{c}_L^{(a)}(t) \\ \alpha^{(a)}(t) \\ \theta^{(a)}(t) \end{bmatrix}}_{\mathbf{x}_t^{(a)}} = \underbrace{\begin{bmatrix} A_{temp}^{(c_L)} & \mathbf{0}_{3IJ \times 3IJ} & \mathbf{0}_{3IJ \times 3IJ} \\ \mathbf{0}_{3IJ \times 3IJ} & A_{temp}^{(\alpha)} & \mathbf{0}_{3IJ \times 3IJ} \\ \mathbf{0}_{3IJ \times 3IJ} & \mathbf{0}_{3IJ \times 3IJ} & A_{temp}^{(\theta)} \end{bmatrix}}_{A_{temp}} \underbrace{\begin{bmatrix} \mathbf{c}_L^{(a)}(t-1) \\ \alpha^{(a)}(t-1) \\ \theta^{(a)}(t-1) \end{bmatrix}}_{\mathbf{x}_{t-1}^{(a)}} + \underbrace{\begin{bmatrix} \mathbf{u}_{c_L}^{(a)}(t) \\ \mathbf{u}_\alpha^{(a)}(t) \\ \mathbf{u}_\theta^{(a)}(t) \end{bmatrix}}_{\mathbf{u}_t^{(a)}}. \quad (4.17)$$

### 4.2.2 Observation Process

For all the three models, the relationship between state  $\mathbf{x}_t$  and observation vector  $\mathbf{y}_t$  at time  $t$  is given by (A.3), and (2.7) which is a nonlinear function of the state variables expressed as

$$\mathbf{y}_t = \mathbf{h}(\mathbf{x}_t) + \mathbf{v}_t, \quad (4.18)$$

where  $\mathbf{v}_t$  stands for measurement noise caused by such things as, (i) errors inherent in the gridding process (ii) error in measuring the TOAs, (iii) sensor location error and (iv) imperfect synchronization across all nodes. This noise is assumed to be a Gaussian random vector with zero mean and known covariance matrix,  $R_v$ . The most dominant source for this error is (i). The nonlinear function  $\mathbf{h}(\mathbf{x}_t)$  is explicitly defined as

$$\mathbf{h}(\mathbf{x}_t) = \begin{bmatrix} \sum_{i=1}^I \sum_{j=1}^J \frac{d_1(i,j)}{c_L([i,j],t) + \mathbf{s}_1 \cdot \mathbf{v}([i,j],t)} \\ \vdots \\ \sum_{i=1}^I \sum_{j=1}^J \frac{d_N(i,j)}{c_L([i,j],t) + \mathbf{s}_N \cdot \mathbf{v}([i,j],t)} \end{bmatrix} \quad (4.19)$$

Assuming that the model parameters are changing temporally, matrices  $\mathbf{A}$  and  $\mathbf{A}_{temp}$  in (4.17) and (4.17) will also change temporally. In what follows, we use the new notation  $\mathbf{A}(\boldsymbol{\rho}_t)$  and  $\mathbf{A}_{temp}(\boldsymbol{\rho}_t)$  to show that  $\mathbf{A}$  and  $\mathbf{A}_{temp}$  are functions of  $\boldsymbol{\rho}_t$  where  $\boldsymbol{\rho}_t$  is the model parameter vector.

Assuming that  $\boldsymbol{\rho}_t$  is time invariant and can be estimated using either a training data set or arrived at from a covariance structure, the state vector can be estimated using the state estimation UKF method in Section 3.4. However, if the parameters are assumed to be unknown and time varying then the problem becomes a dual state-parameter estimation problem which can be solved using the dual UKF discussed in Section 3.5. The dual UKF For the dual UKF using the first order 3-D AR model for

state evolution we have,

$$\text{State filter: } \begin{cases} \mathbf{x}_t = A(\hat{\boldsymbol{\rho}}_{t-1|t-1})\mathbf{x}_{t-1} + \mathbf{u}_t \\ \mathbf{y}_t = \mathbf{h}(\mathbf{x}_t) + \mathbf{v}_t \end{cases} \quad (4.20)$$

$$\text{Parameter filter: } \begin{cases} \boldsymbol{\rho}_t = \boldsymbol{\rho}_{t-1} + \mathbf{n}_t \\ \mathbf{y}_t = \mathbf{h}(A(\boldsymbol{\rho}_t)\hat{\mathbf{x}}_{t-1|t-1}) + \mathbf{v}_t \end{cases}, \quad (4.21)$$

Therefore, having the TOAs as observation and choosing the suitable state evolution model, one can formulate the problem as a state-space problem and reconstruct the temperature and wind velocity fields using dual UKF.

### 4.3 Conclusion

A new statistical-based acoustic tomography algorithm was proposed in this chapter. The proposed method is based on casting the problem as a state-space problem and solving the non-linear state estimation using UKF. In order to capture the state dynamics, three different linear models were suggested and formulated.

The state evolution model plays a critical role in the performance of the proposed method as it decides the accuracy of the state estimation as well as the convergence properties [39]. Assuming that the state evolution model is time-varying, one needs to estimate the model parameters as well as the states at every snapshot and therefore use either the dual UKF or the joint UKF estimators. On the other hand, if the model parameters are known or can be estimated by any means, the original UKF state estimator would be adequate. In the subsequent chapters we used dual UKF on both synthesized and real data sets.

# CHAPTER 5

## DATA GENERATION USING FRACTAL BROWNIAN MOTION

### 5.1 Introduction

In order to test our proposed UKF-based algorithm a data set was acquired from the university of Leipzig, collected at the Meteorological Observatory, Lindenberg, Germany, within the project STINHO [27]. The data set consists of the TOAs for a field of size  $300m \times 440m$  with 8 transmitters and 12 receivers (96 paths and TOA measurements). The detailed explanation of these experiments can be found in [27]. However, the lack of sufficient in situ measurements (only 2 temperature sensors) for a complete evaluation of the developed algorithm motivated us to construct a synthetic but close to realistic data set, using the same setup as in STINHO.

The synthetic data was generated based on fractal Brownian motion (fBm) model [49] for wind velocity and temperature fields in the investigation area. There are several mathematical models which can be employed to describe the wind power spectrum [50–53]. However, fBm, also known as  $1/f$  noise [54], is one of such models. In this thesis, we have used an extended 2-D fBm-based method inspired from that in [49] to generate 2-D wind velocity and temperature fields. The following subsections describe the process of the synthetic data generation. The 1-D fBm is first reviewed and its extension to 2-D is presented. The Fourier-based filtering method is utilized to generate the 2-D extension of fBM, and finally the properties of the generated synthetic data are explained.

## 5.2 Fractal Brownian Motion

In 1827 R. Brown [55] observed that small particles of a solid matter move in an erratic and irregular manner in a liquid medium. The modeling of this motion is an important topic in statistical mechanics [56] which led to the concept of Brownian motion. Brownian motion itself is a member of a bigger family called fractal Brownian motion. Fractals are self-similar patterns which are observed in many natural phenomena, such as clouds, rivers, and atmospheric patterns. Fractal Brownian motion is a branch of statistics which studies the behavior of the self similar continuous time Gaussian processes.

A Gaussian process  $X^H = \{X^H(t), t \geq 0\}$  is called a fractal Brownian motion (fBm) of Hurst parameter  $H \in (0, 1)$  [57, 58] if its mean is zero and its covariance matrix is defined as,

$$E[X^H(t_1)X^H(t_2)] = \frac{1}{2}(t_1^{2H} + t_2^{2H} - |t_1 - t_2|^{2H}). \quad (5.1)$$

The fBm  $X^H$  has interesting characteristics, such as self similarity [57, 58] which states that

$$\{X^H(t), t \geq 0\} \quad \text{and} \quad \left\{\frac{1}{a^H}X^H(at), t \geq 0\right\}, \quad (5.2)$$

have the same probability distribution for any  $a > 0$ . The self similarity property of  $X^H$ , can be considered as a fractal property [59], hence  $X^H$  is called fractal Brownian motion.

The second interesting characteristics of  $X^H$  is having stationary increments, meaning that the increment of the process from  $t_1$  to  $t_2$  has a normal distribution with mean zero and variance,

$$E[(X^H(t_1) - X^H(t_2))^2] = |t_1 - t_2|^{2H} \quad (5.3)$$

which follows immediately from (5.1), by expanding  $(X^H(t_1) - X^H(t_2))^2$ .

The fBm is classified [57, 58] into three classes for different values of the Hurst parameter.

1.  $H = \frac{1}{2}$  : which is called ordinary Brownian motion, in which the covariance can be written as

$$\begin{aligned} E[X^{0.5}(t_1)X^{0.5}(t_2)] &= \frac{1}{2}(t_1 + t_2 - |t_1 - t_2|) \\ &= \min(t_1, t_2). \end{aligned} \quad (5.4)$$

Following (5.1) it can be shown that the increments of the process in disjoint intervals are independent, meaning that for  $t_1 < t_2 < t_3$  we have

$$E[(X^{0.5}(t_2) - X^{0.5}(t_1))(X^{0.5}(t_3) - X^{0.5}(t_2))] = 0. \quad (5.5)$$

2.  $H > \frac{1}{2}$  : indicates that there is a positive correlation between these increments, i.e.

$$E[(X^H(t_2) - X^H(t_1))(X^H(t_3) - X^H(t_2))] > 0 \quad (5.6)$$

3.  $H < \frac{1}{2}$  : indicates that there is a negative correlation between these increments.

$$E[(X^H(t_2) - X^H(t_1))(X^H(t_3) - X^H(t_2))] < 0 \quad (5.7)$$

It is straightforward to show [60] that the spectral density for such random variable has the following characteristic

$$S(f) \propto \frac{1}{f^\beta} \sim \text{fBm} \quad (5.8)$$

where  $\beta = 2H + 1$ . The spectral density function in (5.8) can be extended to higher dimensions in order to obtain higher dimensional fBm. The spectral density function for an n-dimensional fBm is defined as,

$$S(f_1, f_2, \dots, f_n) \propto \frac{1}{(\sum_{i=1}^n f_i)^{\beta+n-1}} \quad (5.9)$$

The spectral density can be used to generate realization of fBm. In order to do so one can use Fourier-based filtering [59], discussed in the following section.

### 5.2.1 Fourier-Based Filtering Method

Given the spectral density of a random process, Fourier-based filtering method enables one to generate realizations of the random process. In this section, we are going to first study the method for the simple case of 1-D fBm, and then we extend the definition to the 2-D case.

To begin the process the Fourier-based filtering method assumes that a sample of  $N$  realizations of a 1-D fBm,  $\{x^H(t), t = 0, \dots, N - 1\}$ , is given. Based on these realizations the periodogram [61] of  $x^H$  is calculated as,

$$\begin{aligned} Per(k) &= \frac{1}{N} \left| \sum_{t=0}^{N-1} x^H(t) e^{-j \frac{2\pi kt}{N}} \right|^2 \quad \text{for } k = 0, \dots, N - 1 \\ &= \frac{1}{N} |X_F^H(k)|^2 \end{aligned} \quad (5.10)$$

where  $X_F^H(k)$  is the discrete Fourier transform of  $\{x^H(t), t = 0, \dots, N - 1\}$ , i.e.,

$$X_F^H(k) = \sum_{t=0}^{N-1} x^H(t) e^{-j \frac{2\pi kt}{N}} \quad \text{for } k = 0, \dots, N - 1, \quad (5.11)$$

Substituting (5.11) in (5.10) and using the fact that periodogram is an estimate of the spectral density we can write,

$$\frac{1}{N} (|X_F^H(k)|^2) = \frac{1}{N} (Re^2(X_F^H(k)) + Im^2(X_F^H(k))) = S(k). \quad (5.12)$$

Note that, the process started with the assumption of having a sample of  $N$  point realizations of  $X^H$ . The Fourier filtering method then states that, if we randomly generate an  $N$ -point discrete signal in Fourier domain that follows (5.12), then the time domain representation of that signal will be an  $N$  point realization of  $X^H$ .

To do so, the Fourier-based filtering method assumes that  $Re(X_F^H(k))$  and  $Im(X_F^H(k))$  in (5.12) are independent random variables with the same normal distributions,  $\mathcal{N}(0, \frac{N}{2}S(k))$ . The distributions are chosen in a way that the expected value of (5.12) follows, i.e.  $E[\frac{1}{N}(Re^2(X_F^H(k)) + Im^2(X_F^H(k)))] = S(k)$ .

Note that for the realizations,  $x^H(t)$ , to be real,  $X_F^H(k)$ s must satisfy  $(X_F^H(k))^* = X_F^H(N-k)$  for  $k = 1, \dots, \frac{N}{2}$ . The Fourier-based filtering method then draws  $Re(X_F^H(k))$  and  $Im(X_F^H(k))$  for  $k = 1, \dots, \frac{N}{2}$  randomly from their distribution and forms  $X_F^H(k)$ s (If  $N$  happens to be an odd number, then the first  $\frac{N+1}{2}$  samples are drawn).

Finally, having the coefficients of the DFT, Fourier-based filtering method generates  $x^H(t)$  using the inverse DFT (IDFT) as follow,

$$x^H(t) = \frac{1}{N} \sum_{k=0}^{N-1} X_F^H(k) e^{j \frac{2\pi t k}{N}}, \quad \text{for } t = 0, \dots, N-1. \quad (5.13)$$

Therefore, this method enables one to generate realizations of a random variable,  $X^H(t)$ , given its spectral density,  $S(f)$ . Figure 5.1 shows the process of generating an  $N$ -point realization of a random variable from its spectral density using the Fourier-based filtering method.

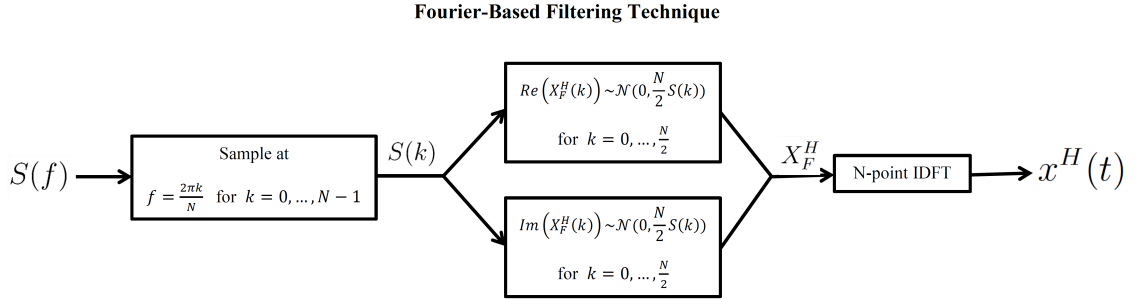


**Figure 5.1:** Schematic diagram of the Fourier-based filtering method.

Fourier-based filtering method can be extended to higher dimensions [59]. For instance for a  $N \times M$  realization of a 2-D fBm process,  $\{x^H(i, j), i = 0, \dots, N-1 \text{ and } j = 0, \dots, M-1\}$ , we can write the periodogram as,

$$\begin{aligned} Per(k, l) &= \frac{1}{MN} \left| \sum_{i=0}^{N-1} \sum_{j=0}^{M-1} x^H(i, j) e^{-j2\pi(\frac{ki}{N} + \frac{lj}{M})} \right|^2 \\ &= \frac{1}{MN} |X_F^H(k, l)|^2, \end{aligned} \quad (5.14)$$

where  $X_F^H(k, l)$  is the 2-D DFT of  $x^H$ , i.e.,

$$X_F^H(k, l) = \sum_{i=0}^{N-1} \sum_{j=0}^{M-1} x^H(i, j) e^{-j2\pi(\frac{ki}{N} + \frac{lj}{M})}. \quad (5.15)$$

Substituting (5.15) in (5.14) and using the fact that the periodogram is an estimate of the spectral density we can write,

$$\frac{1}{NM} (|X_F^H(k, l)|^2) = \frac{1}{NM} (Re^2(X_F^H(k, l)) + Im^2(X_F^H(k, l))) = S(k, l). \quad (5.16)$$

Similar to the 1-D fBm process, the 2-D Fourier-based filtering method assumes that  $Re(X_F^H(k, l))$  and  $Im(X_F^H(k, l))$  are independent random variables with normal distribution,  $\mathcal{N}(0, \frac{NM}{2}S(k, l))$ , and therefore the expected value of (5.16) can be written as,

$$E[\frac{1}{NM} (Re^2(X_F^H(k, l)) + Im^2(X_F^H(k, l)))] = S(k, l). \quad (5.17)$$

Note that for the realizations,  $x^H(i, j)$ , to be real,  $X_F^H(k, l)$ s must satisfy the conditions below,

$$\begin{aligned} (X_F^H(k, l))^* &= X_F^H(N - k, M - l) \\ (X_F^H(0, l))^* &= X_F^H(0, M - l) \\ (X_F^H(k, 0))^* &= X_F^H(N - k, 0). \end{aligned} \quad (5.18)$$

Finally, the Fourier-based filtering method draws  $Re(X_F^H(k, l))$  and  $Im(X_F^H(k, l))$  for  $k = 0, \dots, \frac{N}{2}$  and  $l = 0, \dots, \frac{M}{2}$ , randomly from their distributions and forms  $X_F^H(k, l)$ s.

Having the coefficients of the 2-D DFT, Fourier-based filtering method then generates  $\{x^H(i, j), i = 0, \dots, N - 1 \text{ and } j = 0, \dots, M - 1\}$  using the 2-D inverse DFT (IDFT) as follow,

$$x^H(i, j) = \frac{1}{NM} \sum_{k=0}^{N-1} \sum_{l=0}^{M-1} X_F^H(k, l) e^{j2\pi(\frac{tk}{N} + \frac{tl}{M})}. \quad (5.19)$$

### 5.3 Synthetic Data Generation

Based on the fBm, the method in [49] suggests the wind velocity 2-D power spectral density function as

$$S(f_1, f_2) = \frac{\vartheta}{(f_1^2 + f_2^2)^{\beta+1}}, \quad (5.20)$$

where  $f_1$  and  $f_2$  are the 2-D spatial frequencies in Hz,  $\beta = 1.66$  for wind field simulations (though it can be changed to obtain wind and temperature fields with different characteristics), and  $\vartheta$  is a constant which depends on the height of the simulated field from the ground and the type of the terrain.

The fields  $\mathbf{c}_L(\mathbf{r}, t_0), \alpha(\mathbf{r}, t_0)$  and  $\theta(\mathbf{r}, t_0)$  are then generated from (5.20) using the Fourier-based filtering algorithm reviewed in Section 5.2, for an area 10 times bigger than the investigation area at initial time  $t_0$ . The investigation area is chosen to lay on the center of this larger area.

Figure 5.2 show the virtual layout of investigation field and the locations of the receivers and transmitters indicated by  $R_i$  and  $S_i$ , respectively.

The synthetic data is generated for 500 subsequent snapshots of wind velocity and temperature fields with spatial resolution of one meter and temporal resolution of 12 seconds, for both cases. The TOAs for each sound ray path is then calculated using (3.12) at each snapshot. The measurement noise vector  $\mathbf{v}_t$  is assumed to be a zero mean white Gaussian process with covariance matrix  $\mathbf{R}_v = \sigma_v^2 \mathbf{I}$  and  $\sigma^2 = 0.01$ .

Given these fields at initial time  $t_0$  the wind velocity and temperature fields are calculated in the investigation area at time  $t$  assuming the frozen turbulence assumption at increments of  $\Delta t = 12sec$  using

$$\mathbf{v}(\mathbf{r}, t) = \mathbf{v}(\mathbf{r} - \bar{\mathbf{v}}(t-1)\Delta t, t-1) \quad (5.21)$$

$$\mathbf{c}_L(\mathbf{r}, t) = \mathbf{c}_L(\mathbf{r} - \bar{\mathbf{v}}(t-1)\Delta t, t-1) \quad (5.22)$$

where  $\bar{\mathbf{v}}(t)$  is the spatial mean wind velocity vector at time  $t$ . Figure 5.3 shows the

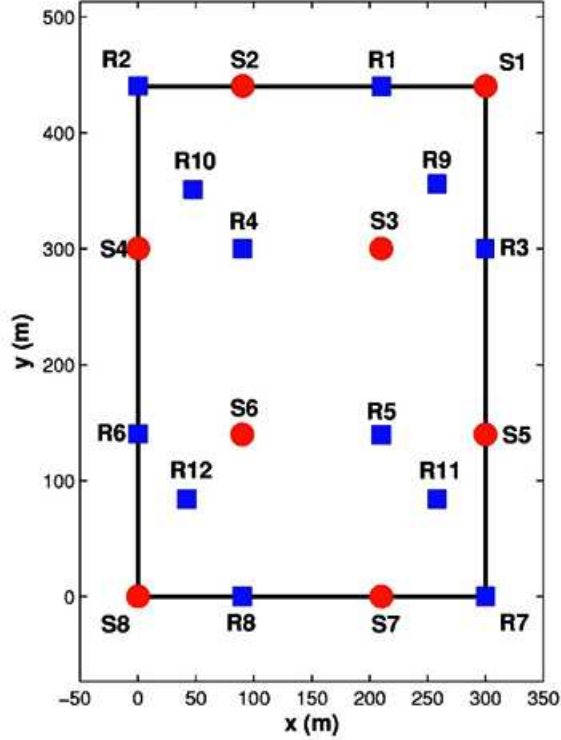


**Figure 5.2:** The out layer of the STINHO field experiment

larger size field and the process of generating the synthetic data in time. Note that the frozen turbulence hypothesis includes two assumptions about the temporal evolution of the atmosphere. First, the layers of the fields are spatially stable through time. Second, these layers are moving with the spatial mean wind velocity.

Figure 5.4 shows the synthetically generated wind velocity and temperature fields for two sample snapshots ( $t = 75, t = 100$ ) over the investigation area for the synthetic data set. It can be seen from Figure 5.4 that fBm model generates near realistic temperature and wind velocity fields. Having the fields  $\mathbf{c}_L(\mathbf{r}, t), \alpha(\mathbf{r}, t)$  and  $\theta(\mathbf{r}, t)$  for  $t = 1, \dots, 500$ , the TOAs are calculated using (A.2) for all the paths. A zero mean white Gaussian noise with variance  $\sigma_v^2 = 0.01$  is added to each calculated TOA, in order to simulate the measurement noise in the synthesized TOA measurements. This variance is chosen based upon the uncertainty measurements reported in [27] which is 0.3 milisecond for each measurement. These noisy measurements are then

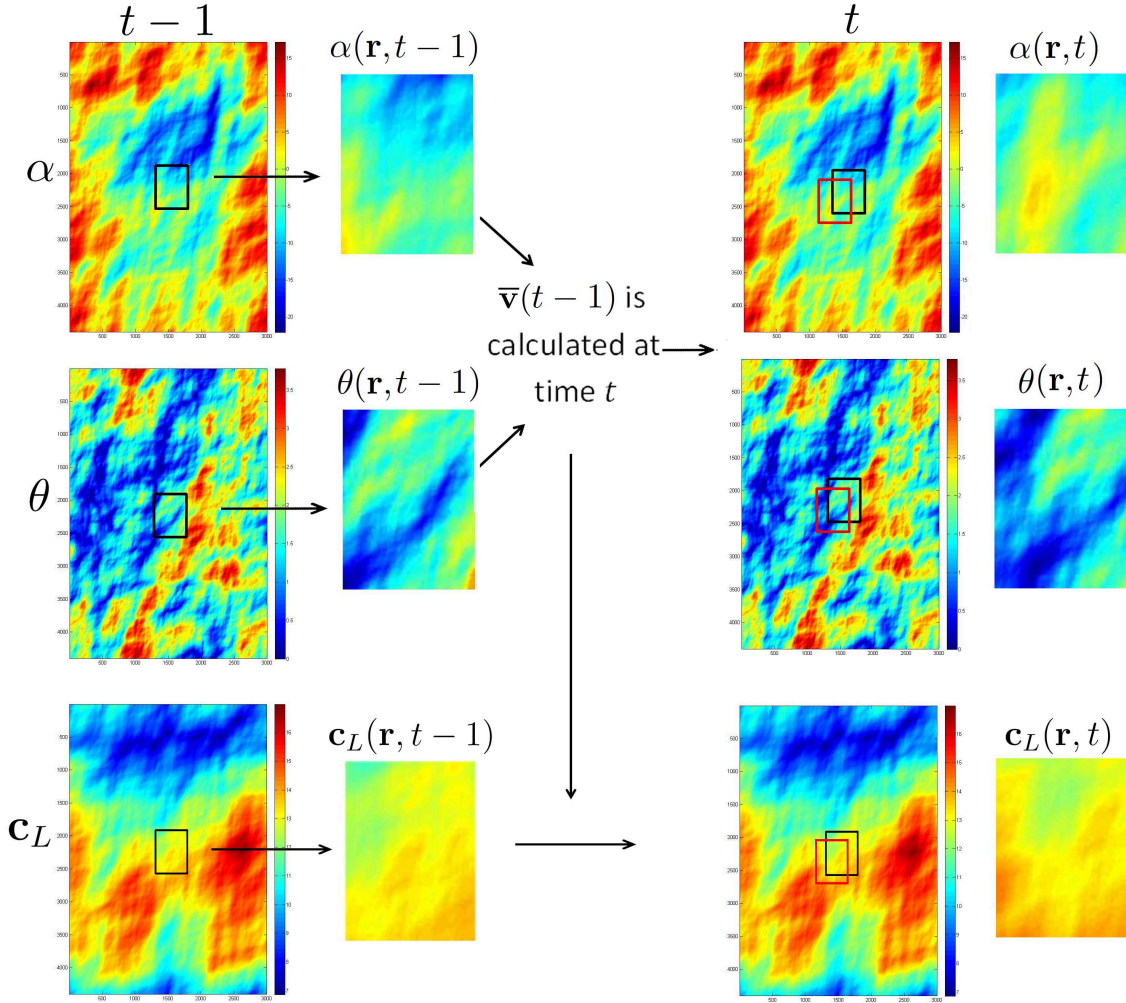


**Figure 5.3:** The oversized  $c_L$ ,  $\alpha$ , and  $\theta$  fields and the process of generating the data sequence in time

applied to the UKF-based acoustic tomography algorithm, discussed in Chapter 4, to reconstruct the temperature and wind velocity fields.

## 5.4 Conclusion

This chapter reviewed the process of generating the synthetic temperature and wind velocity data sets. The fractal Brownian motion (fBm) was explained and used as the model to generate random wind velocity and temperature fields. The reason behind using fBm, is that the atmospheric patterns have identical fractal properties as fBms [62]. The Fourier-based filtering method was reviewed in depth in order to

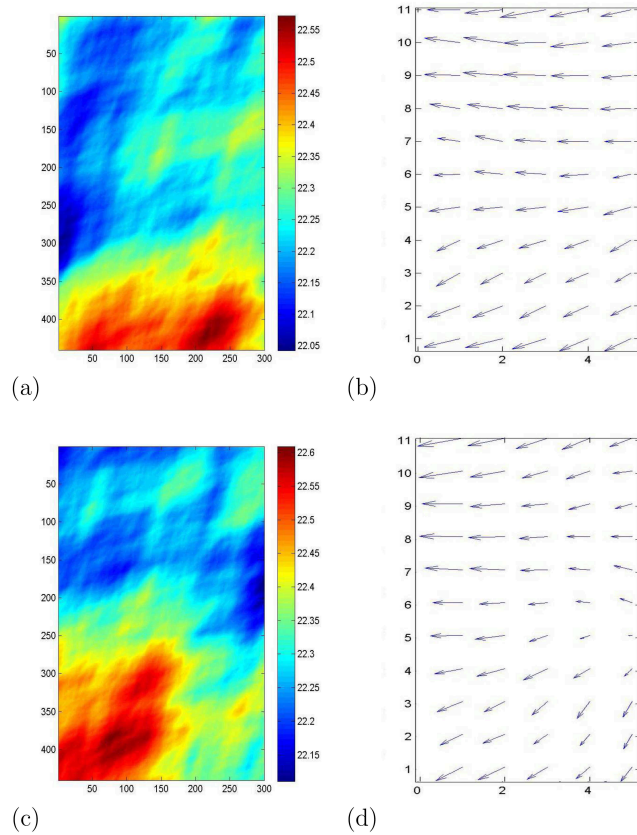


**Figure 5.4:** (a) The synthetic temperature field at snapshot number  $t = 75$  (b) The synthetic wind velocity field at snapshot number  $t = 75$  (c) The synthetic temperature field at snapshot number  $t = 100$  (d) The synthetic wind velocity field at snapshot number  $t = 100$ .

generate realizations of 1-D and 2-D fBm for different sizes.

Utilizing the frozen turbulence assumption, a data set was generated based on fBm with spatial resolution of  $1m$  and temporal resolution of  $12sec$  for 500 snapshots. The temperature and wind velocity synthetic fields are then used to calculate the TOAs for all the paths. Furthermore, an additive zero mean Gaussian process is employed to simulate the effect of the measurement noise.

In this thesis we focused on the 2-D characteristics of the atmospheric surface layer, however the same process can be used to generate a 3-D data set in order to study the performance of the tomography methods for 3-D temperature and wind velocity reconstruction.

# CHAPTER 6

## RESULTS ON SYNTHESIZED AND REAL DATA SETS

### 6.1 Introduction

In this chapter, the developed UKF-based acoustic tomography is applied to the synthetic and real data sets to reconstruct the temperature and wind velocity fields. The synthesized data set was generated using fBm method described in Chapter 5. The real data set was collected at the Meteorological Observatory, Lindenberg, Germany, within the project STINHO. The real STINHO data set has TOA measurements for 79 paths (out of total 96 paths, meaning that the measurements for 17 paths are missing) and for 1038 snapshots (0:00 - 17:17 UTC, every minute). The detailed description of the real data set can be found in [27].

Two different experiments are conducted to evaluate the performance of the UKF-based acoustic tomography method. In the first experiment, UKF-based acoustic tomography was applied to the synthetic data set using three different state evolution models, namely random walk, first order 3-D AR model, and temporal AR model and their performance was tested against that of the TDSI method.

The second experiment is conducted on the real data set. Dealing with the real data set, one doesn't have the luxury of having a training data set to estimate the driving noise covariance matrix or the model parameters. Therefore, we have employed the UKF-based dual estimation method reviewed in Chapter 4 to estimate the states and the model parameters simultaneously. Having a good estimation of the model parameters one could expect the covariance matrix,  $R_u$  to have a similar

pattern as in the first experiment, hence, we have used the same estimated  $R_u$  in the first experiment as the driving noise covariance matrix for the second experiment.

This chapter describes the experiments conducted on the synthetic and the real data sets and compares the reconstruction accuracy and computational complexity of the proposed method using different state evolution models and the TDSI method.

## 6.2 Results on Synthesized Data Set

A  $4 \times 8$  grid is overlaid on the investigation area of size  $300m \times 440m$  to partition it into 32 grids of dimensions  $75m \times 55m$ . The problem was formulated as in Chapter 4, for three different state evolution models and the first 5 snapshots were used to estimate the covariance matrix of the driving noise,  $R_u$ , as well as the state evolution model parameters (See Section 4.2). One could argue that using the actual fields to estimate the statistics of the driving noise is not realistic, however, our goal in the first experiment was to investigate the performance of the UKF state estimator for different state evolution models given a rough estimate of the driving noise (using only 1% of the data). The TDSI method was also implemented and applied to the synthetic data set as part of the first experiment to compare its performance against that of UKF-based method. Similarly, the first 5 snapshots were used to estimate the spatial covariance functions for temperature and wind velocity. The results of the UKF-based method for the three state evolution model are first compared in terms of reconstruction accuracy, tracking ability, and computational speed. Then, the best of the three is compared against the TDSI method.

For both algorithms, the mean fields at each snapshot are first calculated using the method described in Chapter 3. Figure 6.1 shows the plots of the actual and calculated mean fields at all snapshots for the temperature, wind velocity amplitude, and wind velocity angle. The red curve is the actual mean field calculated from the synthetic data over 500 snapshots and the green curve is the reconstructed mean field.

As can be seen, these results illustrate the accuracy of mean field estimation process in [7, 11].

The mean fields are used as the initial starting point  $\hat{\mathbf{x}}_{0|0}$  in the UKF-based acoustic tomography and are also used in TDSI formulation at every snapshot.

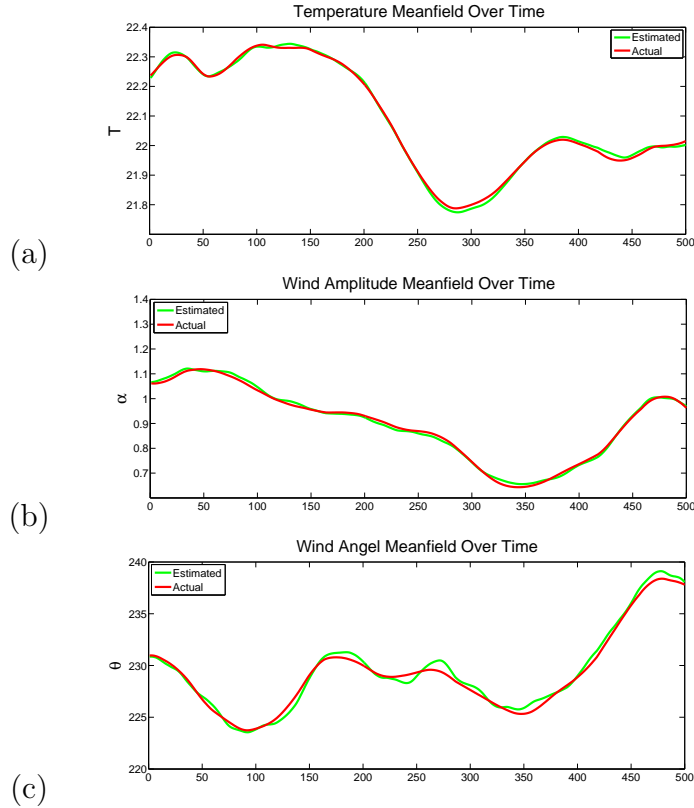


**Figure 6.1:** Actual and estimated mean fields (a) temperature, (b) wind velocity amplitude, and (c) wind velocity angle, over all snapshots.

### 6.2.1 TDSI-Based Acoustic Tomography

TDSI implementation involves finding the parameters of the spatial covariance functions of the Laplace sound speed and wind velocity and estimating the mean fields at every snapshot as explained before. Additionally, using this method assumes that (a) the temperature and wind velocity fields are stationary, (b) the fields follow the frozen turbulence assumption, (c) the projection of the wind velocity on every path is small in comparison to the Laplace sound speed, and (d) the temperature fluctuations

are smaller than the mean temperature.

Assuming Gaussian functions for the spatial covariance functions of the Laplace sound speed and wind velocity fields, the first 5 snapshots of the synthesized data were used as the training data to estimate the parameters of these functions, namely  $\sigma_{c_L}$ ,  $\sigma_{v_x}$ ,  $\sigma_{v_y}$ ,  $l_{c_L}$ , and  $l$  in (2.43)-(2.46), using the least square (LS) method.

Our experiments showed that for the synthetic data set using  $M = 4$  previous snapshots is an optimal choice as far as reconstruction accuracy and speed are concerned. Therefore, we used  $M = 4$  previous snapshots to generate the augmented observation vector  $\mathbf{q}_a(t) = [\mathbf{q}^T(t-4), \mathbf{q}^T(t-3), \mathbf{q}^T(t-2), \mathbf{q}^T(t-1), \mathbf{q}^T(t)]^T$  to reconstruct the fluctuation fields at time  $t$ . The spatial-temporal covariance functions are then constructed based on the frozen turbulence assumption and the estimated spatial covariance functions from equation (2.42). Thus, for the spatial-temporal covariance of the Laplace sound speed we have,

$$B_{c_L c_L}(\mathbf{r}_l, t_l, \mathbf{r}_k, t_k) = B_{c_L c_L}^s(\mathbf{r}_l, \mathbf{r}_k - \bar{\mathbf{v}}(t_l)(t_k - t_l)), \quad (6.1)$$

where  $B_{c_L c_L}(\mathbf{r}_l, t_l, \mathbf{r}_k, t_k)$  is the spatial-temporal covariance of the Laplace sound speed field at location  $\mathbf{r}_l$  and at time  $t_l$  and the Laplace sound speed at location  $\mathbf{r}_k$  and at time  $t_k$ ,  $\bar{\mathbf{v}}(t_l)$  is the spatial mean wind velocity vector at time  $t_l$ . The spatial-temporal covariances for wind velocity amplitude  $B_{\alpha\alpha}$  and wind velocity angle  $B_{\theta\theta}$  are obtained similarly.

Having estimated spatial-temporal covariance matrices, matrices  $C_{mq_a}$  and  $C_{q_a q_a}$  are reconstructed at each snapshot according to (2.38) and (2.39) in Chapter 3. The fields are then reconstructed using (2.32).

## 6.2.2 UKF-Based Acoustic Tomography

### (a) Model Evaluation

In this section three different state evolution models are utilized to reconstruct the temperature and wind velocity fields. The state evolution model parameters are

assumed to be temporally fixed, and are estimated using the first 5 snapshots of the synthesized data.

The first model used to capture the state evolution dynamics is the random walk model, given in (4.3) in Chapter 4. It is assumed that  $\mathbf{v}_t$  and  $\mathbf{u}_t$  are mutually uncorrelated, zero mean Gaussian processes with covariance matrices  $R_v = \sigma_v^2 I$  and  $R_u$ . The latter can be estimated from the training data as follow,

$$R_u = \frac{1}{N_t} \sum_{t=2}^{N_t} (\mathbf{x}_t - \mathbf{x}_{t-1})(\mathbf{x}_t - \mathbf{x}_{t-1})^T \quad (6.2)$$

where  $N_t = 5$  is the size of the training set.

Having estimated  $R_u$  and  $R_v$ , the mean fields calculated for the first snapshot are used as the initial state,  $\hat{\mathbf{x}}_{0|0} = [\bar{\mathbf{c}}_L^T(t_0), \bar{\boldsymbol{\alpha}}^T(t_0), \bar{\boldsymbol{\theta}}^T(t_0)]^T$ , and further  $P_{0|0} = \mathbf{I}$ . Then, the temperature, wind velocity amplitude and angle fields are reconstructed using steps 1-5 of the fixed-point iterative UKF in Section 3.6 for  $K = 5$  number of fixed-point iterations.

The next model used to capture the state evolution dynamics was the first order 3-D AR model described in (4.10) in Chapter 4. It is assumed that the parameter vector  $\boldsymbol{\rho}$  is time-invariant and can be estimated based on the training data using Yule-Walker method [48]. Using Yule-Walker method, the first order 3-D AR coefficients are estimated to be  $\rho_0^{(c_L)} = 0.985$ ,  $\rho_1^{(c_L)} = 0.090$ ,  $\rho_2^{(c_L)} = -0.046$ ,  $\rho_0^{(\alpha)} = 0.998$ ,  $\rho_1^{(\alpha)} = -0.0086$ ,  $\rho_2^{(\alpha)} = 0.0091$ ,  $\rho_0^{(\theta)} = 0.999$ ,  $\rho_1^{(\theta)} = -0.001$  and  $\rho_2^{(\theta)} = 0.001$ . From the estimated parameters it can be seen that in the wind velocity angle the first order 3-D AR is very close to the random walk model. Hence, in the following experiments we set  $\rho_0^{(\theta)} = 1$ ,  $\rho_1^{(\theta)} = 0$ , and  $\rho_2^{(\theta)} = 0$ , which means that we are employing random walk model for the wind velocity angle instead of the 3-D AR model.

Given the estimate of the parameter vector,  $R_u$  is estimated from the training data using,

$$R_u = \frac{1}{N_t} \sum_{t=2}^{N_t} (\mathbf{x}_t - A(\boldsymbol{\rho})\mathbf{x}_{t-1})(\mathbf{x}_t - A(\boldsymbol{\rho})\mathbf{x}_{t-1})^T \quad (6.3)$$

As mentioned before the mean fields are used for the initial state,  $\hat{\mathbf{x}}_{0|0} = [\bar{\mathbf{c}}_L^T(t_0), \bar{\boldsymbol{\alpha}}^T(t_0), \bar{\boldsymbol{\theta}}^T(t_0)]^T$ , and  $P_{0|0} = \mathbf{I}$ . All other conditions are the same as those in the previous case.

Finally, the last model considered here is the 3rd order temporal AR model described in (4.17) in Chapter 4. Using the Yule Walker method the temporal AR coefficients are estimated to be  $\rho_0^{cL} = 2.890$ ,  $\rho_1^{cL} = -2.810$ ,  $\rho_2^{cL} = 0.920$ ,  $\rho_0^\alpha = 2.888$ ,  $\rho_1^\alpha = -2.801$ ,  $\rho_2^\alpha = 0.913$ ,  $\rho_0^\theta = 2.892$ ,  $\rho_1^{cL} = -2.813$ , and  $\rho_2^{cL} = 0.921$ .

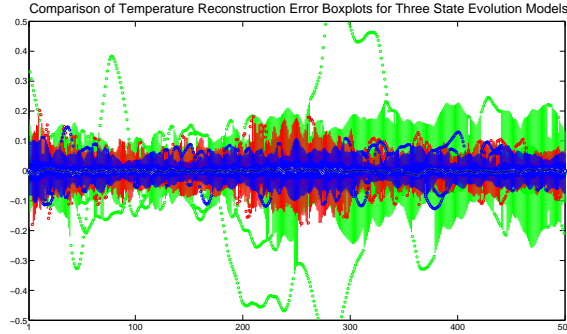
The sample correlation matrix,  $\mathbf{R}_u$  is estimated from the training data using

$$\mathbf{R}_u = \frac{1}{N_t} \sum_{t=2}^{N_t} (\mathbf{x}_t^{(a)} - A_{temp}(\boldsymbol{\rho})\mathbf{x}_{t-1}^{(a)})(\mathbf{x}_t^{(a)} - A_{temp}(\boldsymbol{\rho})\mathbf{x}_{t-1}^{(a)})^T. \quad (6.4)$$

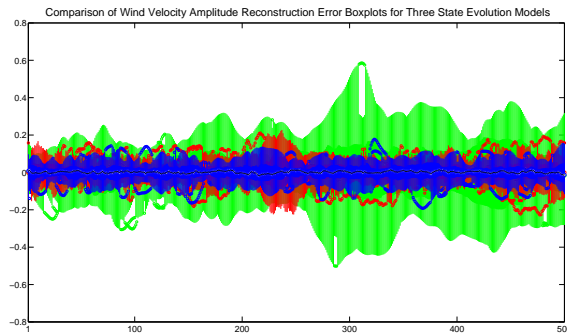
The temperature, wind velocity amplitude and angle fields are then reconstructed using these models.

In order to compare the overall reconstruction accuracy of these models, the reconstruction errors (the difference between actual fields averaged at the grids and the reconstructions) for each field are computed at every snapshot and presented in the boxplots shown in Figure 6.2 for temperature, wind velocity amplitude, and wind velocity angle fields, respectively for all the snapshots. The reconstruction errors for UKF-based acoustic tomography using the random walk model is plotted in green, for the first order 3-D AR model is plotted in blue, and for the temporal model is plotted in red. Each boxplot consists of 500 boxes (1 box per snapshot), and every box demonstrates the variations of reconstruction errors at a single snapshot. The central mark is the median, the edges of the box plot are 25'th and 75'th percentiles, and the whiskers extend to the most extreme points, not considered outliers. The outliers are plotted individually as small circles. The results in Figure 6.2 show that UKF-based acoustic tomography using first order 3-D AR model outperforms the random walk and 3rd order temporal AR models in reconstruction accuracy. However, the reconstruction accuracy of the temporal AR model and the first order 3-D spatial-temporal AR model for wind velocity elements are close to each other, while

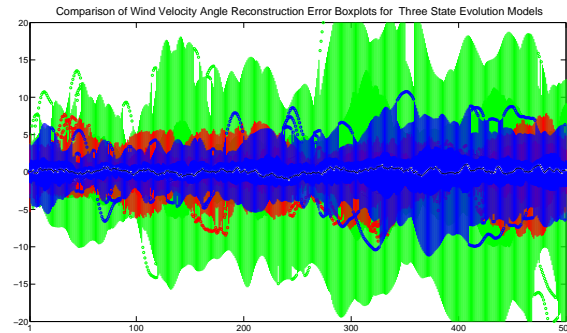
the first order 3-D AR model is slightly better.



(a)



(b)



(c)

**Figure 6.2:** Comparison of field reconstruction errors of UKF-based acoustic tomography using random walk, first order 3-D AR model, and temporal AR in (a) Temperature (b) Wind velocity amplitude (c) Wind velocity angle reconstruction over all snapshots.

The MSE of the field reconstructions for the state evolution models are plotted in Figure 6.3 for all the snapshots. The MSE plots also confirm our previous statement about the temporal AR and the first order 3-D AR models reconstruction accuracy.

The computational complexity of the UKF-based acoustic tomography method

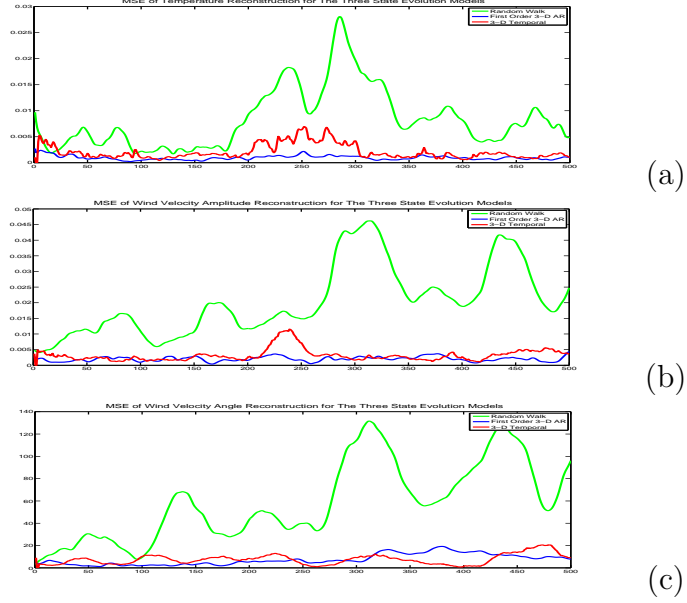


**Figure 6.3:** Comparison of field reconstruction MSEs of UKF-based acoustic tomography using random walk, first order 3-D AR model, and temporal AR in (a) Temperature (b) Wind velocity amplitude (c) Wind velocity angle reconstruction over all snapshots.

is  $O(L^3)$  with  $L$  being the dimension of the state space. Since the size of the state space is the same for the UKF-based acoustic tomography using the random walk and the first order 3-D AR models, therefore, the computational complexity for these state evolution models are about the same. However, for the UKF-based acoustic tomography using the 3rd order temporal AR, due to using augmented state space, the size of the state vector is  $3L$ , and hence the UKF-based acoustic tomography using this model is slower than the those of the first two.

Comparing the reconstruction accuracy and the computational complexity of every model, it can be seen that the first order 3-D AR model outperforms the random walk and the temporal AR models. Hence, the first order 3-D AR model is chosen as the best of the three models and is subsequently compared against the TDSI method.

(b) Comparison with TDSI method

In order to compare the overall reconstruction accuracy of the UKF-based acoustic tomography using the first order 3-D AR model and the TDSI method, the temperature and wind velocity fields are reconstructed using both methods and the boxplot of the variations of reconstruction errors for all grids and for all snapshots are plotted in Figure 6.4.

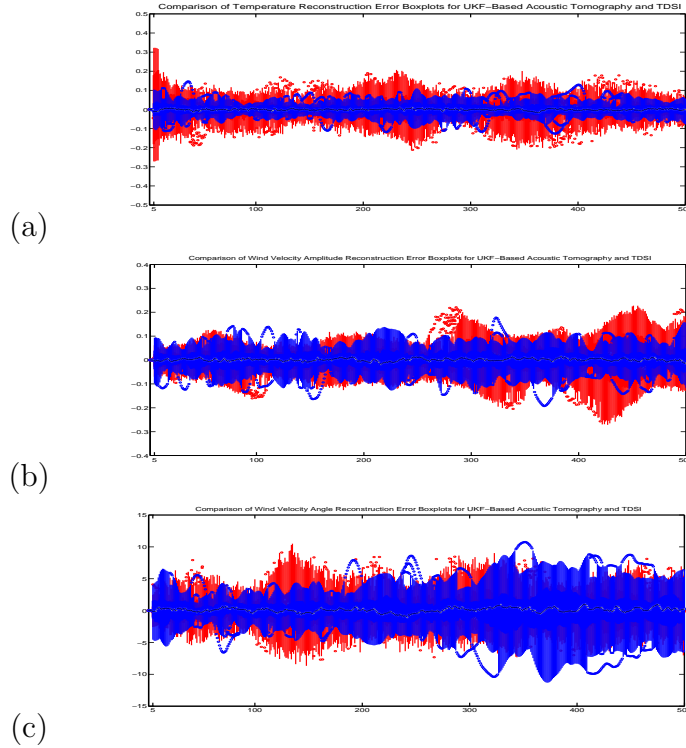


**Figure 6.4:** Comparison of field reconstruction errors of UKF-based acoustic tomography using the first order 3-D AR model and the TDSI method in (a) Temperature (b) Wind velocity amplitude (c) Wind velocity angle reconstruction over all snapshots.

As can be seen from these boxplots the UKF-based acoustic tomography using first order 3-D AR model outperforms the TDSI method in reconstruction accuracy of temperature and wind velocity amplitude fields. However, the performance is very close for the wind velocity angle reconstruction. In addition, the MSE of the field reconstructions for these two methods are plotted in Figure 6.5 for all snapshots, which also attest to the same observation.

Figures 6.6-6.9 illustrate the results of the field reconstruction errors for UKF-based tomography using the first order 3-D spatial-temporal AR model and TDSI for three selected snapshots  $t = 50, 100, 150$ , and 250 on the synthetic data, respectively. The histograms for the reconstruction errors for the UKF-based acoustic tomography and the TDSI methods are also plotted in blue and red, respectively. Closer investigation of these histograms together with the error images show that the UKF-based acoustic tomography provides a more accurate reconstructions compared to those of the TDSI method.

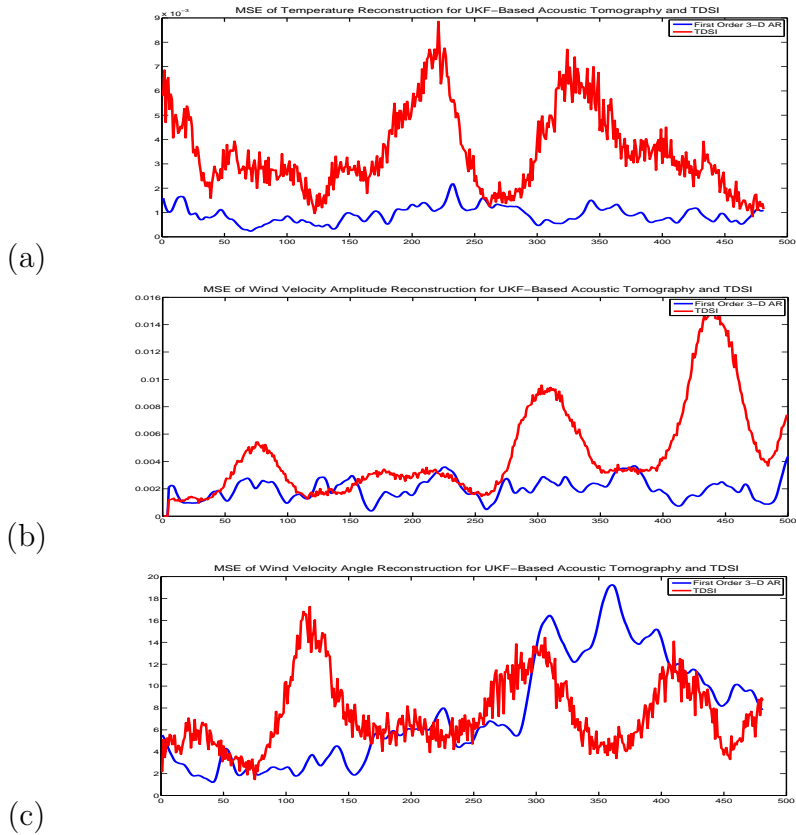


**Figure 6.5:** Comparison of field reconstruction MSEs of UKF-based acoustic tomography using the first order 3-D AR model and the TDSI method in (a) Temperature (b) Wind velocity amplitude (c) Wind velocity angle reconstruction over all snapshots.

The computational complexity of the TDSI method, is  $O([(M + 1) * N]^3)$ , where  $M+1$  is the number of snapshots used to reconstruct the fields at a single snapshot and  $N$  is the number of paths. In our experiment we have used  $M = 4$  past observations for

$N = 96$  acoustic paths at every snapshot. Compared to the computational complexity of the UKF-based acoustic tomography,  $O(L^3)$  with  $L = 96$ , the TDSI operates about  $(M + 1)^3$  times slower than the UKF-based algorithm.

Overall, the UKF-based acoustic tomography outperforms the TDSI method in reconstruction accuracy as well as computational complexity. Furthermore, it is shown in [11, 63] that the reconstruction accuracy of the TDSI method is higher than that of SI and SIRT. Therefore, one would expect that the reconstruction accuracy of UKF-based algorithm also outperforms those of the SI and SIRT.

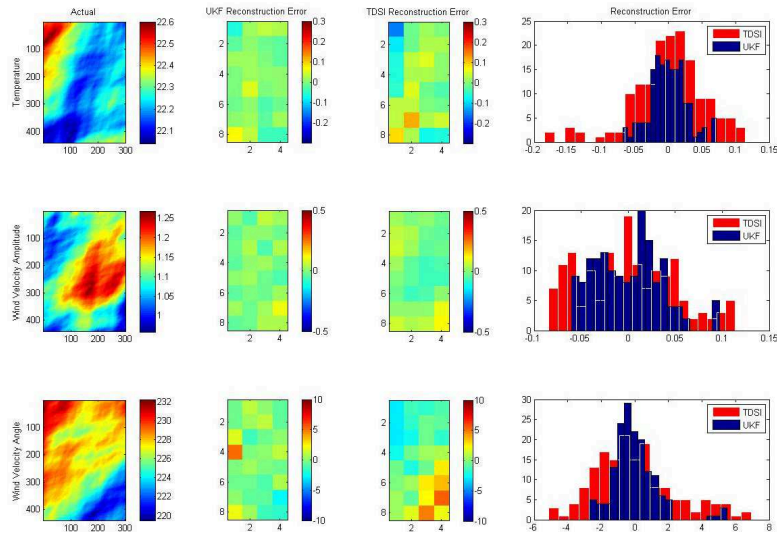


**Figure 6.6:** Comparison of temperature and wind velocity fields reconstructions of snapshot number 50, for UKF-based acoustic tomography using the first order 3-D AR model and the TDSI method. The histogram is plotted for reconstruction errors of snapshots 48 through 52.

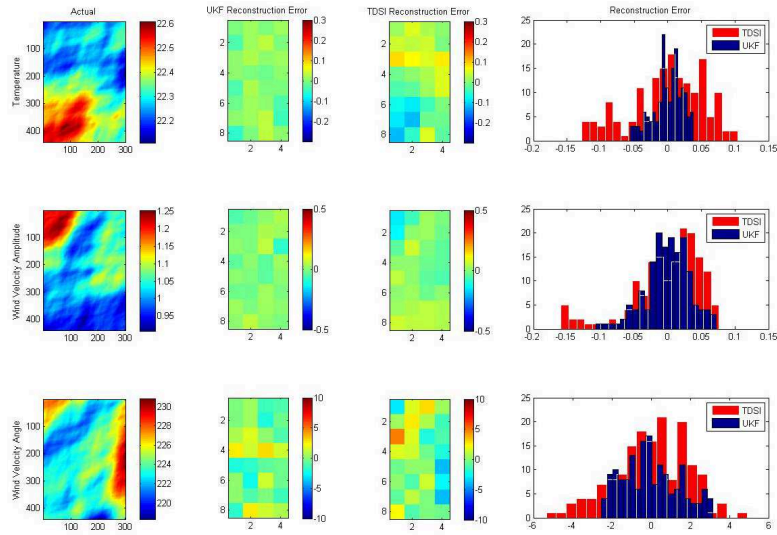


**Figure 6.7:** Comparison of temperature and wind velocity fields reconstructions of snapshot number 100, for UKF-based acoustic tomography using the first order 3-D AR model and the TDSI method. The histogram is plotted for reconstruction errors of snapshots 98 through 102.

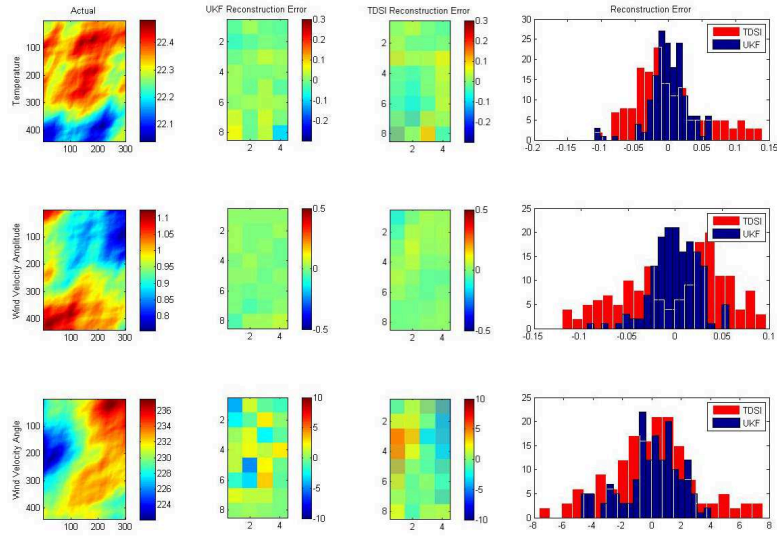


**Figure 6.8:** Comparison of temperature and wind velocity fields reconstructions of snapshot number 150, for UKF-based acoustic tomography using the first order 3-D AR model and the TDSI method. The histogram is plotted for reconstruction errors of snapshots 148 through 152.

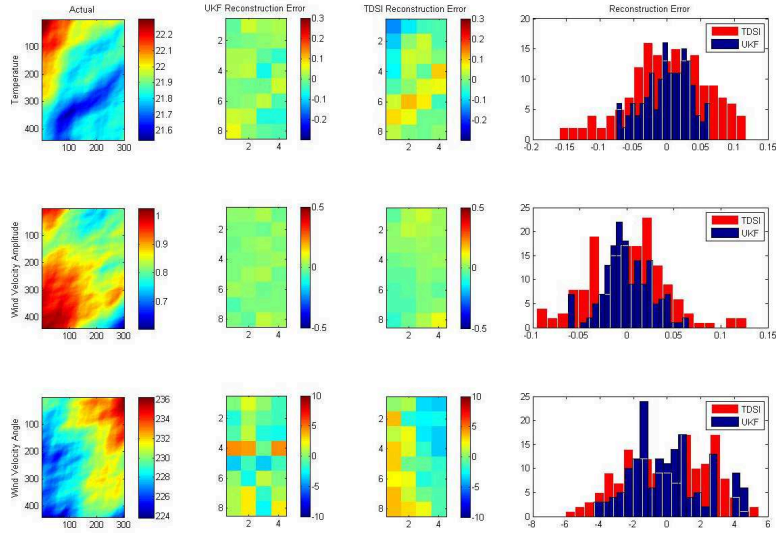


**Figure 6.9:** Comparison of temperature and wind velocity fields reconstructions of snapshot number 250, for UKF-based acoustic tomography using the first order 3-D AR model and the TDSI method. The histogram is plotted for reconstruction errors of snapshots 248 through 252.

### 6.3 Results on Real Data Sets

In this section, we have used the real data set collected at the Meteorological Observatory, Lindenberg, Germany, within the project STINHO. The size of the investigation field and the location of the sensors are the same as in Figure 5.2. The TOAs are measured every minute as opposed to every 12sec in the synthesized data. The data set is missing the TOA measurements for 17 of the paths for all snapshots (1038 snapshots). Therefore, the total number of observations reduces from 96 to 79.

Figure 6.10 shows the TOA measurements over all snapshots as a binary matrix in which 0 and 1 denote whether the data is missing or not, and are illustrated with blue and green, respectively. This presents a major difficulty when processing the data using a recursive process such as UKF. As it can be seen from Figure 6.10, in addition to the missing data for those 17 paths, the data is also missing randomly throughout the snapshots, which can be due to equipment malfunction.

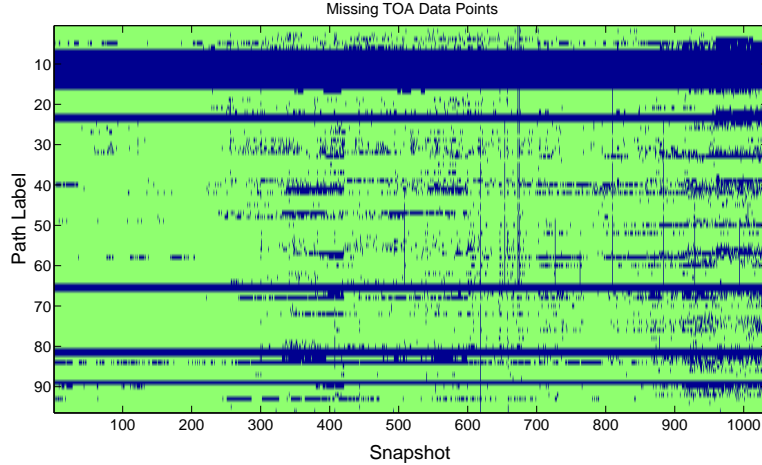


**Figure 6.10:** The TOA measurements and the missing data points.

In order to deal with the random missing measurements, a cubic spline piecewise regression interpolation [64] is used to interpolate those randomly missing data points, for every path.

The acquired data set has only two in-situ measurements for temperature with no measurement for wind velocity. Although, other research groups from German Weather Service and University of Bayreuth, have more excessive in-situ measurements for temperature and wind velocity fields, unfortunately we could not use those data sets.

Figure 6.11 shows the actual investigation field and the location of the two in-situ temperature sensors,  $T1$  and  $T2$ . It can be seen that the in-situ sensors are located at grids  $[i = 1, j = 4]$  and  $[i = 3, j = 5]$ .

The first order 3-D AR state evolution model is also used here to capture the dynamics of the state evolution. However, in the case of working with real data, there is no training data set to capture the state model parameters. Therefore, we employed the dual estimation framework and used dual UKF presented in Section 3.5 of Chapter 3, to update the state evolution model parameters at every snapshot during the UKF process.

It is assumed that  $\mathbf{v}_t$ ,  $\mathbf{u}_t$ , and  $\mathbf{n}_t$  are mutually uncorrelated, zero mean Gaussian

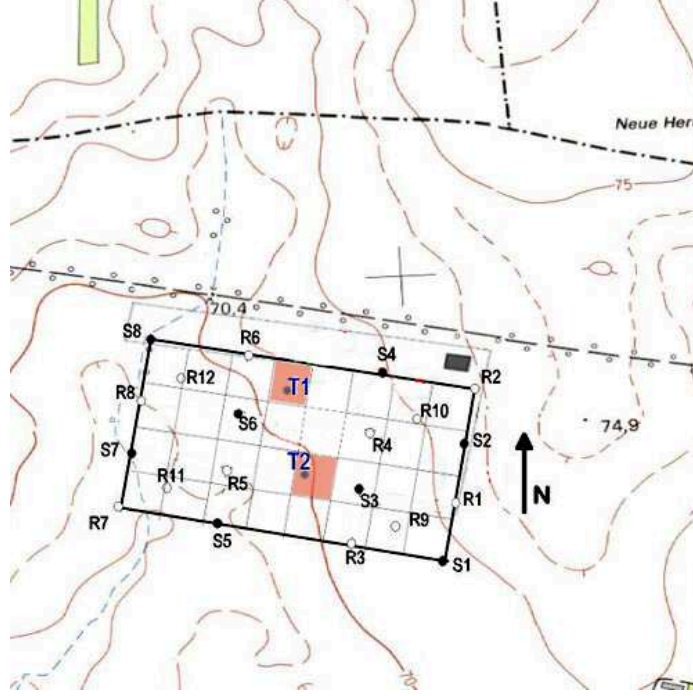


**Figure 6.11:** The investigation field with the in-situ temperature sensors.

processes with covariance matrices  $R_v = \sigma_v^2 I$ ,  $R_u$ , and  $R_n = \sigma_n^2 I$ , respectively where  $\sigma_v^2 = 0.01$  is chosen based upon the uncertainty measurements as mentioned before and  $\sigma_n^2 = 0.0025$  is chosen as the variance of parameter evolution driving noise. Note that  $\sigma_n^2$  is chosen based on the maximum range of the fluctuations of the state evolution parameters observed in the synthetic data, which was 0.15. Finally, assuming that the overall statistical properties of the real data are close to those of the synthesized data we used the same estimated  $R_u$  as in the previous experiment as the state evolution driving noise covariance matrix.

The mean temperature and wind velocity fields for the first snapshot are first calculated using the method described in Chapter 3 and used as the initial state  $\hat{\mathbf{x}}_{0|0} = [\bar{\mathbf{c}}_L^T(t_0), \bar{\boldsymbol{\alpha}}^T(t_0), \bar{\boldsymbol{\theta}}^T(t_0)]^T$ . The initial parameter vector is chosen to be  $\boldsymbol{\rho}_{0|0} = [1, 0, 0, 1, 0, 0, 1, 0, 0]^T$ , which corresponds to starting from a random walk model. Furthermore, the state and parameter error covariance matrices are taken to be  $P_{0|0} = \mathbf{I}_{96 \times 96}$  and  $P_{0|0}^\rho = \mathbf{I}_{9 \times 9}$ , respectively.

Having these initial values as well as those for  $R_v$ ,  $R_u$ ,  $R_n$ , and using the interpolated TOA measurements as the observation vector at every snapshot, the temperature and wind velocity fields were reconstructed using the dual-UKF method.

In order to evaluate the reconstruction accuracy of the proposed method, the reconstructed temperature at the grids  $[i = 1, j = 4]$  and  $[i = 3, j = 5]$  (See Figure 6.11), were compared to the reported temperature from nodes  $T1$  and  $T2$ . Figures 6.12 and 6.13 show the reported and reconstructed temperature for the first 300 snapshots together with the histogram of the reconstruction error for these snapshots. It can be seen from these figures that the fixed point iterative UKF-based acoustic tomography method tracks the temperature field successfully during this 300 snapshots.

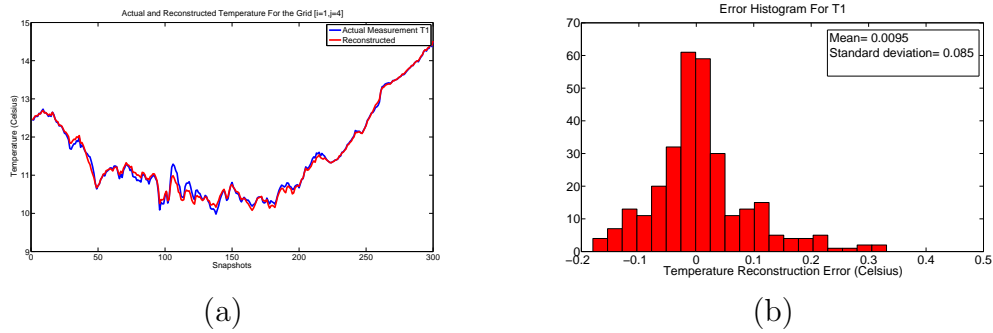


**Figure 6.12:** (a) The actual and reconstructed temperature at the grid  $[i = 1, j = 4]$   
 (b) The reconstruction error histogram

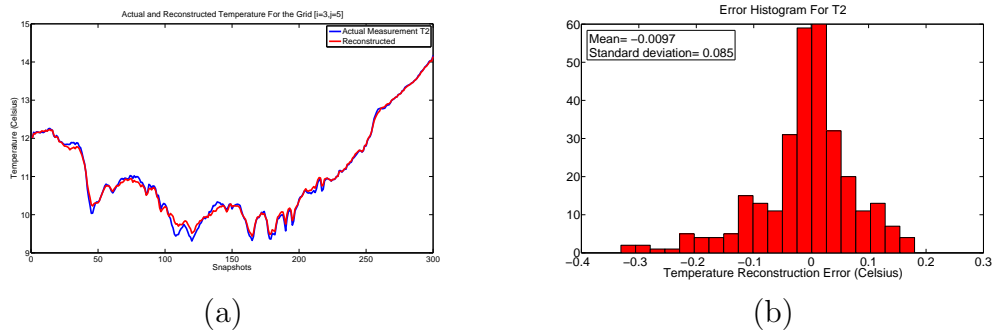


**Figure 6.13:** (a) The actual and reconstructed temperature at the grid  $[i = 3, j = 5]$   
 (b) The reconstruction error histogram

Finally, Figure 6.14-6.19 show the reconstructed temperature and wind velocity fields for 20 minutes 0 : 50 – 0 : 70 UTC with 4 minutes increments. As can be seen

from these, the reconstructed fields over this time period are consistent and changing gradually, as expected.

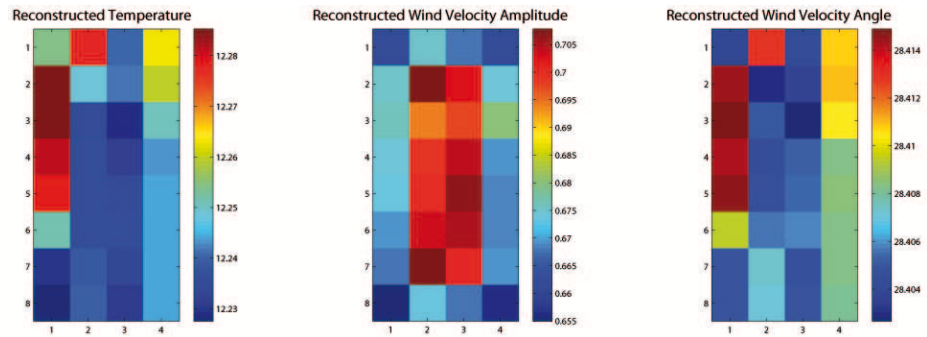


**Figure 6.14:** The reconstructed temperature and wind velocity fields for the snapshot number 50.

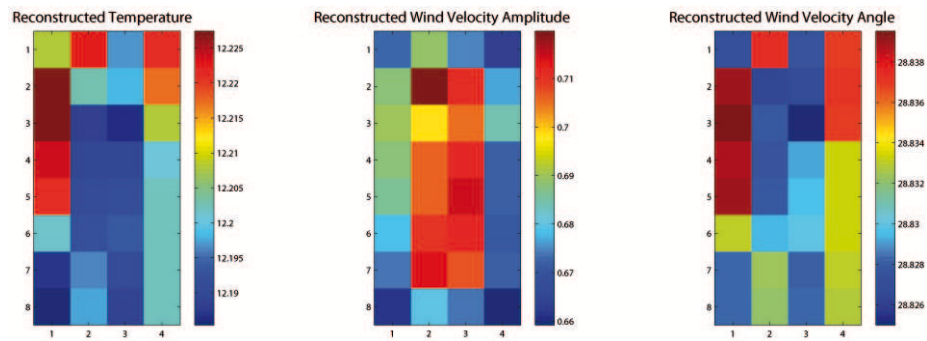


**Figure 6.15:** The reconstructed temperature and wind velocity fields for the snapshot number 54.

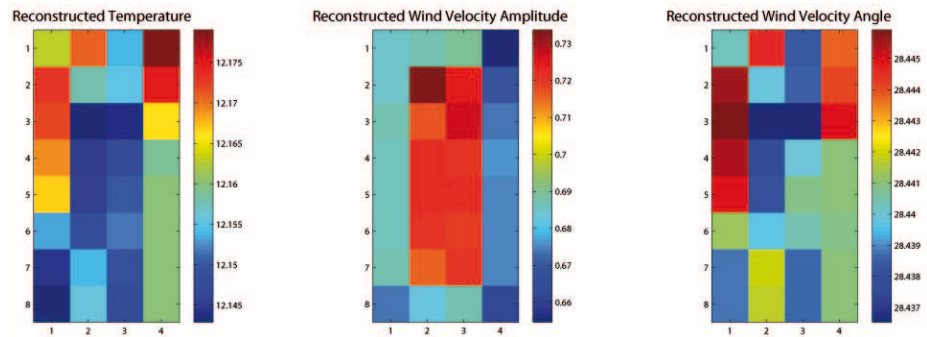


**Figure 6.16:** The reconstructed temperature and wind velocity fields for the snapshot number 58.

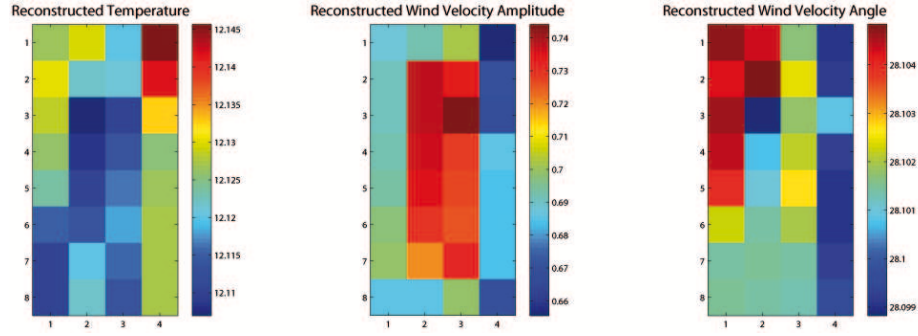


**Figure 6.17:** The reconstructed temperature and wind velocity fields for the snapshot number 62.

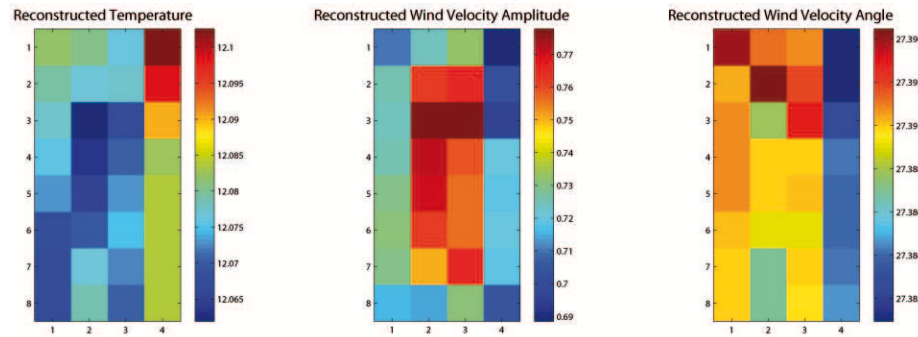


**Figure 6.18:** The reconstructed temperature and wind velocity fields for the snapshot number 66.

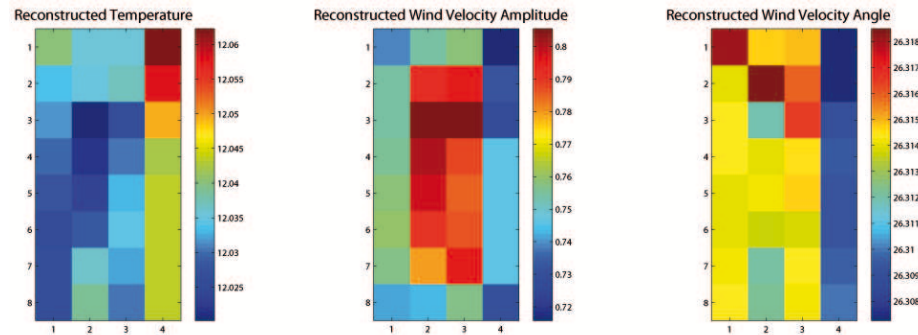


**Figure 6.19:** The reconstructed temperature and wind velocity fields for the snapshot number 70.

## 6.4 Conclusion

In this Chapter the UKF-based acoustic tomography algorithm was tested on the synthetic and the real data set. Two experiments were conducted in order to study the accuracy performance of the proposed method. In the first experiment, we focused

on the synthetic data set and aimed for finding the best state evolution model among three linear models, namely random walk, first order 3-D AR, and temporal AR models. These models were compared against each other and it was shown that the first order 3-D AR model outperformed the others in reconstruction accuracy as well as the computational complexity.

Next, the UKF-based acoustic tomography using the first order 3-D AR model was compared with the TDSI method. It was shown that the UKF-based method reconstructs the temperature and wind velocity amplitude fields more accurately, while performing almost the same in the wind velocity angle reconstruction. Moreover, it was shown that the UKF-based method is substantially faster than the TDSI method. The computation time for the iterated UKF with  $K = 3$  at every snapshot was found to be approximately 5sec (on synthesized data) on a computer with Intel Core i7 CPU, 12.0GB RAM, and 64bit operating system while it takes approximately 200sec for the TDSI method. Thus, the proposed UKF-based method is highly computationally efficient, ideally suited for applications where near real-time state estimation is required.

In the second experiment, the UKF-based acoustic tomography method was applied to the real data set. The reconstructed fields were compared to the two available in-situ measurements for temperature reconstruction and it was shown that the reconstruction field closely follows the measured values. The temperature reconstruction error was reported to have mean and standard deviation of approximately zero and 0.085 , respectively.

Not having adequate number of in-situ measurements, makes it difficult to evaluate the performance of the method exclusively. However, relying on the comparison of the reconstruction results with the available in-situ measurements the UKF-based acoustic tomography method was succeeded in the temperature and wind velocity reconstruction using the real data.

# CHAPTER 7

## CONCLUSIONS AND SUGGESTIONS FOR FUTURE WORK

### 7.1 Conclusions and Discussions

Acoustic tomography of the atmosphere is a nonlinear inverse problem which attempts to reconstruct temperature and wind velocity fields in the atmospheric surface layer (ASL) using the nonlinear dependence of the travel time of an acoustic wave on temperature and wind velocity fields along the propagation path. Using acoustic tomography is shown to be highly beneficial [7], as it uses a small number of acoustic sensors to reconstruct the temperature and wind velocity fields with high spatial resolution. However, Acoustic tomography of the atmosphere is an underdetermined nonlinear inverse problem, which is in general difficult to solve.

Several acoustic tomography methods have recently been introduced that can be categorized as statistical-based algorithms [7, 11], algebraic-based algorithms [9, 17] and those which use sparse reconstruction framework [18]. Part of this work is devoted to studying these methods and reviewing the required assumptions for each method. Our ultimate goal in this work was to develop a new statistical-based algorithm with minimal simplifying assumptions and better performance. Hence, a new statistical-based approach toward solving the acoustic tomography problem was presented which casts the problem as a nonlinear state-estimation problem in which states represent the temperature and wind velocity fields in each grid over the monitored area. Unscented Kalman filter (UKF) [39] is employed to estimate and track these states at every time snapshot. UKF is based on Unscented Transform

method which does not require linearization of the state or observation equations.

First we reviewed the acoustic tomography formulation in Chapter 2 and showed that the TOA is a nonlinear function of temperature and wind velocity fields. Several atmospheric acoustic tomography methods and their assumptions were reviewed in detail. This included SI [7] and TDSI [11] that are statistical-based algorithms as they solve the inverse problem by applying the Wiener filter to the first order linear approximation of the forward problem. It was discussed that using Wiener filter requires knowledge about the statistical characteristics of the temperature and wind velocity fields and since these characteristics are unknown, optimal stochastic inverse is not generally feasible. Then, we reviewed SIRT method [9], representing the algebraic-based acoustic tomography methods. It was shown that algebraic-based methods require no initial knowledge about the statistics of the temperature and wind velocity fields, however their formulation requires reciprocal measurements, which may not be cost-effective and realistic. We also reviewed the acoustic tomography algorithms which use the sparse reconstruction framework, e.g., [18], and discussed the feasibility of their required assumptions such as non-moving atmosphere and the sparsity of the fields in the atmosphere and questioned the applicability of these algorithms to real-life applications.

In Chapter 3 the idea behind UKF and its different variations were presented to prepare the foundation for the subsequent chapters. The Unscented Transform (UT) process was described and utilized to derive the UKF. The original UKF was explained in detail followed by the cases of state estimation and dual state-parameter estimation. Then, the fixed point UKF was introduced as a better method to solve the problems with large uncertainty in the choice of the initial error covariance matrix and low SNR or insufficient measurements. The performance of UKF highly depends on the accuracy of (a) the state evolution model, (b) the observation model, (c) the covariance matrix of the driving noise, and (d) the covariance matrix of the

observation noise. We discussed that when state evolution model is unknown or has many different stochastic parameters, the dual state-parameter estimation UKF should be used instead of the original UKF to estimate the state and model parameters simultaneously from the observations. We also showed that the concept of fixed point iteration can be extended to all variations of the UKF.

The new statistical-based acoustic tomography algorithm was proposed and formulated in Chapter 4. The proposed method casts the problem as a state estimation problem and solves the non-linear state estimation problem using UKF. Three different linear models, namely random walk, first order spatial-temporal 3-D AR, and third order temporal AR models were suggested and formulated in order to capture the state dynamics over time in an investigation area. The state-space equations are then formed based on the state evolution model and the TOA formulation.

In order to test our proposed UKF-based algorithm a data set was acquired from the university of Leipzig, collected at the Meteorological Observatory, Lindenberg, Germany, within the project STINHO [27]. The data set consists of the TOAs for a field of size  $300m \times 440m$  with 8 transmitters and 12 receivers (96 paths and TOA measurements). The detailed explanation of these experiments can be found in [27]. However, the lack of sufficient in situ measurements (only 2 temperature sensors) for a complete evaluation of the developed algorithm motivated us to devise a method to construct a synthetic but close to realistic data set, using the same setup as in STINHO. The process of generating the synthetic temperature and wind velocity data sets is then reviewed in Chapter 5. Knowing the fact that the atmospheric patterns have fractal properties [62], the fractal Brownian motion (fBm) [57, 58] was used as the model to generate random wind velocity and temperature fields. The 1-D and 2-D Fourier-based filtering method was studied in order to generate realizations of the random fields. The random temperature and wind velocity fields are generated for a single snapshot in an area 10 times bigger than the investigation field ( $300m \times 440m$ ).

Then, the frozen turbulence assumption is used to generate the data in time from the single oversized snapshot. The synthetic data set was generated with spatial resolution of  $1m$  and temporal resolution of  $12sec$  for 500 snapshots. These temperature and wind velocity synthetic fields are then used to calculate the TOAs for all the paths. Furthermore, an additive zero mean Gaussian process is employed to simulate the effect of the measurement noise. It was noted that the same process can be used to generate a 3-D random temperature and wind velocity data sets in order to study the performance of the tomography methods for 3-D temperature and wind velocity reconstruction.

Finally the UKF-based acoustic tomography algorithm was tested on the synthetic and the real data set in Chapter 6. First, we aimed for finding the best state evolution model among the three linear models presented in Chapter 4. Hence, the proposed method was applied to the synthesized data set, using these three state evolution models. The results were compared against each other and it was shown that the first order spatial-temporal 3-D AR model outperformed the others in reconstruction accuracy as well as the computational complexity. Next, the UKF-based acoustic tomography using the first order 3-D AR model was compared with the TDSI method [11]. It was shown that the UKF-based method outperforms the TDSI method in reconstruction accuracy as well as computational efficiency. Given the fact that TDSI outperforms the SI and SIRT methods, one would expect that the reconstruction accuracy of the UKF-based algorithm is also better than those of the SI and SIRT. This is due to the observation that the TDSI method outperformed these methods in benchmarking results presented in [11, 63]

In the second experiment, the UKF-based acoustic tomography method was applied to the real data set. The dual UKF is used to reconstruct the temperature and wind velocity fields as well as state evolution model parameters. The reconstructed

fields were compared to the two available in-situ measurements for temperature reconstruction. Not having adequate number of in-situ measurements, makes it difficult to evaluate the performance of the method extensively. However, relying on the comparison of the reconstruction results with the available two in-situ temperature measurements the UKF-based acoustic tomography method was found to produce good temperature reconstruction with mean and standard deviation of approximately zero and 0.085 , respectively. Moreover, the reconstructed fields are found to be temporally consistent, meaning that they change gradually in time, as it is expected from near surface atmospheric fields.

Based on the results presented in Chapter 6 it is evident that the UKF-based acoustic tomography method is a computationally efficient method capable of reconstructing and tracking the temperature and wind velocity fields accurately. Most of the assumptions used by other acoustic tomography methods [7, 9, 11], such as the linearization process, stationarity of the fields, and reciprocal measurements are lifted in the proposed method. This work opens a new avenue to acoustic tomography of the atmosphere and demonstrates the usefulness of the UKF for nonlinear tomography problems.

## 7.2 Future Work

Although, the UKF-based acoustic tomography proposed in this thesis offers an accurate solution to the acoustic tomography problem, there is still room for improvements in many different aspects which can be pursued in the future. These include, but are not limited to:

- The straight-ray model was used in this study to model the acoustic wave propagation in the atmospheric surface layer. The next step in the development would be to use the bent-ray model, and take into account the information from the direction of arrivals (DOAs), in addition to the TOAs [19].

- Different state evolution models with adaptive parameters can be studied in order to find more realistic models which capture the state dynamics better.
- The UKF-based acoustic tomography formulation could be changed in the future in order to deal with randomly missing data.
- The real data used in this study was lacking adequate in-situ measurements. In order to evaluate the method more elaborately a data set with more in-situ measurements should be used in the future studies.
- It would be interesting to study the acoustic tomography of the atmosphere using particle filters [65,66] which do not require Gaussianity and compare the results to those of the UKF-based acoustic tomography.
- Studying the impact of this UKF-based approach to other tomography problems such as brain imaging could be of great interest.

## REFERENCES

- [1] J. Baruchel, J. Y. Buffiere, E. Maire, P. Merle, and G. Peix, *X-Ray Tomography in Material Science*. Hermes Science Publications, 2000.
- [2] M. F. Reiser, W. Semmler, and H. Hricak, *Magnetic Resonance Tomography*. New York: Springer, 2008.
- [3] W. Munk and C. Wunsch, “Ocean acoustic tomography - rays and modes,” *Reviews of Geophysics*, vol. 21, no. 4, pp. 777–793, 1983.
- [4] W. K. Graber, “SODAR monitoring of the atmosphere - recent developments,” *Applied Physics B: Lasers and Optics*, vol. 57, pp. 1–2, 1993.
- [5] J. L. Spiesberger and K. M. Fristrup, “Passive localization of calling animals and sensing of their acoustic environment using acoustic tomography,” *The American Naturalist*, vol. 135, pp. 107–153, 1990.
- [6] V. I. Tatarskii, *The effects of the turbulent atmosphere on wave propagation*. Moscow, 1967, Israel Program for Scientific Translations, U.S. Dept. of Commerce: Nauka, 1971.
- [7] D. K. Wilson and D. W. Thomson, “Acoustic tomographic monitoring of the atmospheric surface layer,” *Atmospheric and Oceanic Technology*, vol. 11, pp. 751–769, June 1994.
- [8] D. K. Wilson, A. Ziemann, V. E. Ostashev, and A. G. Voronovich, “An overview of acoustic travel-time tomography in the atmosphere and its potential applications,” *Acustica*, vol. 87, pp. 721–730, 2001.

- [9] A. Ziemann, K. Arnold, and A. Raabe, “Acoustic travel time tomography - a method for remote sensing of the atmospheric surface layer,” *Meteorology and Atmospheric Physics*, vol. 71, pp. 43–51, April 1999.
- [10] K. Arnold, A. Ziemann, A. Raabe, and G. Spindler, “Acoustic tomography and conventional meteorological measurements over heterogeneous surfaces,” *Meteorology and Atmospheric Physics*, vol. 85, pp. 175–186, 2004.
- [11] S. N. Vecherin, V. E. Ostashev, G. H. Goedecke, D. K. Wilson, and A. G. Voronovich, “Time-dependent stochastic inversion in acoustic travel-time tomography of the atmosphere,” *The Journal of the Acoustical Society of America*, vol. 119, pp. 2579–2588, May 2006.
- [12] S. N. Vecherin, V. E. Ostashev, A. Ziemann, D. K. Wilson, K. Arnold, and M. Barth, “Tomographic reconstruction of atmospheric turbulence with the use of time-dependent stochastic inversion,” *Journal of the Acoustical Society of America*, vol. 122, pp. 1416–1425, 2007.
- [13] M. Barth and A. Raabe, “Acoustic tomographic imaging of temperature and flow fields in air,” *Measurement Science and Technology*, vol. 22, pp. 2579–2588, March 2011.
- [14] W. Munk, P. Worcester, and C. Wunsch, *Ocean acoustic tomography*. 40 West 20th Street, New York, NY, 10011-4211, USA: Cambridge University Press, 1995.
- [15] M. McCarron, M. R. Azimi-Sadjadi, and M. Mungiole, “An operationally adaptive system for rapid acoustic transmission loss prediction,” *Neural Networks*, vol. 27, pp. 91 – 99, 2012.
- [16] G. Wichern, M. R. Azimi-Sadjadi, and M. Mungiole, “Environmentally adaptive acoustic transmission loss prediction in turbulent and nonturbulent atmospheres,” *Neural Networks*, vol. 20, no. 4, pp. 484–497, 2007.

- [17] K. Arnold, A. Ziemann, and A. Raabe, “Tomographic monitoring of wind and temperature at different heights above the ground,” *Acustica*, vol. 87, pp. 703–708, 2001.
- [18] I. Jovanovic, A. Hormati, L. Sbaiz, and M. Vetterli, “Efficient and stable acoustic tomography using sparse reconstruction methods,” *19th International Congress on*, no. September, pp. 2–7, 2007.
- [19] I. Jovanovi, “Acoustic tomography for scalar and vector fields : theory and application to temperature and wind estimation,” *Journal of Atmospheric and Oceanic Technology*, pp. 1–15, 2009.
- [20] L. Scharf and C. Demeure, *Statistical signal processing: detection, estimation, and time series analysis*. Addison-Wesley series in electrical engineering, Addison-Wesley Pub. Co., 1991.
- [21] S. Kodali, K. Deb, P. Munshi, and N. Kishore, “Comparing GA with MART to tomographic reconstruction of ultrasound images with and without noisy input data,” in *Evolutionary Computation, 2009. CEC '09. IEEE Congress on*, pp. 2963 –2970, May 2009.
- [22] S. J. Julier, “New extension of the Kalman filter to nonlinear systems,” *Proceedings of SPIE*, vol. 3, pp. 182–193, 1997.
- [23] S. Julier and J. Uhlmann, “Unscented filtering and nonlinear estimation,” *Proceedings of the IEEE*, vol. 92, pp. 401–422, 2004.
- [24] E. A. Wan and R. V. Merwe, “The unscented Kalman filter,” in *Kalman filtering and neural networks* (S. S. Haykin, ed.), ch. 7, pp. 221–277, New York, US: John Wiley and Sons, 2001.

- [25] S. Julier, “The scaled unscented transformation,” *Proceedings of the 2002 American Control Conference IEEE*, vol. 6, pp. 4555–4559, 2002.
- [26] G. Welch and G. Bishop, “An introduction to the Kalman filter,” *Design*, vol. 7, pp. 1–16, 2001.
- [27] A. Raabe, A. Klaus, A. Ziemann, M. Schroter, S. Raasch, J. Bange, P. Zittel, T. Spieb, T. Foken, M. Gockede, F. Beyrich, and J. P. Leps, “STINHO, structure of turbulent transport under inhomogeneous surface conditions,” *Meteorologische*, vol. 14, pp. 315–327, 2005.
- [28] V. Ostashev, *Acoustics in Moving Inhomogeneous Media*. E & FN Spon, 1997.
- [29] S. M. Kay, *Fundamentals of Statistical Processing, Volume I : Estimation Theory*. Prentice Hall, 1993.
- [30] E. Piccolomini, “The conjugate gradient regularization method in computed tomography problems,” *Applied Mathematics and Computation*, vol. 102, pp. 87–99, 1999.
- [31] A. H. Andersen and A. C. Kak, “Simultaneous algebraic reconstruction technique (SART): a superior implementation of the art algorithm.,” *Ultrasonic Imaging*, vol. 6, pp. 81–94, 1984.
- [32] E. Cand, “Sparsity and incoherence in compressive sampling,” *Bernoulli*, vol. 23, pp. 1–20, 2006.
- [33] D. Donoho, “Compressed sensing,” *Information Theory, IEEE Transactions on*, vol. 52, pp. 1289–1306, April 2006.
- [34] R. J. Vanderbei, *Linear Programming: Foundations and Extensions*, vol. 49. Springer, 2001.

- [35] J. C. Tannehill, D. A. Anderson, and R. H. Pletcher, *Computational Fluid Mechanics and Heat Transfer*. Taylor and Francis, 1997.
- [36] R. E. Kalman, “A new approach to linear filtering and prediction problems,” *Journal Of Basic Engineering*, vol. 82, pp. 35–45, 1960.
- [37] H. Sorenson, *Kalman filtering: theory and application*. IEEE Press selected reprint series, IEEE Press, 1960.
- [38] S. Julier and J. K. Uhlmann, “A general method for approximating nonlinear transformations of probability distributions,” *Transformation*, vol. 4, pp. 1–27, 1996.
- [39] R. V. Merwe and W. Eric, “Sigma-point Kalman filters for probabilistic inference in dynamic state-space models,” *PhD thesis*, pp. 1–378, April 2004.
- [40] R. A. Howard, *Dynamic Programming and Markov Processes*. MIT Press, 1960.
- [41] G. Kitagawa, “Monte-Carlo filter and smoother for non-gaussian nonlinear state space models,” *Journal Of Computational And Graphical Statistics*, vol. 5, no. 1, pp. 1–25, 1996.
- [42] J. Gentle, *Numerical Linear Algebra for Applications in Statistics*. Statistics and Computing, Springer, 1998.
- [43] M. C. Vandyke, J. L. Schwartz, and C. D. Hall, “Unscented Kalman filtering for spacecraft attitude state and parameter estimation,” *Aerospace*, vol. 115, pp. 1–13, 2004.
- [44] A. Sitz, U. Schwarz, J. Kurths, and H. U. Voss, “Estimation of parameters and unobserved components for nonlinear systems from noisy time series,” *Physical Review E - Statistical, Nonlinear and Soft Matter Physics*, vol. 66, p. 016210, 2002.

- [45] J. H. Gove and D. Y. Hollinger, “Application of a dual unscented Kalman filter for simultaneous state and parameter estimation in problems of surface-atmosphere exchange,” *Journal of Geophysical Research*, vol. 111, no. D8, pp. 1–21, 2006.
- [46] R. Zhan and J. Wan, “Iterated unscented Kalman filter for passive target tracking,” *Aerospace and Electronic Systems, IEEE Transactions on*, vol. 43, pp. 1155–1163, July 2007.
- [47] F. Spitzer, *Principles of Random Walk*. Springer, 2001.
- [48] P. J. Brockwell and R. A. Davis, *Introduction to Time Series and Forecasting*, vol. 39. Springer, 2002.
- [49] O. Khorloo, Z. Gunjee, and B. Sosorbaram, “Wind field synthesis for animating wind-induced vibration,” *The International Journal of Virtual Reality*, vol. 10, pp. 53–60, February 2011.
- [50] M. Shinya and A. Fournier, “Stochastic motion - motion under the influence of wind,” *Computer Graphics Forum*, vol. 11, 1992.
- [51] J. Stam and E. Fiu, “Turbulent wind fields for gaseous phenomena,” in *Proceedings of the 20th annual conference on Computer graphics and interactive techniques*, SIGGRAPH ’93, (New York, NY, USA), pp. 369–376, ACM, 1993.
- [52] J. Stam, “Stable fluids,” in *Proceedings of the 26th annual conference on Computer graphics and interactive techniques*, SIGGRAPH ’99, (New York, NY, USA), pp. 121–128, ACM Press/Addison-Wesley Publishing Co., 1999.
- [53] N. Foster and D. Metaxas, “Modeling the motion of a hot, turbulent gas,” in *Proceedings of the 24th annual conference on Computer graphics and interactive*

- techniques*, (New York, NY, USA), pp. 181–188, ACM Press/Addison-Wesley Publishing Co., 1997.
- [54] M. Keshner, “1/f noise,” *Proceedings of the IEEE*, vol. 70, pp. 212 – 218, March 1982.
- [55] I. Karatzas and S. E. Shreve, *Brownian Motion and Stochastic Calculus*, vol. 113. Springer, 1991.
- [56] D. Chandler, *Introduction to Modern Statistical Mechanics*. Oxford University Press, 1987.
- [57] L. Decreusefond and A. S. stnel, “Stochastic analysis of the fractional Brownian motion,” *Potential Analysis*, vol. 10, pp. 177–214, 1999.
- [58] D. Nualart, *Fractional Brownian motion : stochastic calculus and applications*, vol. 5, pp. 75–86. European Mathematical Society, 2006.
- [59] R. F. Voss, *The science of fractal images*. Springer-Verlag, 1988.
- [60] B. B. Mandelbrot and J. W. Van Ness, “Fractional brownian motions, fractional noises and applications,” *SIAM Review*, vol. 10, p. 422437, 1968.
- [61] A. Schuster, “On the investigation of hidden periodicities with application to a supposed twenty-six-day period of meteorological phenomena,” *Terr Mag*, vol. 3, pp. 13–41, 1898.
- [62] F. Ludwig, “Atmospheric fractals : a review,” *Environmental Software*, vol. 4, pp. 9 – 16, 1989.
- [63] S. N. Vecherin, V. E. Ostashev, D. K. Wilson, and A. Ziemann, “Time-dependent stochastic inversion in acoustic tomography of the atmosphere with reciprocal sound transmission,” *Measurement Science Technology*, vol. 19, 2008.

- [64] D. J. Poirier, “Piecewise regression using cubic splines,” *Journal of the American Statistical Association*, vol. 68, no. 343, pp. 515–524, 1973.
- [65] R. Van Der Merwe, A. Doucet, N. De Freitas, and E. Wan, “The unscented particle filter,” *Advances in Neural Information Processing Systems*, vol. 96, no. CUED/F-INFENG/TR 380, p. 584590, 2001.
- [66] J. Carpenter, P. Clifford, and P. Fearnhead, “Improved particle filter for nonlinear problems,” *IEEE Proceedings - Radar Sonar and Navigation*, vol. 146, no. 1, pp. 2–7, 1999.

# APPENDIX A

## SIRT FORMULATION

This appendix reviews the application of the simultaneously iterative reconstruction technique (SIRT) in acoustic tomography of the atmosphere. The acoustic propagation and the time of arrival (TOA) formulations are briefly reviewed. Finally, the SIRT framework is studied and the corresponding assumptions are investigated.

### A.1 Problem Formulation

The travel time for an acoustic wave to propagate from a source to a receiver is a function of temperature, wind velocity (air flow) and humidity along the path. However the effect of humidity on the travel time is somehow negligible and hence is typically be ignored. Acoustic tomography methods use this relation to reconstruct the temperature and wind velocity fields in an investigation area based on several travel time measurements between different sources and receivers deployed in an investigation area.

Assuming a straight-ray model for sound propagation, the sound speed along a propagation path can be written as

$$c_{ray}(\mathbf{r}, t) \approx c_L(\mathbf{r}, t) + \mathbf{s} \cdot \mathbf{v}(\mathbf{r}, t). \quad (\text{A.1})$$

where  $\mathbf{r}$  is the position vector of a point on the investigation area,  $\mathbf{s}$  is the unit vector in the direction of sound propagation,  $c_L$  is the Laplace sound speed (temperature dependent), and  $\mathbf{v}$  is the wind velocity vector.

Based on (A.1) the travel time formula for the  $n$ 'th path is defined as:

$$\tau_n(t) = \int_{L_n} \frac{dl_n}{c_{ray}(\mathbf{r}, t)} = \int_{L_n} \frac{dl_n}{c_L(\mathbf{r}, t) + \mathbf{s}_n \cdot \mathbf{v}(\mathbf{r}, t)}, \quad (\text{A.2})$$

where the integration is along the  $n$ 'th propagation path,  $L_n$  is the length of the  $n$ 'th propagation path and  $\mathbf{s}_n$  is the unit vector in its direction.

Discretizing the investigation area, into  $I \times J$  grids and assuming that  $c_L(\mathbf{r}, t)$  and  $\mathbf{v}(\mathbf{r}, t)$  are spatially constant in each grid, one can rewrite (A.2) as follow,

$$\tau_n(t) = \sum_{i=1}^I \sum_{j=1}^J \frac{d_n(i, j)}{c_L([i, j], t) + \mathbf{s}_n \cdot \mathbf{v}([i, j], t)}. \quad (\text{A.3})$$

Here  $d_n(i, j)$  is the distance  $n$ 'th propagation path travels in the  $(i, j)$ 'th cell,  $c_L([i, j], t)$  and  $\mathbf{v}([i, j], t)$  are the Laplace sound speed and the wind velocity vector in the  $(i, j)$ 'th grid at time  $t$ , respectively.

## A.2 SIRT

Acoustic tomography using SIRT employs reciprocal sensors to separate the effects of temperature and wind velocity and reformulate the problem. Figure A.1 shows the parameters used in the TOA formulation.

Note that there are two TOA measurements for the path shown in Figure A.1,  $R1 - R2$  and  $R2 - R1$  with respective TOA measurements  $\tau_{n,1}$  and  $\tau_{n,2}$ . Using (A.3) these measurements can be related to the Laplace sound speed and wind velocity fields as follow,

$$\tau_{n,1} = \sum_{i=1}^I \sum_{j=1}^J \frac{d_n(i, j)}{c_L(i, j) + \mathbf{s}_n \cdot \mathbf{v}(i, j)} \quad (\text{A.4})$$

$$\tau_{n,2} = \sum_{i=1}^I \sum_{j=1}^J \frac{d_n(i, j)}{c_L(i, j) - \mathbf{s}_n \cdot \mathbf{v}(i, j)}. \quad (\text{A.5})$$

In order to ease the derivation process and avoiding confusion the 2-D arrays  $d_n$ ,  $c_L$ , and  $\mathbf{v}$  are mapped into 1-D arrays (the notation is preserved), therefore the double

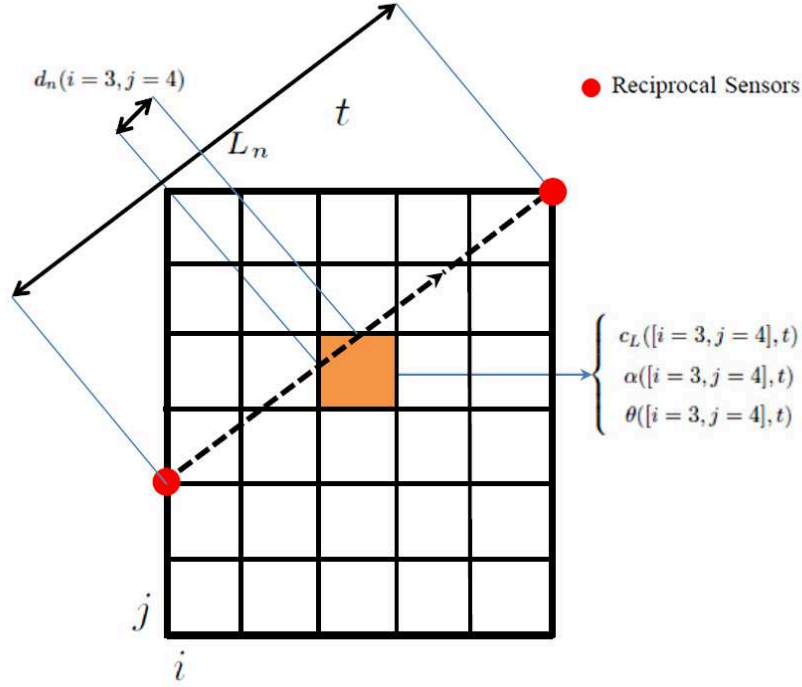


**Figure A.1:** A tomographic setup with reciprocal sensors

summation in (A.4) and (A.5) are substituted by a single summation as follow,

$$\tau_{n,1} = \sum_{i=1}^{IJ} \frac{d_n(i)}{c_L(i) + \mathbf{s}_n \cdot \mathbf{v}(i)} \quad (\text{A.6})$$

$$\tau_{n,2} = \sum_{i=1}^{IJ} \frac{d_n(i)}{c_L(i) - \mathbf{s}_n \cdot \mathbf{v}(i)}. \quad (\text{A.7})$$

The SIRT method then separates the effect of the temperature and wind velocity fields on the TOA by defining the effective sound speed,  $c^{eff}$ ,

$$c_{n,1}^{eff} \triangleq \frac{L_n}{\tau_{n,1}} \quad (\text{A.8})$$

$$c_{n,2}^{eff} \triangleq \frac{L_n}{\tau_{n,2}} \quad (\text{A.9})$$

and the effective sound speeds are assumed to be the superposition of the effective Laplace sound speed,  $c_{L,n}^{eff}$ , and the effective wind speed,  $v_n^{eff}$ , as follow,

$$c_{n,1}^{eff} = c_{L,n}^{eff} + v_n^{eff} \quad (\text{A.10})$$

$$c_{n,2}^{eff} = c_{L,n}^{eff} - v_n^{eff}. \quad (\text{A.11})$$

The SIRT-based acoustic tomography then defines the temperature-based TOA and wind-based TOA as follow,

$$\tau_n^{cL} \triangleq \frac{L}{c_{L,n}^{eff}} = \frac{2\tau_{n,1}\tau_{n,2}}{\tau_{n,2} + \tau_{n,1}} \quad (\text{A.12})$$

$$\tau_n^v \triangleq \frac{L}{v_n^{eff}} = \frac{2\tau_{n,1}\tau_{n,2}}{\tau_{n,2} - \tau_{n,1}} \quad (\text{A.13})$$

and states that  $\tau_n^{cL}$  represents the TOA for the  $n$ 'th path when the wind velocity is set to zero and  $\tau_n^v$  represents the case in which the Laplace sound speed is set to zero. Therefore, it claims that we can write,

$$\tau_n^{cL} = \sum_{i=1}^{IJ} \frac{d_n(i)}{c_L(i)} \quad (\text{A.14})$$

$$\tau_n^v = \sum_{i=1}^{IJ} \frac{d_n(i)}{\mathbf{s}_n \cdot \mathbf{v}(i)}. \quad (\text{A.15})$$

and reconstructs the Laplace sound speed and wind velocity fields separately using a gradient based iterative  $\ell_2$  minimization algorithm.

However, one can question the validity of (A.14) and (A.15). In the rest of this section, (A.14) and (A.15) are evaluated and the assumptions behind these claims are investigated.

### A.2.1 Temperature-Based TOA

Since we are evaluating (A.14) and (A.15) for an arbitrary path, in order to simplify the notation we drop the path subscription,  $n$ , in the rest of the derivations, knowing that the derivations are true for every path. From (A.12) and (A.14) we can write,

$$\frac{2\tau_1\tau_2}{\tau_2 + \tau_1} = \sum_{i=1}^{IJ} \frac{d(i)}{c_L(i)}, \quad (\text{A.16})$$

and our goal in this subsection is to investigate the validity of (A.16).

Using equations (A.6) and (A.7), we expand the left hand of the equation (A.16)

as follow,

$$\begin{aligned}
\frac{2\tau_1\tau_2}{\tau_2 + \tau_1} &= \frac{2 \sum_{i=1}^{IJ} \frac{d(i)}{c_L(i)+\mathbf{s}\cdot\mathbf{v}(i)} \sum_{j=1}^{IJ} \frac{d(j)}{c_L(j)-\mathbf{s}\cdot\mathbf{v}(j)}}{\sum_{j=1}^{IJ} \frac{d(j)}{c_L(j)-\mathbf{s}\cdot\mathbf{v}(j)} + \sum_{i=1}^{IJ} \frac{d(i)}{c_L(i)+\mathbf{s}\cdot\mathbf{v}(i)}}} \\
&= \frac{\sum_{i=1}^{IJ} \sum_{j=1}^{IJ} \frac{d(i)d(j)}{(c_L(i)+\mathbf{s}\cdot\mathbf{v}(i))(c_L(j)-\mathbf{s}\cdot\mathbf{v}(j))}}{\sum_{j=1}^{IJ} \frac{d(j)c_L(j)}{c_L^2(j)-(\mathbf{s}\cdot\mathbf{v}(j))^2}}. \tag{A.17}
\end{aligned}$$

Substituting (A.17) into (A.16) we have,

$$\begin{aligned}
\sum_{i=1}^{IJ} \frac{d(i)}{c_L(i)} &= \frac{\sum_{i=1}^{IJ} \sum_{j=1}^{IJ} \frac{d(i)d(j)}{(c_L(i)+\mathbf{s}\cdot\mathbf{v}(i))(c_L(j)-\mathbf{s}\cdot\mathbf{v}(j))}}{\sum_{j=1}^{IJ} \frac{d(j)c_L(j)}{c_L^2(j)-(\mathbf{s}\cdot\mathbf{v}(j))^2}} \\
\Rightarrow \sum_{i=1}^{IJ} \sum_{j=1}^{IJ} \frac{d(i)d(j)c_L(j)}{c_L(i)(c_L^2(j) - (\mathbf{s}\cdot\mathbf{v}(j))^2)} &= \sum_{i=1}^{IJ} \sum_{j=1}^{IJ} \frac{d(i)d(j)}{(c_L(i) + \mathbf{s}\cdot\mathbf{v}(i))(c_L(j) - \mathbf{s}\cdot\mathbf{v}(j))}
\end{aligned}$$

which can be expanded as follow,

$$\begin{aligned}
&\sum_{i=1}^{IJ} \sum_{j \neq i}^{IJ} \frac{d(i)d(j)c_L(j)}{c_L(i)(c_L^2(j) - (\mathbf{s}\cdot\mathbf{v}(j))^2)} + \sum_{i=1}^{IJ} \frac{d^2(i)}{c_L^2(i) - (\mathbf{s}\cdot\mathbf{v}(i))^2} = \\
&\sum_{i=1}^{IJ} \sum_{j \neq i}^{IJ} \frac{d(i)d(j)}{(c_L(i) + \mathbf{s}\cdot\mathbf{v}(i))(c_L(j) - \mathbf{s}\cdot\mathbf{v}(j))} + \sum_{i=1}^{IJ} \frac{d^2(i)}{(c_L^2(i) - (\mathbf{s}\cdot\mathbf{v}(i))^2)}
\end{aligned}$$

Therefore for (A.16) to be true we need,

$$\frac{c_L(j)}{c_L(i)(c_L^2(j) - (\mathbf{s}\cdot\mathbf{v}(j))^2)} = \frac{1}{(c_L(i) + \mathbf{s}\cdot\mathbf{v}(i))(c_L(j) - \mathbf{s}\cdot\mathbf{v}(j))} \quad , \forall i \neq j \in \{1, \dots, IJ\}$$

the right side of the above equation can be written as,

$$\begin{aligned}
\frac{1}{(c_L(i) + \mathbf{s}\cdot\mathbf{v}(i))(c_L(j) - \mathbf{s}\cdot\mathbf{v}(j))} &= \frac{(c_L(j) + \mathbf{s}\cdot\mathbf{v}(j))}{(c_L(i) + \mathbf{s}\cdot\mathbf{v}(i))(c_L^2(j) - (\mathbf{s}\cdot\mathbf{v}(j))^2)} \\
&= \frac{c_L(j)(1 + \frac{\mathbf{s}\cdot\mathbf{v}(j)}{c_L(j)})}{c_L(i)(1 + \frac{\mathbf{s}\cdot\mathbf{v}(i)}{c_L(i)})(c_L^2(j) - (\mathbf{s}\cdot\mathbf{v}(j))^2)}
\end{aligned}$$

and therefore (A.16) is valid if and only if,

$$\frac{c_L(j)}{c_L(i)(c_L^2(j) - (\mathbf{s}\cdot\mathbf{v}(j))^2)} = \frac{c_L(j)(1 + \frac{\mathbf{s}\cdot\mathbf{v}(j)}{c_L(j)})}{c_L(i)(1 + \frac{\mathbf{s}\cdot\mathbf{v}(i)}{c_L(i)})(c_L^2(j) - (\mathbf{s}\cdot\mathbf{v}(j))^2)} \quad , \forall i \neq j \in \{1, \dots, IJ\}$$

which is only valid when  $\mathbf{s}\cdot\mathbf{v}(i) \ll c_L(i), \forall i \in \{1, \dots, IJ\}$ . Note that this assumption is valid for most applications, therefore we have shown that the first claim of SIRT about the temperature-based TOA is valid.

## A.2.2 Wind-Based TOA

In this subsection we are going to evaluate (A.15). Using (A.13), (A.15) can be written as,

$$\frac{2\tau_1\tau_2}{\tau_2 - \tau_1} = \sum_{i=1}^{IJ} \frac{d(i)}{\mathbf{s}\cdot\mathbf{v}(i)}. \quad (\text{A.18})$$

Using equations (A.6) and (A.7), we expand the left hand of the equation (A.18) as follow,

$$\begin{aligned} \frac{2\tau_1\tau_2}{\tau_2 - \tau_1} &= \frac{2 \sum_{i=1}^{IJ} \frac{d(i)}{c_L(i)+\mathbf{s}\cdot\mathbf{v}(i)} \sum_{j=1}^{IJ} \frac{d(j)}{c_L(j)-\mathbf{s}\cdot\mathbf{v}(j)}}{\sum_{j=1}^{IJ} \frac{d(j)}{c_L(j)-\mathbf{s}\cdot\mathbf{v}(j)} - \sum_{i=1}^{IJ} \frac{d(i)}{c_L(i)+\mathbf{s}\cdot\mathbf{v}(i)}}} \\ &= \frac{\sum_{i=1}^{IJ} \sum_{j=1}^{IJ} \frac{d(i)d(j)}{(c_L(i)+\mathbf{s}\cdot\mathbf{v}(i))(c_L(j)-\mathbf{s}\cdot\mathbf{v}(j))}}{\sum_{j=1}^{IJ} \frac{d(j)(\mathbf{s}\cdot\mathbf{v}(j))}{c_L^2(j)-(\mathbf{s}\cdot\mathbf{v}(j))^2}} \end{aligned}$$

therefore we can rewrite equation (A.16) as

$$\begin{aligned} \sum_{i=1}^{IJ} \frac{d(i)}{\mathbf{s}\cdot\mathbf{v}(i)} &= \frac{\sum_{i=1}^{IJ} \sum_{j=1}^{IJ} \frac{d(i)d(j)}{(c_L(i)+\mathbf{s}\cdot\mathbf{v}(i))(c_L(j)-\mathbf{s}\cdot\mathbf{v}(j))}}{\sum_{j=1}^{IJ} \frac{d(j)(\mathbf{s}\cdot\mathbf{v}(j))}{c_L^2(j)-(\mathbf{s}\cdot\mathbf{v}(j))^2}} \\ \Rightarrow \sum_{i=1}^{IJ} \sum_{j=1}^{IJ} \frac{d(i)d(j)(\mathbf{s}\cdot\mathbf{v}(j))}{(\mathbf{s}\cdot\mathbf{v}(i))(c_L^2(j)-(\mathbf{s}\cdot\mathbf{v}(j))^2)} &= \sum_{i=1}^{IJ} \sum_{j=1}^{IJ} \frac{d(i)d(j)}{(c_L(i)+\mathbf{s}\cdot\mathbf{v}(i))(c_L(j)-\mathbf{s}\cdot\mathbf{v}(j))} \end{aligned}$$

which can be expanded as follow,

$$\begin{aligned} \sum_{i=1}^{IJ} \sum_{j \neq i}^{IJ} \frac{d(i)d(j)(\mathbf{s}\cdot\mathbf{v}(j))}{(\mathbf{s}\cdot\mathbf{v}(i))(c_L^2(j)-(\mathbf{s}\cdot\mathbf{v}(j))^2)} + \sum_{i=1}^{IJ} \frac{d^2(i)}{c_L^2(i)-(\mathbf{s}\cdot\mathbf{v}(i))^2} &= \\ \sum_{i=1}^{IJ} \sum_{j \neq i}^{IJ} \frac{d(i)d(j)}{(c_L(i)+\mathbf{s}\cdot\mathbf{v}(i))(c_L(j)-\mathbf{s}\cdot\mathbf{v}(j))} + \sum_{i=1}^{IJ} \frac{d^2(i)}{(c_L^2(i)-(\mathbf{s}\cdot\mathbf{v}(i))^2)} \end{aligned}$$

Therefore for (A.18) to be true we need,

$$\frac{\mathbf{s}\cdot\mathbf{v}(j)}{(\mathbf{s}\cdot\mathbf{v}(i))(c_L^2(j)-(\mathbf{s}\cdot\mathbf{v}(j))^2)} = \frac{1}{(c_L(i)+\mathbf{s}\cdot\mathbf{v}(i))(c_L(j)-\mathbf{s}\cdot\mathbf{v}(j))}, \forall i \neq j \in \{1, \dots, IJ\}$$

the right side of the above equation can be written as,

$$\begin{aligned} \frac{1}{(c_L(i)+\mathbf{s}\cdot\mathbf{v}(i))(c_L(j)-\mathbf{s}\cdot\mathbf{v}(j))} &= \frac{(c_L(j)+\mathbf{s}\cdot\mathbf{v}(j))}{(c_L(i)+\mathbf{s}\cdot\mathbf{v}(i))(c_L^2(j)-(\mathbf{s}\cdot\mathbf{v}(j))^2)} \\ &= \frac{(\mathbf{s}\cdot\mathbf{v}(j))(1+\frac{c_L(j)}{\mathbf{s}\cdot\mathbf{v}(j)})}{(\mathbf{s}\cdot\mathbf{v}(i))(1+\frac{c_L(i)}{\mathbf{s}\cdot\mathbf{v}(i)})(c_L^2(j)-(\mathbf{s}\cdot\mathbf{v}(j))^2)} \end{aligned}$$

and therefore (A.18) is valid if and only if,

$$\frac{\mathbf{s} \cdot \mathbf{v}(j)}{(\mathbf{s} \cdot \mathbf{v}(i))(c_L^2(j) - (\mathbf{s} \cdot \mathbf{v}(j))^2)} = \frac{(\mathbf{s} \cdot \mathbf{v}(j))(1 + \frac{c_L(j)}{\mathbf{s} \cdot \mathbf{v}(j)})}{(\mathbf{s} \cdot \mathbf{v}(i))(1 + \frac{c_L(i)}{\mathbf{s} \cdot \mathbf{v}(i)})(c_L^2(j) - (\mathbf{s} \cdot \mathbf{v}(j))^2)}, \forall i \neq j \in \{1, \dots, IJ\}$$

which is only valid when  $\frac{c_L(i)}{\mathbf{s} \cdot \mathbf{v}(i)} \approx \frac{c_L(j)}{\mathbf{s} \cdot \mathbf{v}(j)}, \forall j \neq i \in \{1, \dots, IJ\}$ . Note that this assumption could be true for special cases, however it is not valid in general, i.e. when  $\mathbf{s} \cdot \mathbf{v}$  is fluctuating near zero or when the wind is erratic in the investigation area.

### A.3 Simulation and Results

In order to show the discrepancy of the SIRT method in calculating the wind velocity-based TOA, a synthetic data set was generated based on the layout of the STINHO-2 experiment, shown in Figure A.2. The synthetic fields are generated for 500 snapshots with spatial and temporal resolution of 1m and 12sec, respectively. The TOAs,  $\tau_{n,1}$  and  $\tau_{n,2}$  for  $n = 1, \dots, 28$ , are then generated for the paths between reciprocal sensors  $R1, \dots, R8$ .

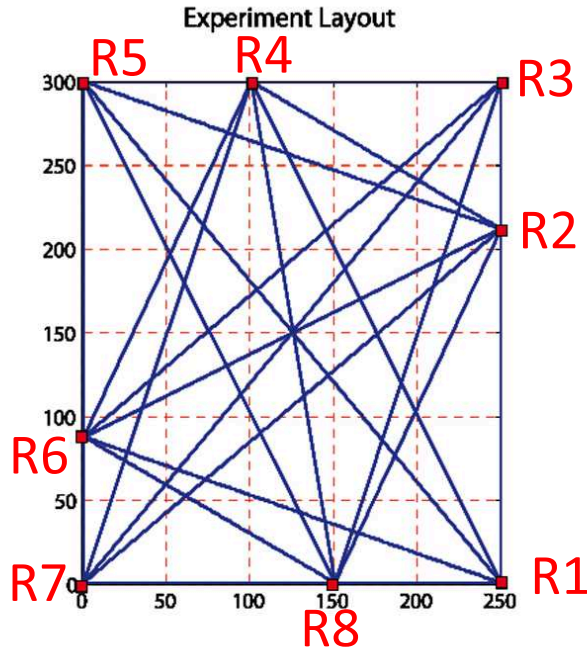


**Figure A.2:** Layout of the STINHO-2 experiment with reciprocal sensors

A  $5 \times 6$  grid is laid on the synthetic fields forming cells of the size  $50m \times 50m$ . The actual temperature-based and wind velocity-based TOAs are then calculated from (A.14) and (A.15), respectively. Finally, the estimated temperature-based and wind velocity-based TOAs are calculated from (A.12) and (A.13), using  $\tau_{n,1}$  and  $\tau_{n,2}$  for  $n = 1, \dots, 28$ .

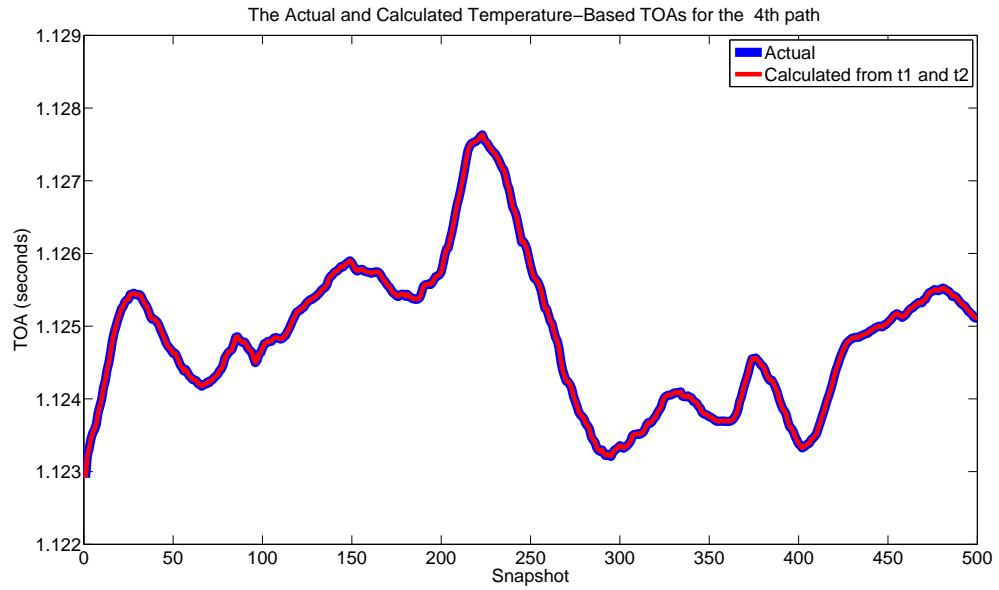
Figure A.3 shows the actual and estimated temperature-based TOA for the sample path number four (R1-R5), and the estimation error for this path over all snapshots. Note that the mean Laplace sound speed in this case was around  $340 \frac{m}{sec}$  while the mean wind velocity amplitude was around  $0.8 \frac{m}{sec}$ , therefore the condition  $\mathbf{s} \cdot \mathbf{v}(i) \ll c_L(i), \forall i \in \{1, \dots, IJ\}$  holds and (A.16) is valid, as it can be seen in Figure A.3.

To investigate SIRT's second claim (A.18), the actual and estimated wind velocity-based TOAs were calculated from (A.15) and (A.13), respectively. Figures A.4 and A.5 show the actual and estimated wind velocity-based TOAs for paths number 4 and 12. It can be seen that when  $\mathbf{s}_n \cdot \mathbf{v}$  is fluctuating near zero (the wind becomes semi-perpendicular to the path), the condition  $\frac{c_L(i)}{\mathbf{s} \cdot \mathbf{v}(i)} \approx \frac{c_L(j)}{\mathbf{s} \cdot \mathbf{v}(j)}$  does not hold and the wind velocity-based TOAs estimation errors increase drastically. These results confirm our findings in the previous section.

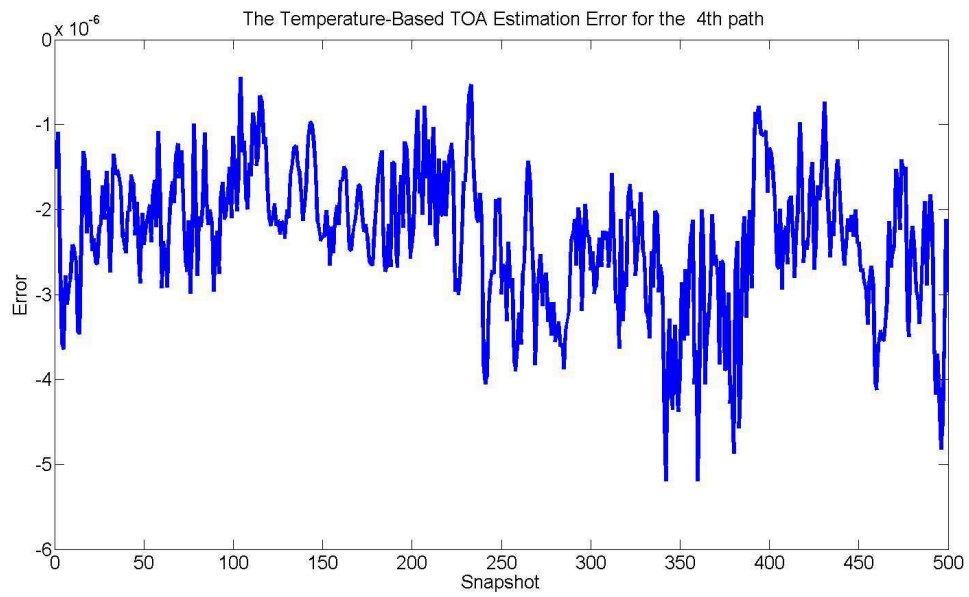
The huge discrepancy between the actual and estimated wind velocity-based TOA for some paths, will lead to inaccurate and in some cases irrelevant wind velocity reconstruction.

## A.4 Conclusion

The SIRT-based acoustic tomography formulation was studied closely and some discrepancies were shown in the wind velocity-based TOA estimation, which can cause noticeable inaccuracies in wind velocity reconstruction. We believe that this issue should be addressed and studied in detail.



(a)



(b)

**Figure A.3:** (a) Actual and estimated temperature-based TOA for the path number 4 (b) The temperature-based TOA estimation error

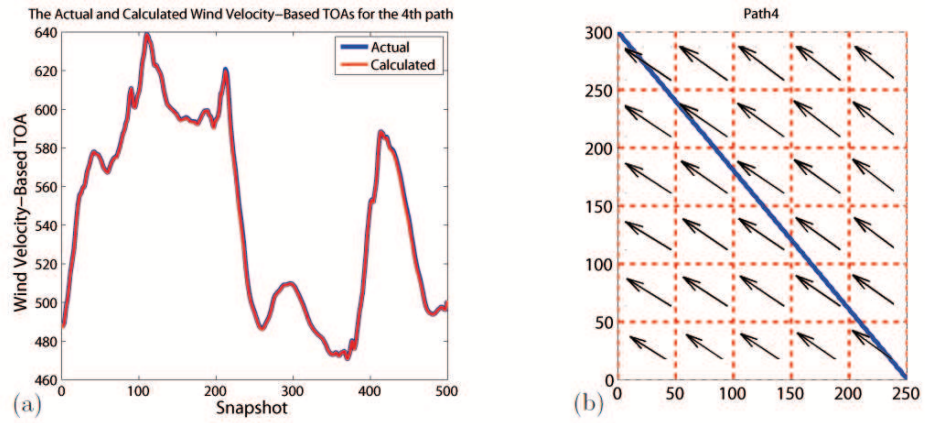


**Figure A.4:** (a) The actual and estimated wind velocity-based TOA for the 4'th path over all snapshots (b) the layout of the field and the 4'th path, with the mean wind velocity over all snapshots

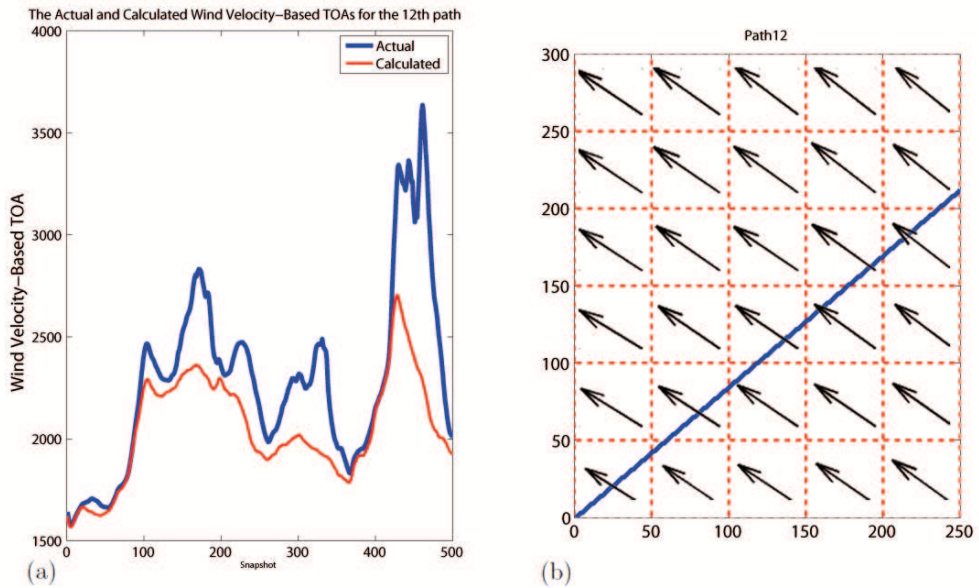


**Figure A.5:** (a) The actual and estimated wind velocity-based TOA for the 12'th path over all snapshots (b) the layout of the field and the 12'th path, with the mean wind velocity over all snapshots